



Cadmium zinc telluride and its use as a nuclear radiation detector material

T.E. Schlesinger^{a,*}, J.E. Toney^b, H. Yoon^c, E.Y. Lee^d, B.A. Brunett^d, L. Franks^d, R.B. James^d

^aDepartment of Electrical and Computer Engineering, Carnegie Mellon University, Pittsburgh, PA 15213, USA

^bSpire Corporation, Bedford, MA, USA

^cSpectrolab, Inc., Sylmar, CA, USA

^dSandia National Laboratories, Livermore, CA, USA

Accepted 18 December 2000

Abstract

We present a comprehensive review of the material properties of cadmium zinc telluride (CZT, $\text{Cd}_{1-x}\text{Zn}_x\text{Te}$) with zinc content $x = 0.1\text{--}0.2$. Particular emphasis is placed on those aspects of this material related to room temperature nuclear detectors. A review of the structural properties, charge transport, and contacting issues and how these are related to detector and spectrometer performance is presented. A comprehensive literature survey and bibliography are also included. © 2001 Elsevier Science B.V. All rights reserved.

Keywords: Cadmium zinc telluride; Nuclear detector; Spectroscopy

1. Fundamental material properties

1.1. Introduction

The ability to detect and perform energy-dispersive spectroscopy of high energy radiation such as X-rays, gamma-rays, and other uncharged and charged particles has improved dramatically in recent years. This is of great importance in a wide range of applications including medical imaging, industrial process monitoring, national security and treaty verification, environmental safety and remediation, and basic science. Central to the movement of this technology out of the laboratory and into commercial systems has been the remarkable progress in the technology associated with devices and systems operating at room temperature. With the elimination of cryogenic cooling it is possible to manufacture low-power systems that are far more compact and that can operate in the field or for long periods of time in an unattended mode.

This review discusses the material properties of cadmium zinc telluride ($\text{Cd}_{1-x}\text{Zn}_x\text{Te}$ or CZT) with Zn concentrations in the range $x = 0.1\text{--}0.2$. CZT in this composition range is used for the fabrication of radiation detectors deployed in these systems. In what follows we first introduce the reasons that this material is well suited for this application as well as providing a short overview of the key steps involved in the fabrication of the devices. This will serve to motivate the reasons we focus on particular material properties and device fabrication issues associated with CZT.

* Corresponding author. Tel.: +1-412-2688728; fax: +1-412-2682860.

In this review we have attempted to present a balanced overview of what is the result of a great deal of effort by many researchers around the world who have contributed to the development of CZT as a nuclear radiation detector material. Invariably when writing such a review one cannot ensure that all those who have contributed to the field are properly referenced and that all results deserving discussion are included in the article. In addition it is often the case that authors of such a review may tend to emphasize their own work as this is closest at hand and, of course, what they are ultimately most familiar with. To the extent that we are guilty of both of these errors we apologize in advance both to the reader and to the workers whose efforts may not have received the proper emphasis within the article. Nonetheless, we hope that this review and bibliography will serve as a useful summary of the work that has helped to advance the understanding of this material and move forward the technology of room temperature radiation detectors.

1.2. Interaction of radiation with semiconductors

Electromagnetic radiation such as X-rays and gamma-rays can interact with a solid-state detector via four mechanisms [1]. These are elastic scattering, photoelectric absorption, Compton scattering, and pair production. It is photoelectric absorption which, in most cases, is the ideal process for detector operation. In this process all the energy of an incident photon is absorbed by one of the orbital electrons of the atoms of the detector material. This photoelectron will then lose the kinetic energy it has acquired via Coloumb interactions with the semiconductor lattice creating many electron–hole pairs. Detection of these charges as a current pulse via an external circuit allows the creation of a histogram of pulse heights, the pulse height spectrum, with the peak due to this interaction called the photopeak.

Independent of which semiconductor material is employed, certain material properties are required for the realization of high performance spectrometers that provide both good spectral resolution and high counting efficiency. While some requirements are the same as would be required for any semiconductor device technology, others are particular for this application. Some of the key properties are as follows:

1. High atomic number (Z) for efficient radiation–atomic interactions. The cross-section for photoelectric absorption in a material of atomic number Z varies as Z^n , where $4 < n < 5$.
2. Large enough bandgap for high resistivity and low leakage current. Low leakage currents when an electric field is applied during operation are critical for low noise operation. The high resistivity necessary ($>10^9 \Omega \text{ cm}$) is achieved by using larger bandgap materials with low intrinsic carrier concentrations and by controlling the extrinsic and intrinsic defects to pin the Fermi-level near midgap.
3. Small enough bandgap so that the electron–hole ionization energy is small ($<5 \text{ eV}$). While there is no absolute minimum bandgap energy for radiation detection, values above about 1.5 eV are normally needed to control thermally generated current and resultant losses in energy resolution due to noise. This ensures that the number of electron–hole pairs created is reasonably large and the statistical variation in the number of electron–hole pairs created is small. This results in higher signal to noise ratio.
4. High intrinsic $\mu\tau$ product. The carrier drift length is given by $\mu\tau E$ [2], where μ is the carrier mobility, τ the carrier lifetime, and E the applied electric field. Charge collection is determined by what fraction of the detector thickness photogenerated electrons and holes traverse during the time charge is collected. In the ideal case the carrier drift length would be far greater than the detector thickness to ensure complete charge collection. While this may be the case for electrons

in some materials, it is typically not the case for holes. Thus, these devices often suffer from incomplete hole collection, which results in less than full charge collection and a reduced current pulse. This in turn broadens the photopeak in the pulse height spectrum to the low energy side and thereby decreases the resolution of the spectrometer.

5. High-purity, homogeneous, defect-free materials with acceptable cross-sectional areas and thickness. For high-sensitivity and efficiency, large detector volumes are required to ensure that as many incident photons as possible have the opportunity to interact in the detector volume. Related to this is the requirement that the detector material be of high density, although this is essentially guaranteed simply by virtue of the fact that a solid material is employed for the detector material in contrast to gas detectors. The requirement of homogeneity and low defect density is to ensure good charge transport properties, low leakage currents, and no conductive short circuits between the detector contacts. In most cases, single-crystal volumes are required to reduce the deleterious effects of grain boundaries and other extended defects.
6. Electrodes that produce no defects, impurities or barriers to the charge collection process and which can be used effectively to apply a uniform electric field across the device. Related to this is the requirement to be free of polarization effects in the detector. These are any processes (e.g. space-charge buildup within the device) that over time change the magnitude or uniformity of the electric field within the device and thus produce temporal changes in the detector operation.
7. Surfaces with sufficiently high electrical resistivity that noise due to surface conduction is low. The surfaces should be stable over time to prevent increases in the surface leakage currents over the lifetime of the detector. It is also important that the electric field lines within the detector do not terminate at its non-contacted surfaces to prevent problems of incomplete charge collection and buildup of surface charges.

In considering all the requirements listed above, certain materials appear to be especially well suited for this application. In particular cadmium zinc telluride ($\text{Cd}_{1-x}\text{Zn}_x\text{Te}$ or CZT) has come to the forefront among a number of materials for this application and in recent years (CZT) X-ray and gamma-ray spectrometers have been developed to the point that they now can reliably produce high resolution spectra over a wide energy range [3]. This performance has been achieved through both improved material properties [4] and through the development of a number of device geometries which take best advantage of the material properties.

1.3. Detector fabrication

The fabrication of semiconductor nuclear detectors involves a number of critical steps. These will typically include growth of high resistivity material, slicing and polishing of the device volume, the application of metal contacts (including photolithographic processes), surface passivation to limit surface leakage currents, and finally packaging (including bonding to the external circuitry).

While most CZT used for X-ray and gamma-ray detectors is grown by the high pressure Bridgman method, there have also been reports of detectors fabricated from material grown by modified conventional Bridgman and vapor phase transport techniques [5–8]. The primary goal on which every growth technique is focused is the production of defect-free, high-resistivity material, in sufficient quantities to ensure high yield and low cost. These growth methods are discussed in detail in sections of this review. We also describe the primary structural defects that are often observed in CZT and how these may affect detector performance.

Material resistivity is typically controlled by intrinsic and extrinsic dopants which pin the Fermi-level near midgap. A complete description of the defect states, the balance between them, and

how they determine the resistivity of CZT have not yet been fully achieved. Nonetheless, in this review we present a discussion of the current understanding of the dominant defects in CZT, including those that may be detrimental to achieving high resistivity material.

Room temperature semiconductor nuclear detectors generally employ one of a small number of device configurations. Particular geometries which have proven to be of particular importance include electrode configurations that function as electron-only devices [9–13], devices that exploit what has become known as the “small pixel effect” [14], and devices in which the size of the collecting electrode is adjusted for optimal performance for a particular $\mu\tau$ (mobility-lifetime) product [15]. Some generic device configurations are shown schematically in Fig. 1. Pictured in this figure are (a) a simple planar device, (b) a co-planar grid, and (c) a pixellated array. Each of these may be used for applications where particular performance parameters are to be optimized. For example, simple planar detectors or co-planar grids are generally employed for large volume single element detectors. The former is simpler to implement in terms of the associated electronics but the latter operating as an “electron-only” devices provide higher spectral resolution, particularly for higher energy gamma rays (i.e. >200 keV). Pixellated detectors are employed in imaging systems, where position information is contained in the signals from individual pixels. In each case lithographic techniques are employed to define the geometry of the metal electrodes, which are applied to the surface of the semiconductor material. The choice of metal and the control of the deposition method (whether sputtering, evaporation, or electroless deposition) can affect the quality

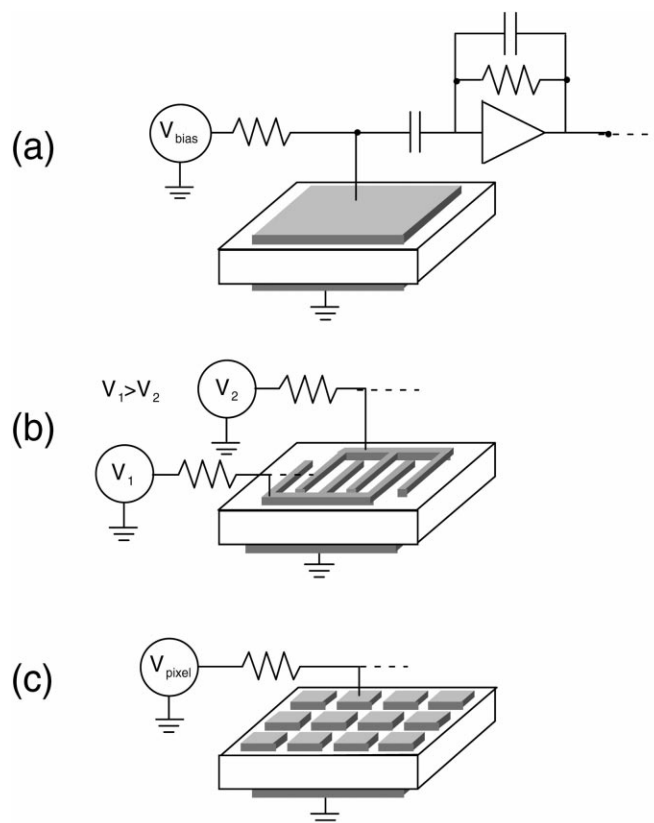


Fig. 1. Schematic diagram of three basic nuclear detector geometries: (a) single element planar detector; (b) co-planar grid detector; (c) pixellated detector for imaging applications.

of the device which is fabricated. However, as will be discussed in this review, finding the correct conditions for each metal or deposition technique is more critical than the particular deposition method employed.

Under operating conditions, a high voltage (on the order of 1000 V/cm) is typically applied across the device, and incident high energy photons interact in the volume of the detector. The charges created by the interaction of the high energy photon and the detector material drift across the detector volume inducing a current in the external circuit. This current is typically integrated by an external circuit with the total charge collected in this manner being proportional to the energy of the incident photon. By creating a histogram of the pulse heights detected in this manner, a pulse height spectrum is created with the peaks in the spectrum corresponding to the energies of the incident photons. As mentioned above the device geometries and pulse processing methods employed can have a major effect on device performance. Indeed, material that will not produce acceptable spectra in one configuration or with one particular set of electronics may work very well in another configuration or in conjunction with more sophisticated electronics. Nonetheless a discussion of these aspects of this technology is beyond the scope of this review as we will focus on the materials properties of the CZT and those of the metal/CZT junctions.

1.4. Crystal structure

CdTe and ZnTe have the cubic zinc sulfide, or zincblende, structure [16]. This structure is sometimes described as a pair of interpenetrating face centered cubic (fcc) sub-lattices, offset from each other by one-quarter of a unit cell body diagonal, with the Cd or Zn nuclei occupying one sub-lattice and the Te nuclei the other. Mathematically, this structure is most conveniently described as a fcc Bravais lattice with a two-point basis. The basis can be taken as

$$\sigma_1 = (0, 0, 0) \quad (1)$$

$$\sigma_2 = \left(\frac{1}{4}a, \frac{1}{4}a, \frac{1}{4}a\right) \quad (2)$$

where x , y , and z are the orthogonal unit vectors. The X-ray scattering amplitude for this lattice and basis is proportional to the geometrical structure factor, given by

$$S(\mathbf{q}) = \sum_{i=1}^2 f_i e^{i(\sigma_i \cdot \mathbf{q})} \quad (3)$$

where \mathbf{q} is the scattering vector (difference between incident and scattered wave vectors), and f_1 and f_2 are the atomic form factors for Cd (or Zn) and Te, respectively. At a Bragg peak \mathbf{q} is equal to some reciprocal lattice vector, \mathbf{K} , so that the structure factor is

$$S(\mathbf{K}) = f_1 + f_2 e^{i(\sigma_2 \cdot \mathbf{K})} \quad (4)$$

If f_1 and f_2 were equal, as in the diamond structure possessed by Si and Ge, it would be possible for $S(\mathbf{K})$ to be zero for certain values of \mathbf{K} , leading to “forbidden” reflections, that is, diffraction peaks which the underlying Bravais lattice (fcc) possesses but which the lattice with basis does not. But since for the zincblende structure the two form factors are different, the structure factor introduced by the basis is never zero, and the crystal has the same set of diffraction peaks as fcc, although the relative amplitudes are different.

The alloy $\text{Cd}_{1-x}\text{Zn}_x\text{Te}$ can ideally be regarded as a CdTe crystal with Zn atoms randomly substituted for a fraction x of the Cd atoms. No strong evidence for phase separation in high pressure Bridgman materials has been presented, although micron-scale compositional variations have been observed [17]. The difference in the lattice constants of CdTe and ZnTe implies that this substitution is accompanied by some change in the average unit cell dimension. It is usually assumed that the resulting lattice constant is a linear interpolation between the two constituents, but EXAFS measurements have shown a bimodal distribution of bond lengths, suggesting distortion of the Te sub-lattice [18], so that the linear interpolation is true only in an approximate sense.

Within the limits of the linear approximation, known as Vegard's law, there is a simple relationship between the lattice constant and the alloy composition:

$$a(x) = a_1(1 - x) + a_2x \quad (5)$$

where a_1 and a_2 are the lattice constants of CdTe and ZnTe, respectively. The average lattice constant can be determined by simple X-ray diffraction using Bragg's law:

$$n\lambda = 2d \sin(\theta) \quad (6)$$

where λ is the wavelength of the incident radiation, d the distance between crystal planes, θ is the angle of incidence, and n is any positive integer. The distance d depends on the orientation of the crystal, but is directly proportional to the lattice constant, a . The alloy composition can thus be determined from the position of the diffraction peak.

Fig. 2 shows a powder X-ray diffraction curve for $\text{Cd}_{1-x}\text{Zn}_x\text{Te}$ with $x \approx 0.1$. The zinc fraction of the sample can be estimated from the position of the (2 2 0) peak using Eq. (6). For this set of planes,

$$d = \frac{1}{2} \sqrt{2}a \quad (7)$$

and for this peak $n = 2$, Eq. (6) gives

$$a = \frac{\sqrt{2}\lambda}{\sin(\theta)} \quad (8)$$

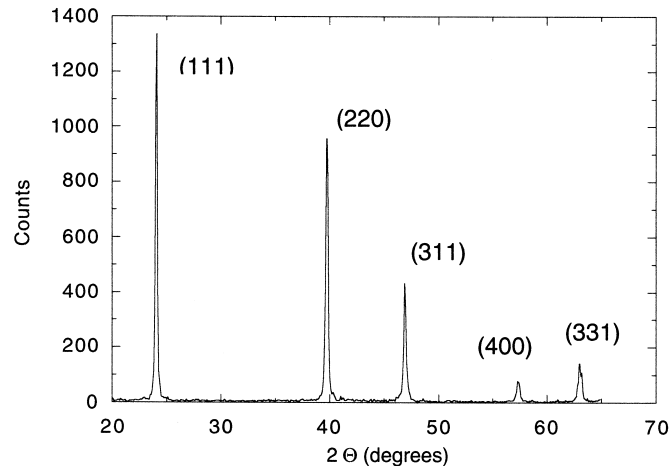


Fig. 2. Powder X-ray diffraction curve for $\text{Cd}_{1-x}\text{Zn}_x\text{Te}$ with $x \sim 0.1$ [193].

Using the peak position of $2\theta = 39.9^\circ$ gives $x = 0.16$, which is a reasonable approximation. A more accurate determination of the lattice constant can be achieved by high resolution triple axis X-ray diffraction but the use of this technique requires oriented single crystals to obtain sufficient signal and to determine the separate effects of strain and mosaicity [19]. Triple axis XRD will be discussed in more detail later in this review.

1.5. Lattice dynamics structure

Zincblende crystals, having a two-atom basis, exhibit three acoustic and three optical vibrational modes — two transverse and one longitudinal in each case, although the two transverse modes are degenerate in the high-symmetry directions [20]. Dispersion relations for CdTe and ZnTe have been calculated [21] using the 11-parameter rigid ion model of [22] and measured by inelastic neutron scattering [23,24]. The calculated and measured dispersion curves for CdTe are shown in Fig. 3.

The vibrational modes of $\text{Cd}_{1-x}\text{Zn}_x\text{Te}$, as observed by infrared absorption or Raman scattering measurements, are not a simple interpolation between those of its constituents. Rather than a single TO and a single LO mode, two of each type of mode are observed, one being termed “CdTe-like” and the other, “ZnTe-like.” This behavior is typical for ternary semiconductor compounds, but $\text{Cd}_{1-x}\text{Zn}_x\text{Te}$ has the unique property that the frequencies of both TO modes increase with x [25]. In all similar alloys one TO frequency increases while the other decreases with x .

1.6. Band structure

CdTe and ZnTe are direct-bandgap semiconductors with bandgaps at room temperature of approximately 1.5 and 2.2 eV, respectively [26]. The direct bandgap makes these compounds attractive for optical devices and is also helpful for optical characterization techniques such as photoluminescence. The band structure of CdTe, based on pseudopotential calculations [27] is shown in Fig. 4; the band structure of ZnTe is qualitatively similar. There are four valence bands to accommodate the eight valence electrons per primitive cell. The degeneracy of the heavy-hole and

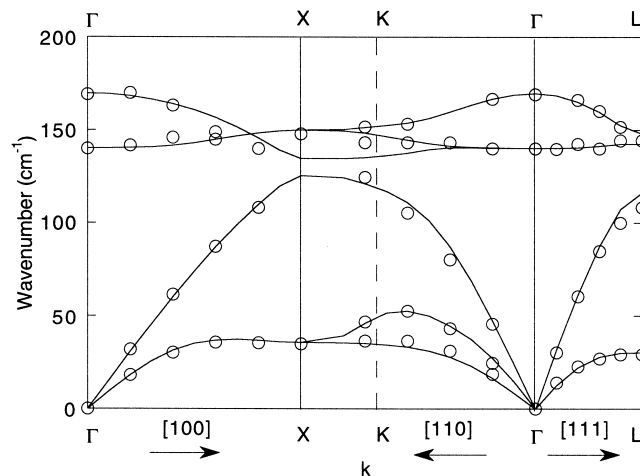


Fig. 3. Phonon dispersion curves for CdTe calculated by the 11-parameter rigid-ion model (lines) and measured by inelastic neutron diffraction (circles). Calculation after Plumelle and Vandevyver [21], data from Rowe et al. [23].

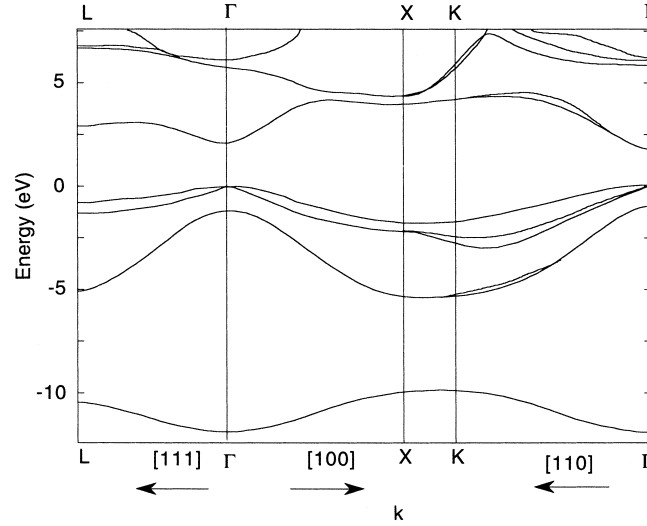


Fig. 4. Band structure of CdTe calculated by the pseudopotential method [27].

light-hole bands, and the degeneracy at $\mathbf{k} = 0$ of the split-off band with the heavy- and light-hole bands, is removed by spin-orbit interaction [28]. The constant energy surface is spherical, which means that the effective masses are given simply by the reciprocal of the curvature of the energy band in \mathbf{k} -space at $\mathbf{k} = 0$:

$$\frac{1}{m^*} = \frac{(2\pi)^2}{h^2} \frac{\partial^2 E}{\partial k^2} \quad (9)$$

Both CdTe and ZnTe have relatively low effective masses for electrons (approximately $0.11m_0$ and $0.15m_0$, respectively) [26], giving them reasonably good transport properties. For holes one must remember that there are different effective masses for the separate valence bands, and how they are to be combined to determine an “average” effective mass depends on the context. One is sometimes interested in the density of states effective mass, given by (neglecting the split-off band):

$$m_{\text{dh}} = (m_{\text{hh}}^{3/2} + m_{\text{lh}}^{3/2})^{2/3} \quad (10)$$

where m_{hh} and m_{lh} are the heavy and light-hole band effective masses, respectively [29]. Sometimes in the conductivity effective mass, one uses the equation

$$m_{\text{ch}} = \frac{m_{\text{dh}}^{3/2}}{m_{\text{hh}}^{1/2} + m_{\text{lh}}^{1/2}} \quad (11)$$

to describe the effective hole mass. Kanzer [30] gives the effective hole masses (in units of m_0) as

$$\text{CdTe : } m_{\text{hh}} = 0.70, m_{\text{lh}} = 0.103, \quad \text{ZnTe : } m_{\text{hh}} = 0.63, m_{\text{lh}} = 0.154 \quad (12)$$

We thus have

$$\text{CdTe : } m_{\text{dh}} = 0.73, m_{\text{ch}} = 0.53, \quad \text{ZnTe : } m_{\text{dh}} = 0.68, m_{\text{ch}} = 0.47 \quad (13)$$

The question of the band structure of $\text{Cd}_{1-x}\text{Zn}_x\text{Te}$, or any ternary semiconductor, is a fairly difficult one, because the entire band theory of solids is based on the assumption of periodicity, which does not exist in an alloy because of local composition fluctuations. A starting point for calculations is the virtual crystal approximation [31], which is the assumption that the crystal potential (for example, the matrix elements in the tight-binding approximation) is a linear interpolation between those of the two constituents. This approach generally does not give the correct dependence of the bandgap on composition. Singh [31] points out that for direct-bandgap semiconductors in the tight-binding approximation, the band edges are linear sums of the matrix elements, which implies that the bandgap should vary linearly with x . In practice, the measured dependence of the bandgap as a function of composition ($E_g(x)$) is always found to have some curvature, which can usually be fit well to a quadratic. The coefficient of the quadratic term is called the bowing parameter, and is attributed to short-range disorder [32]. Shim et al. [33] have generalized the tight-binding approach to include disorder and relaxation effects and have obtained reasonable results for the composition dependence of the direct bandgap and direct–indirect transition in several III–V alloys, lending support to the idea that the bowing stems from local disorder. The value of the bowing parameter for $\text{Cd}_{1-x}\text{Zn}_x\text{Te}$ is discussed in a subsequent section.

2. Growth

2.1. Phase diagrams

A phase diagram for the CdTe – ZnTe pseudobinary, of fundamental importance in the development of growth strategies, is shown in Fig. 5 [34]. This temperature–composition diagram is characterized by a liquidus curve (upper) designating the composition of liquidus and a solidus curve (lower) defining solid solutions. The end-points are determined by the melting point of the two pure components. The area between the two curves defines a two-phase region. Data points (both curves) are due to Steininger et al. [35]. It is seen that CdTe and ZnTe form a solid solution throughout the entire alloy range. In addition, it is to be noted that the first solid that forms from the melt will contain more zinc than the initial averaged content of the melt.

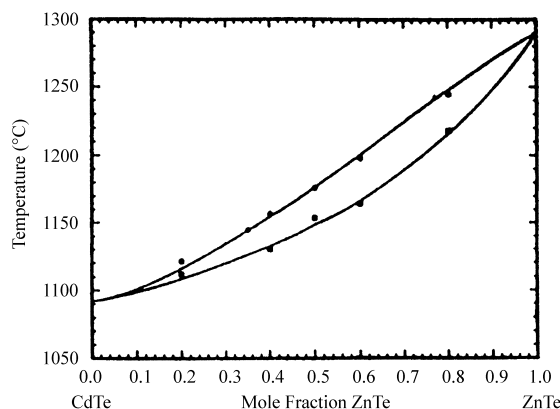


Fig. 5. Calculated liquidus and solidus lines in the CdTe – ZnTe pseudobinary. Experimental points are due to Steininger et al. [35], and Yu and Brebrick [34].

2.2. Growth methods

A number of methods have been successfully employed in the growth of $\text{Cd}_{1-x}\text{Zn}_x\text{Te}$ for substrate applications, including the traveling wave heater [36], Bridgman [37,38,252], physical vapor growth [39] and vapor phase epitaxy [260,261]. Numerous variations of each method have been reported. Interest in CZT as a substrate arises from the ability to create nearly perfect lattice-matching with such materials as HgCdTe, HgZnTe, and HgZnSeTe by adjustment of the Zn composition (x). In addition to lattice-matching, a high degree of structural perfection is necessary. For room temperature nuclear detector applications, very stringent electrical requirements must be met as well as a high degree of structural perfection. For the latter application, the method of choice of commercial suppliers is primarily the high pressure Bridgman method [4,40–42]. While less popular commercially, very good spectrographic quality material has also been produced by low-pressure variants of the basic Bridgman technique (LPB) [5–7,37,43]. In an effort to avoid deficiencies inherent in Bridgman grown materials, research continues on alternative methods such as physical vapor phase (PVT) [44–47], as well as on other melt-growth methods. Salient features of the HPB, LPB, and PVT techniques together with the material characteristics of the product materials are summarized in the following subsections.

2.2.1. Basic Bridgman method

The basic Bridgman method involves the movement of a crucible containing the melt through a furnace designed to provide a suitable temperature profile. The furnace may be either vertical or horizontal. The crucible may be transported through the heater, or the crucible stationary with a moving heater, or alternatively, both stationary and the temperature profile altered by a programmed temperature controller.

2.2.2. High pressure Bridgman

In the HPB method an over-pressure of 10–150 atm of an inert gas, typically argon, is maintained over the melt to suppress the loss of volatile components [3]. While the elevated pressure reduces the loss of these components, the losses are not eliminated. Continuous losses of cadmium, the highest vapor pressure component, causes the melt to become enriched in tellurium during growth.

A schematic diagram of a typical HPB furnace is shown in Fig. 6 [48]. The furnace is enclosed in a steel pressure vessel. We note that certain features of the furnace in Fig. 6, most notably the water jacket, are not common to all HPB furnaces. The temperature profile of the furnace is maintained by graphite ([49] or like heater elements). A multi-zone temperature profile is sometimes employed with the hot zone fixed at about 1100°C. The crucible is fitted with a cover to reduce vapor losses. Particular care must be taken in the choice of crucible material because of the potential for contamination of the melt. Quartz, for example, can be a source of significant oxygen contamination [3]. Porous graphite, which is amenable to high-temperature bakeout, is used most frequently. Carbon-coated quartz crucibles are also in common use. Travel of the crucible in this design is controlled by a mechanical actuator introduced through a high pressure feedthrough. Crucibles with inside diameters up to 10 cm holding charges up to 10 kg have been reported [42]. Growth rates vary but are typically in region of 0.1–1 mm/h.

In practice, the constituent elements undergo multiple purification and are weighed to stoichiometric proportions prior to introduction into the crucible. Before initiation of the growth cycle, the charge is heated in a programmed schedule. Following the growth phase the crystal is gradually brought to room temperature and ambient pressure. The complete growth cycle is

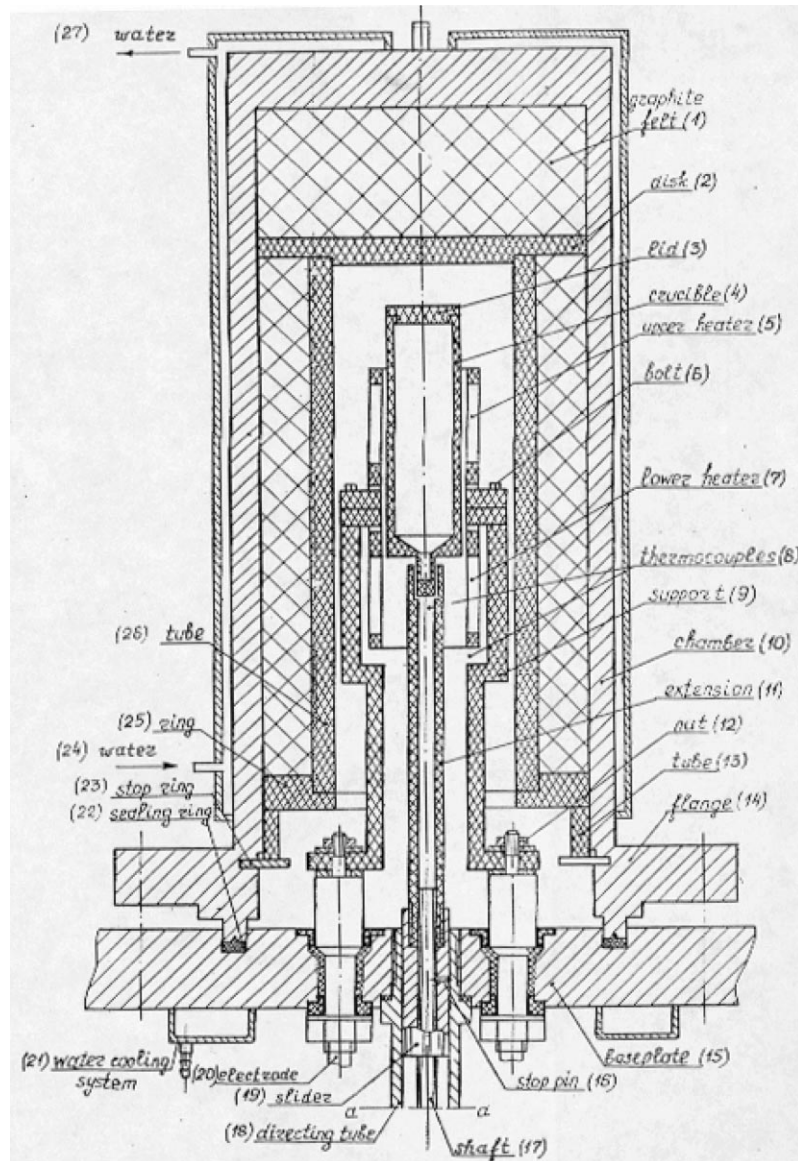


Fig. 6. Schematic diagram of high pressure Bridgman furnace used for the growth of $\text{Cd}_{1-x}\text{Zn}_x\text{Te}$ ([48], private communication).

completed in about 3–4 weeks. A typical CZT ingot grown by the HPB is shown by the top photo in Fig. 7. In the current stage of development CZT crystals typically contain macro defects such as pipes, wires, cracks, grain and twin boundaries as well as tellurium inclusions and precipitates. The latter result from retrograde solubility in the phase diagram [16,50] and are inherent in the HPB process. The spatial distribution of precipitates is normally one of three types: dispersed, cellular, or segregated along grain and twin boundaries. Those precipitates dispersed in CZT appear to have little effect on the electrical properties [51]; the same is not necessarily true for Te precipitates along grain and twin boundaries. With the relatively low bandgap (0.33 eV) of Te the electrical resistivity of the Te-rich precipitates and wires will be several orders of magnitude lower than the surrounding CZT and might account for the higher leakage found along grain boundaries. Impurities, which also have

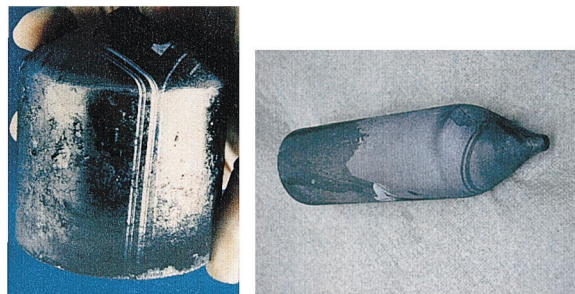


Fig. 7. Left: HPB grown $\text{Cd}_{1-x}\text{Zn}_x\text{Te}$ ingot (Doty, private communication, Sandia National Laboratories, Livermore, CA). Right: low-pressure vertical Bridgman grown $\text{Cd}_{1-x}\text{Zn}_x\text{Te}$ ingot (Li, Ynnel Tech, private communication, 2000).

an affinity for these sites, could contribute to higher leakage currents as well. An infrared transmission micrograph of Te precipitates along a grain boundary is shown in Fig. 8. Efforts to increase electrical resistivity or carrier lifetimes of HPB grown material by annealing have to date, been unsuccessful [52,53]. The net result of the various macro defects is to limit the useful portion of currently available ingots to about 25% of the total volume [51]. In addition, there are effects related to liquid–solid solubility factors (see Section 3.1), which are manifest as axial (along growth axis)

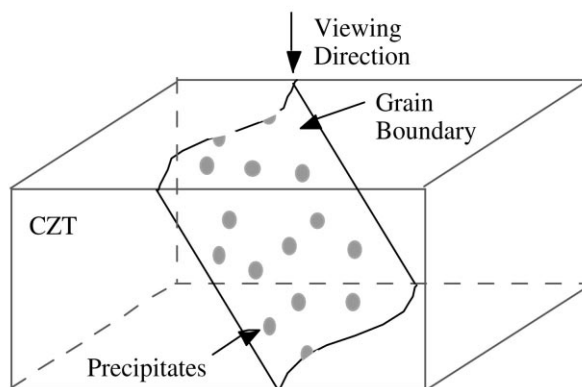
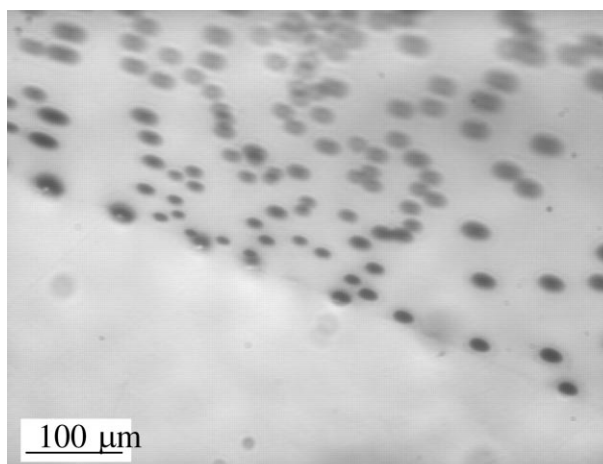


Fig. 8. Infrared transmission micrograph of CZT as seen along a grain boundary. The decoration of the grain boundary with Te precipitates is illustrated below the infrared image [50].

variations in the concentration of both impurities and the base constituents. One important issue is the decline in the zinc concentration along the growth axis of the boule due to its greater-than-unity segregation coefficient. The various crystalline flaws and non-homogeneities limit the full exploitation of the material, particularly for large ($>1\text{ cm}^3$) spectrometer-grade devices. The yield of such devices is relatively low ($<10\%$), which adversely affects cost and availability.

2.2.3. Low pressure Bridgman (LPB)

As noted previously, the Bridgman growth technique has also been successfully employed to produce spectrometer quality CZT without the use of a high gas over-pressure. As discussed below in one case a horizontal design is employed with a stationary charge and furnace, moving temperature gradient (established by an electronic controller), and an internal cadmium reservoir. In the other, a vertical configuration with a multi-zone furnace was employed.

The horizontal Bridgman technique offers potential advantages over vertical designs. These accrue from the perpendicular orientation of the gravitational field relative to the growth axis. The growth interface is not subject to the weight of the liquid, and the ingot is not confined to a fixed volume. Perhaps more importantly, the geometry is more amenable to control of the stoichiometry by having metal vapor in contact with both the liquid and solid phases. The method has been used to produce $\text{Cd}_{1-x}\text{Zn}_x\text{Te}$ with x in the region of 0.12–0.04. A typical furnace design is shown in Fig. 9. The design features a multi-zone heater, which is used to maintain a 1100°C growth zone, and an 800°C region for controlling the cadmium vapor pressure. The furnace is programmed so that a temperature gradient moves axially and the charge and furnace are stationary. A transverse gradient ($\approx 1.5^\circ\text{C}/\text{cm}$), established by modifying the insulation, is used in some cases. The charge is typically about 1–2 kg. Synthesis and growth are performed in the same ampoule to minimize contamination, although the basic method is self purifying and not highly sensitive to the purity level of the starting

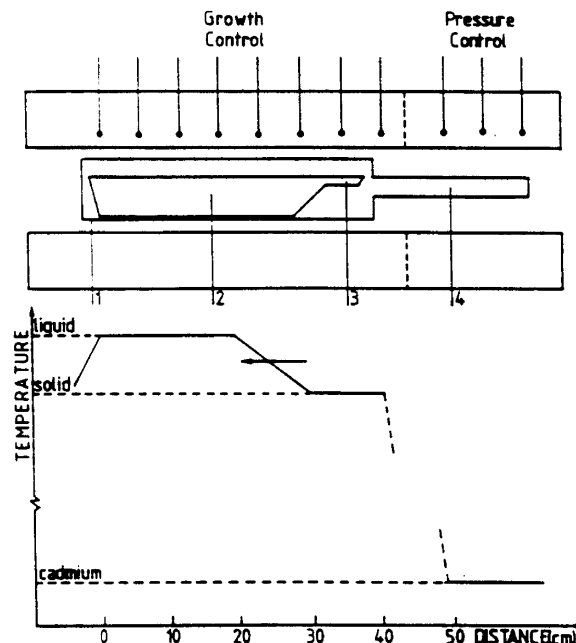


Fig. 9. Multi-zone furnace for horizontal Bridgman growth of CZT: (1) quartz ampoule; (2) boat; (3) seed; (4) cadmium reservoir [37].

materials. The boat (vitreous carbon or silica) is placed in a silica ampoule, which is sealed under vacuum or argon. A post-growth cooling cycle ($\sim 5^\circ\text{C/h}$) is used to reduce mechanical stress and the formation of dislocations. Further details of the growth process may be found in the literature [37].

The modified horizontal Bridgman method has yielded material of high quality. At this point boule sizes are somewhat smaller than obtainable with HPB, but usable wafers can be relatively large. For example, single crystal wafers of $40\text{ mm} \times 38\text{ mm} \times 5\text{ mm}$ have been produced. Yields are also relatively high compared to HPB material; the yield of $20\text{ mm} \times 20\text{ mm}$ wafers is about 25–30%. Electrical resistivities of greater than $5 \times 10^9\ \Omega\text{ cm}$, and $(\mu\tau)_e$ values of $1 \times 10^{-3}\text{ cm}^2/\text{V}$ have been reported [7]. While fairly high, the resistivity values are somewhat lower than those reported for material produced by HPB. X-ray rocking curves have typical values of 70 arcseconds [37]. In contrast to HPB-grown material, the dominant low-temperature photoluminescence emissions are characterized by strong donor-to-acceptor recombinations and by weaker near-band-edge excitonic emission [7]. Difficulties at this point include parasitic vapor growth, bubble formation, and twinning.

Encouraging results have also been obtained using the Bridgman process in its classical vertical configuration. Growth is conducted within sealed and evacuated quartz ampoules generally with the charge in pyrolytic boron nitride crucibles. A multi-stage furnace is used to establish a four-segment temperature profile. Ampoule sizes up to 80 mm in diameter have been reported with boules up to 3.5 kg [54]. Formulations with x in the region of 0.04–0.2 have been reported. The charge may be prepared in situ with the Te in the crucible (in the lower end of the ampoule), the Cd in a quartz reservoir (near the top of the ampoule), and Zn in either container. Alternatively, the compounding is conducted via vapor transport in a separate carbon coated ampoule and later loaded into the growth ampoule. Both compounding and growth take place in excess Cd to produce a vapor pressure of about 1 atm as a means of avoiding significant deviations from stoichiometry. The Cd over-pressure is maintained by controlling the upper furnace at a temperature of 825°C or less. Post-growth annealing, used in some instances [5], is conducted at temperatures between 600 and 850°C . Further details on the furnace design and process parameters can be found in the literature [54–56].

The quality of the material produced by this low pressure Bridgman process is generally comparable to HPB grown material and exceeds it in some areas. X-ray rocking curve widths of about 8 arcseconds (Cu K α radiation) have been reported [55]. Etch pit densities (EPD) in the low 10^4 cm^{-2} region have been reported [5]. EPD values can be substantially higher (10^5 – 10^6 cm^{-2}) near the surface of the crystal in the region adjacent to the ampoule [55]. There is an indication that lower EPD are associated with material growth in pyrolytic boron nitride, compared to ingots grown in carbon-coated quartz [54]. Te precipitates in the region of $(2\text{--}5) \times 10^3\text{ cm}^{-2}$ have been reported on an axially cut wafer. The precipitates were found to be smaller (~ 6 – $10\ \mu\text{m}$ diameter) from regions nearer the ampoule wall than from the central portion of the boule, where they were found to be about 25–35 μm [55].

Higher quality material (for radiation detector applications) was obtained when boules received post-growth thermal processing. In such material both electron and hole traps and their concentrations may be lower relative to HPB material [5,6]. Electrical resistivities as high as $2 \times 10^{11}\ \Omega\text{ cm}$ have been reported for processed samples as opposed to $5 \times 10^8\ \Omega\text{ cm}$ for unprocessed samples. It is interesting to note that the $\mu\tau$ product for holes has been measured to be within a factor of two of the value for electrons ($1.1 \times 10^{-4}\text{ cm}^2/\text{V}$) [5]. If accurate, this has important consequences in terms of detector performance as energy resolution is optimal for equal charge collection efficiencies [57]. It is possible that the post-growth processing changes the nature of the deep level traps from predominantly hole traps to predominantly electron traps, which has the effect of decreasing the electron lifetime and increasing the hole lifetime.

Recent progress on modified vertical Bridgman grown $\text{Cd}_{1-x}\text{Zn}_x\text{Te}$ has resulted in doped crystals with electrical resistivities of $(3\text{--}10) \times 10^9 \Omega \text{ cm}$. Exceptionally high values of $(\mu\tau)_e$ of between $(3\text{--}11) \times 10^{-3} \text{ cm}^2/\text{V s}$ were measured for the crystals [58]. These high values of $(\mu\tau)_e$ and ρ have allowed for the production of co-planar grid detectors with active columns of 1 cm^3 and larger. Planar detectors with thickness of up to 25 mm were also fabricated. Energy resolutions of about 6–7% were reported for 122 keV radiation and peak-to-valley ratios of over 50 were observed at this energy. Pixellated detectors were also produced from the material. Nuclear spectroscopic tests of 122 keV showed good uniformity, and energy resolutions of about 3% were observed for $2 \text{ mm} \times 2 \text{ mm}$ pixels and 5 mm thick devices [59,60]. The peak channel positions of the 5 mm thick pixels were found to vary by less than 1% [59,61]. Yields of over 70% were measured for planar detectors having $(\mu\tau)_e > 3 \times 10^{-3} \text{ cm}^2/\text{V s}$ [58]. Crystals as large as 150 cm^3 were grown; a photo of one ingot which is composed of two large single crystals is shown in the bottom photo of Fig. 7. These developments will stimulate great interest in the use of low-pressure Bridgman to grow detector grade CZT crystals.

On a cautionary note the reader is advised that the encouraging results reported to date for low-pressure grown CZT are based on a relatively small number of ingots and more data is clearly needed. The metric for commercial detector-grade CZT crystals is still based on materials grown by the HPB method, particularly for the case of large-volume gamma-ray and low-energy X-ray detectors.

2.2.4. Physical vapor transport

Physical vapor transport (PVT) has successfully grown a number of binary compounds used in radiation detection, including HgI_2 [62–64], and CdTe [65–69]. The method has, in principle, a number of advantages over melt growth techniques. The lower growth temperature and minimal contact area with the containment vessel have the potential of reducing impurity levels and stress-related imperfections. In addition, it should be possible to achieve greater uniformity and better control of the stoichiometry. The method is amenable to either seeded or unseeded growth. As with melt growth a number of variations of the basic method have been developed. In general, the method is characterized by relatively slow growth rates and, in the case of CZT, by smaller boules.

Despite significant thermo-chemical and kinetic complications, PVT has been applied with some success to the growth of CZT. Some of the problems have been investigated by Palosz et al. [70,71]. An example of a PVT growth system for CZT is shown schematically in Fig. 10. This variation, due to Melnikov [72], features a light guide (4) to cool the crystal. Other structural elements include a tubular quartz housing (1), growth chamber (3), quartz tube (9), and quartz plate (10). Provisions are made for evacuation of the vessel and back-filling with an inert gas (2). A single crystal seed (7) can be positioned on the light guide. Thermal energy is supplied by a tubular multi-section electric furnace (not shown).

Growth temperatures for PVT of CZT are typically in the region of 900–1050°C. A critical process parameter in PVT is the undercooling (ΔT), which is the temperature difference between the source material and the growing crystal. While large undercooling values ($\Delta T > 10^\circ\text{C}$) stimulate more rapid crystal growth, improved compositional homogeneity is found with lower values ($\Delta T \approx 1\text{--}2^\circ\text{C}$) [45,46,71]. Growth rates in the range of 0.05–3.5 mm/h have been reported [71,72]. As with the Bridgman method, controlled post-growth cooling is frequently employed. For example, typical cooling rates are about 1000–200°C in 6.5 h, or from 1000 to 800°C at a rate of 10°C/h followed by a 20°C/h phase. Boule sizes up to 50 mm in diameter have been reported [72,73], although diameters in the region of 10–20 mm are more typical. These sizes are considerably smaller than those obtainable using the Bridgman method.

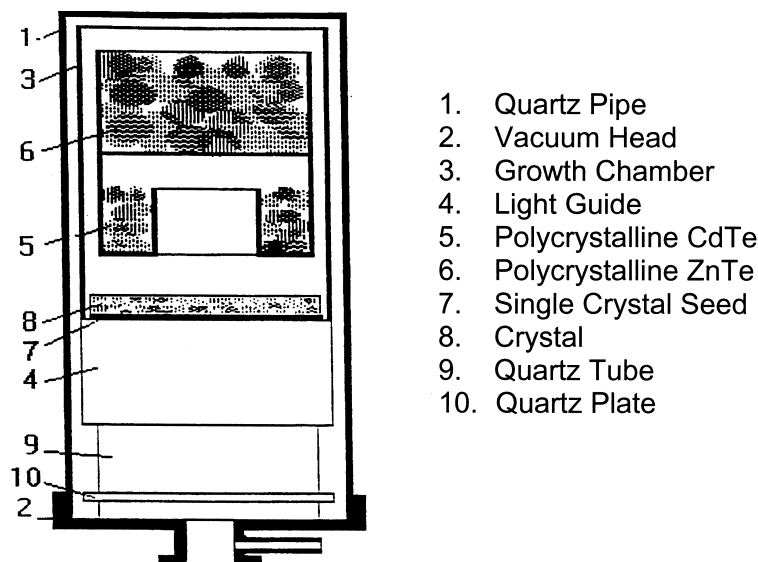


Fig. 10. Schematic diagram of physical vapor growth apparatus [72].

Boules grown by the PVT method are often characterized by high compositional uniformity. Szczerbakow et al. [45] using both X-ray and photoluminescence techniques found variations in x over a boule to be in the region of 0.001. There is evidence that twinning may be more prevalent in CZT than in cadmium telluride grown under similar conditions. Resistivity values range from 10^7 [46] to $8 \times 10^{10} \Omega \text{ cm}$ [72]. We note that resistivity values less than about $10^9 \Omega \text{ cm}$ are generally too low for several spectroscopic applications of the material, particularly for those in the low-energy X-ray region where low leakage is required. Etch pit densities (EPD) have been reported from as low as 10^4 [46] up to $5 \times 10^5 \text{ cm}^{-2}$ [74,75]. Tellurium precipitates, which are common in melt grown material, are present in at least some PVT grown samples [75].

2.3. Crystalline perfection and structural defects

Structural defects are known to strongly influence the performance of semiconductor devices [29,51]; for example, subgrain/twin boundaries lead to high dark current in HgCdTe based IR devices [76], and orthogonal arrays of misfit dislocations in InGaAs based high electron mobility transistors lead to lower channel conductivity [77]. Only a few studies involving X-ray diffraction analysis of HPB $\text{Cd}_{1-x}\text{Zn}_x\text{Te}$ exists in the literature [42,78,79]. These studies used double crystal X-ray diffraction (DCD) technique, which cannot separate the effects of peak broadening due to tilt and strain. Doty et al. [42] reported an average DCD FWHM value of 14 arcseconds for $\text{Cd}_{0.96}\text{Zn}_{0.04}\text{Te}$, and average etch pit density of $1 \times 10^4 \text{ cm}^{-2}$. Johnson [78] reported DCD FWHM values ranging from ~ 20 to 120 arcseconds on HPB CdTe crystals. However, neither study reported a relationship between the X-ray diffraction results and detector performance, since the FWHM values reported using the DCD technique do not necessarily represent the true crystal quality (i.e. do not always measure solely the amount of lattice tilt), particularly if significant lattice strain (lattice parameter variation) exists within the probed volume. Furthermore, this may be the main reason why no correlation between DCD FWHM values and etch pit density (EPD) has been established (e.g. [80]), whereas as is discussed below, a correlation between triple axis X-ray diffraction (TAD) ω -scan FWHM and EPD is clearly observed [81].

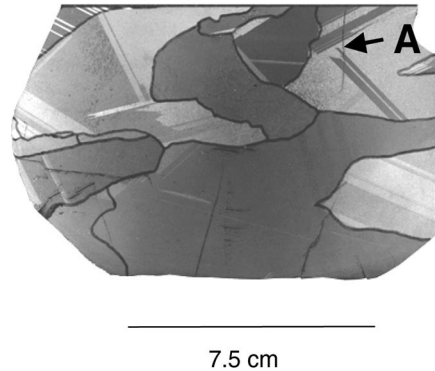


Fig. 11. Optical photograph of an axially sliced (exactly along the growth direction) HPB $\text{Cd}_{1-x}\text{Zn}_x\text{Te}$ wafer with some of the grain boundaries outlined in black. Cracks are also visible; they originate from the edge of the wafer and propagate inward through grains and twins (as marked by “A”).

Current HPB $\text{Cd}_{1-x}\text{Zn}_x\text{Te}$ ingots commonly contain gross structural defects including cracks and grain/twin boundaries, which are readily observable by visual inspection and can be observed in more detail by infrared transmission images. Other extended defects, which are not so readily apparent, include mosaic structure, small angle tilt boundaries, and dislocations; these defects are found within individual grains (i.e. single crystal regions).

2.3.1. Cracks

Cracks represent one of the major macroscopic structural defects in HPB $\text{Cd}_{1-x}\text{Zn}_x\text{Te}$. In a recent report [82] by a manufacturer of HPB $\text{Cd}_{1-x}\text{Zn}_x\text{Te}$, cracks were identified as lowering the yield of useable material by as much as 25%. Cracks result from excess thermal stress, most likely during the crystal cool-down period [50]. Cracking after growth is evidenced by the fact that the cracks propagate through grains and twins, for example, as marked as “A” in Fig. 11. The cracks are typically a few cm in length and $\sim 25\ \mu\text{m}$ in width, and they originate at the edge of the crystal (i.e. at the crucible/crystal interface) and propagate inward towards the center of the ingot. Excess stress is likely to develop from adhesion between the crystal and the crucible wall [82] as the crystal cools and these locations serve as sites for fracture and crack propagation. Cracking can also result from stress during the slicing and dicing of the material [83].

In addition to serving as locations where the crystal may fracture, the free surface areas associated with the cracks can act as nucleation sites for secondary phases such as precipitates and impurities. Chemical analysis of the cracks [84] using X-ray energy dispersive spectroscopy showed increased signals from elements such as carbon and zinc (the graphite crucible is a likely candidate for the source of carbon). Such accumulation of metallic impurities, which have orders of magnitude lower resistivity than the bulk $\text{Cd}_{1-x}\text{Zn}_x\text{Te}$, is likely to influence the local electrical properties at or near the regions of accumulation.

The cracks are readily identified by infrared transmission imaging as shown in Fig. 12 with arrows pointing to the cracks. The cracks appear dark (black) in the infrared because of the scattering due to the irregular and rough surfaces as well as the secondary phases accumulated near the cracks. It is also noted that the cracks often project through the thickness of the wafer (0.55 cm) at various angles and depth; however, some of the cracks do not project entirely through the thickness of the wafer. Microcracks have also been observed by Heffelfinger et al. [84]; they propagate along certain high-symmetry crystal planes. Better understanding and control of the thermal environment have led to large decreases in the density of cracks, and many ingots now exhibit no cracking based on IR transmission.

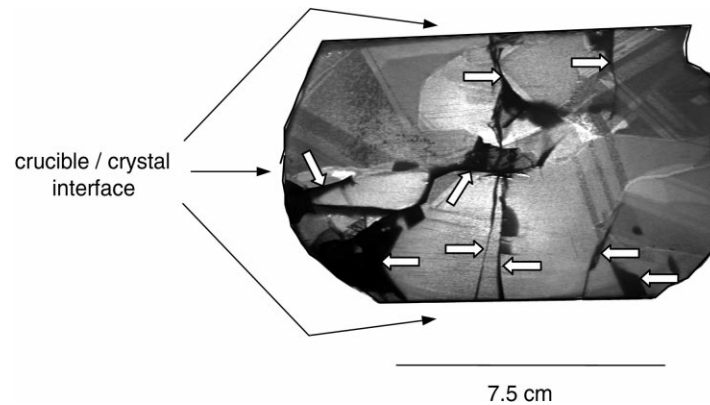


Fig. 12. Infrared transmission image of the same $\text{Cd}_{1-x}\text{Zn}_x\text{Te}$ wafer shown in Fig. 11 with the major cracks identified with arrows.

2.3.2. Grain and twin boundaries

The crystallographic surface orientations of various grains of axial $\text{Cd}_{1-x}\text{Zn}_x\text{Te}$ wafers have been determined using the back reflection X-ray Laue technique [85]. An example is summarized in Fig. 13, in which (a) shows the spatial locations at which Laue measurements were performed, and (b) shows the surface orientations on a standard stereographic triangle. Similar analyses have been

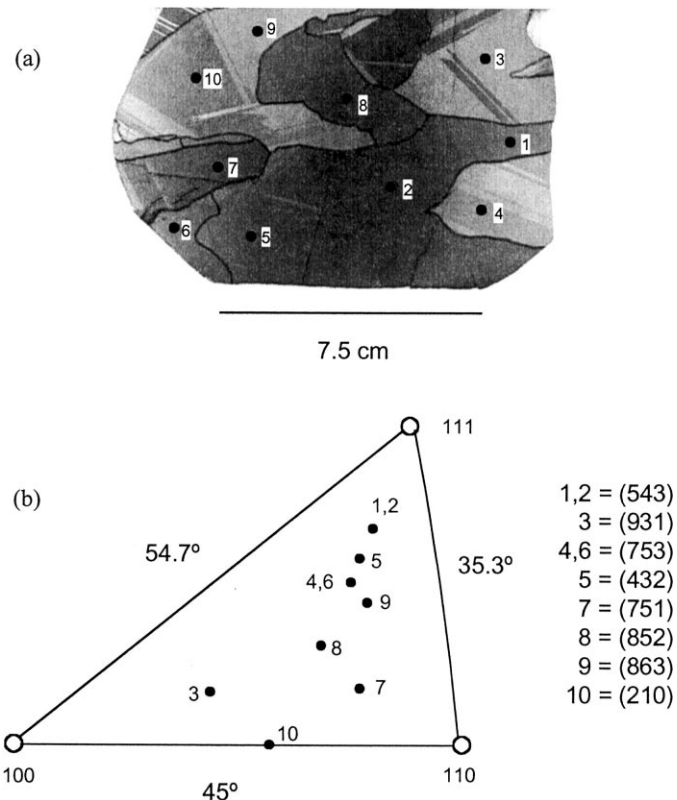


Fig. 13. (a) Locations where Laue measurements were performed and (b) stereographic analysis of the surface orientations of the grains.

performed on numerous wafers to determine whether a preferred growth direction existed but no clear trend has been observed.

The grain and twin boundaries are easily identified visually only when the wafer surface is rough such as in the “as-sawn” surface or a roughly lapped surface. This is because the rough surfaces enhance the direction of the light scattered from the different crystallographic orientations. The wafer shown in Fig. 11 has an “as-sawn” surface, and hence the grain and twin boundaries can be easily observed. However, on finely polished and/or etched surfaces or crystals with electrical contacts (Au or Pt) deposited on the surfaces, identifying the locations of the boundaries by visual inspection becomes difficult, if not impossible. In this case, because lapping the surfaces would be a destructive approach, X-ray topography serves as a convenient and nondestructive technique to locate the boundaries. This is illustrated in Fig. 14 in which a double crystal X-ray topography of a section of the axial $\text{Cd}_{1-x}\text{Zn}_x\text{Te}$ wafer is shown. The rocking curve of the sampled area is also shown, and the topography exposure was made at the peak of the rocking curve. Again, the significance of showing this example is to illustrate the usefulness of the X-ray topography technique in identifying the locations of the boundaries so that a correlation study can be made to the results of detector spatial mapping measurements.

2.3.3. Tilt boundaries and mosaic structure

Fig. 15 shows a triple axis X-ray diffraction (TAD) ω -scan mapping of a (1 1 1) oriented single crystal $\text{Cd}_{1-x}\text{Zn}_x\text{Te}$ [86]. A single measurement probes an area of about $5 \text{ mm} \times 2 \text{ mm}$ (as indicated

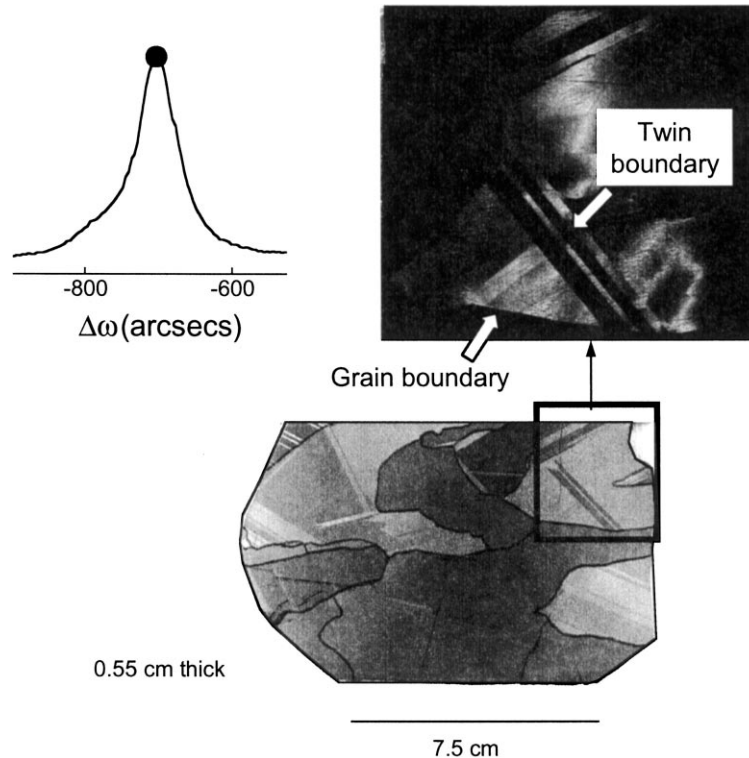


Fig. 14. Double crystal X-ray topography (white = diffracted intensity) of a section of the axial $\text{Cd}_{1-x}\text{Zn}_x\text{Te}$ wafer clearly reveals the grain and twin boundaries. The boundaries are not visible on wafer surfaces which are finely polished and/or etched, and X-ray topography offers a nondestructive means to identify the exact spatial locations of the boundaries from such surfaces [81].

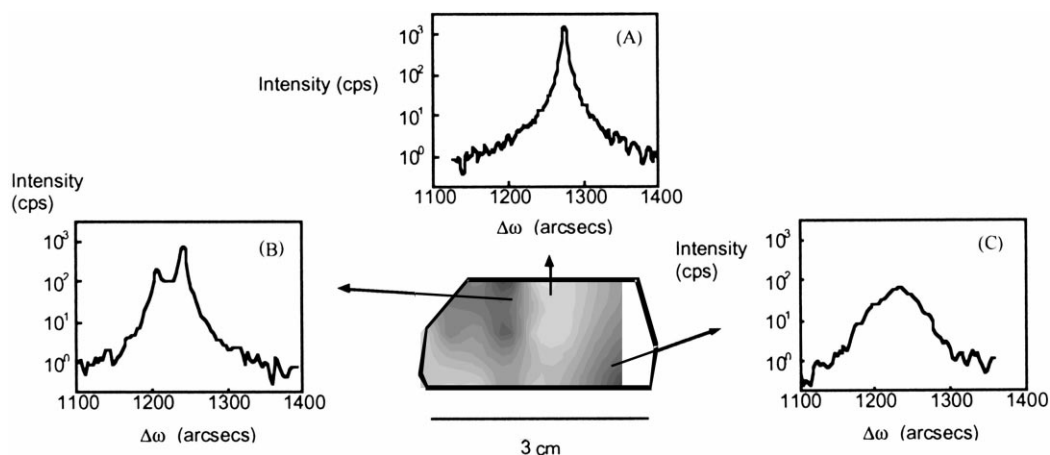


Fig. 15. Triple axis diffraction ω -scan mapping of a (1 1 1) oriented $\text{Cd}_{1-x}\text{Zn}_x\text{Te}$. The light and dark regions correspond to low and high FWHM values, ranging from 8 to 50 arcseconds. Also shown are individual scans representative of regions of high crystal quality (A), low angle tilt boundary (B), and mosaic structure (C) [86].

by the rectangle), and multiple measurements are performed across the entire crystal surface to generate the map. The greyscale contours represent full width at half maximum (FWHM) values of the TAD ω -scans (light = low FWHM; dark = high FWHM); the low and high values for this particular sample are 8 and 50 arcseconds, respectively. All measurements were performed using the (3 3 3) reflection. Three example TAD ω -scans are also shown that illustrate the various features of the ω -scans, and the results are summarized in Table 1 below.

The FWHM of the ω -scan revealing the tilt boundary is measured as the angular separation between the half intensity of the left peak to the half intensity of the right peak. As a comparison, under the same experimental conditions, a typical silicon crystal exhibits a single narrow peak of $\text{FWHM} = 3.5$ arcseconds using the (0 0 4) reflection.

The variations in the crystal quality as indicated by the FWHM values are presumed to stem from the non-optimal thermal stress induced during crystal growth. If this is indeed the case, the crystallinity variation “pattern” measured from the surface (several microns depth) is likely to project through the thickness of the crystal (~ 2.5 mm thick). This was verified by repeating the TAD ω -scan measurements after etching away ~ 100 nm as well as measuring the back sides of the crystals. The results indeed showed the crystallinity variation pattern to project through the thickness of the crystal [81].

Although the TAD ω -scan mapping provides a great deal of information, the spatial distribution of the crystalline quality can be measured by double crystal X-ray topography [81,87]. A combination of these two techniques provides an even more powerful means to characterize the crystalline perfection of single crystal wafer regions. The double crystal X-ray topographs shown in

Table 1

Summary descriptions of the three TAD ω -scans shown in Fig. 15

TAD ω -scan representing	FWHM (arcseconds)	Characteristic feature
(A) High crystal quality	8	Single, narrow peak
(B) Tilt boundary	50	Two (or more) resolvable peaks
(C) Mosaic structure	45	Single, broadened peak

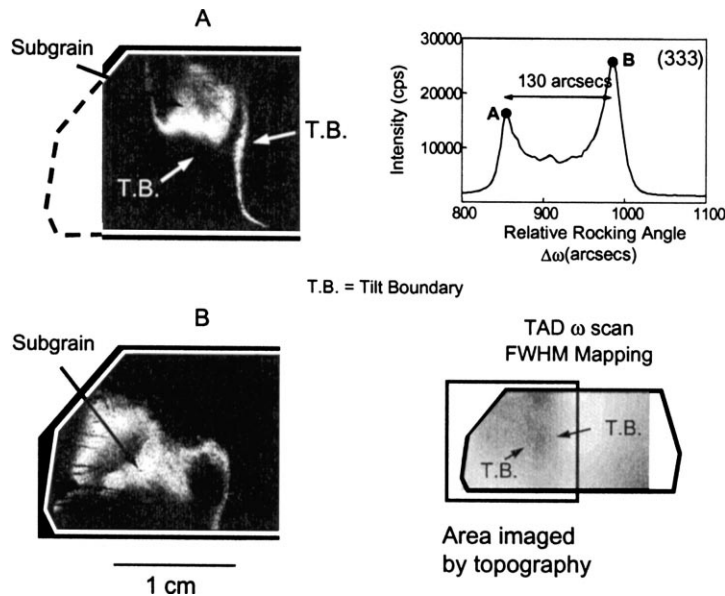


Fig. 16. Double crystal X-ray topographs (white = diffracted intensity) of a single crystal $\text{Cd}_{1-x}\text{Zn}_x\text{Te}$ (same sample shown in Fig. 15). The two exposures (A and B) were taken at the top of the two peaks shown in the rocking curve.

Fig. 16 illustrate how they can provide, for example, the locations of tilt boundaries and delineate subgrains within single crystal CZT. The two topographs (white = diffracted intensity) labeled A and B were taken at the top of the two peaks shown in the rocking curve. The two subgrains as indicated in the figure are separated by 130 arcseconds (0.0361°). Locations of tilt boundaries are also indicated by arrows and the results are consistent with the TAD ω -scan FWHM mapping, also shown in the figure.

2.3.4. Etch pit density

Etch pit density (EPD) measurements have been performed on (1 1 1) oriented $\text{Cd}_{1-x}\text{Zn}_x\text{Te}$ samples using the Nakagawa etch [88], which consists of HF , H_2O_2 , and H_2O , and is routinely used to reveal dislocations that terminate on (1 1 1) \AA surfaces of CdTe and $\text{Cd}_{1-x}\text{Zn}_x\text{Te}$. Fig. 17 shows two EPD micrographs taken from the same sample shown in Fig. 16 of (a) high EPD, $\sim 1 \times 10^5 \text{ cm}^{-2}$ and (b) low EPD, $\sim 2 \times 10^4 \text{ cm}^{-2}$ from the regions as indicated on the TAD ω -scan FWHM mapping. Fig. 17 also shows the TAD ω -scan FWHM values from the same regions. These results are representative of most EPD measurements: EPD values of $\sim 10^5$ and $\sim 10^4 \text{ cm}^{-2}$ are typically observed in crystal regions that exhibited TAD ω -scan FWHM greater than ~ 40 arcseconds and less than ~ 10 arcseconds, respectively. As a comparison, high quality GaAs that exhibits TAD ω -scan FWHM of ~ 5 arcseconds has EPD of less than 10^3 cm^{-2} . Table 2 summarizes these results.

Table 2

Summary of the typical correlation between TAD ω -scan FWHM and EPD

	TAD ω -scan FWHM (arcseconds)	EPD (cm^{-2})
High quality $\text{Cd}_{1-x}\text{Zn}_x\text{Te}$	<10	$\leq 1 \times 10^4$
Low quality $\text{Cd}_{1-x}\text{Zn}_x\text{Te}$	>40	$\geq 1 \times 10^5$
High quality GaAs (for comparison)	4	$\leq 1 \times 10^3$

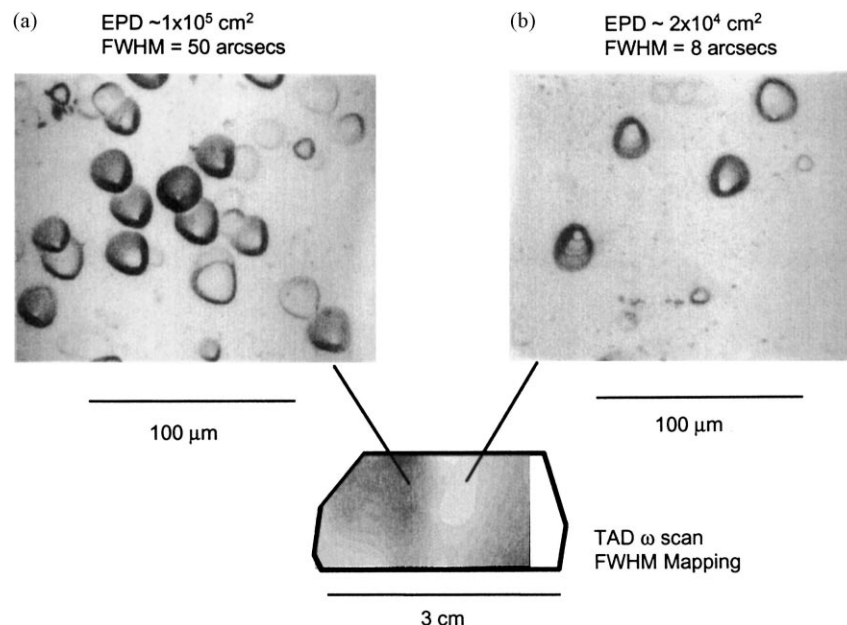


Fig. 17. Nakagawa etch pit density optical micrographs comparing crystal regions with (a) high ($\sim 1 \times 10^5 \text{ cm}^{-2}$) and (b) low ($\sim 2 \times 10^4 \text{ cm}^{-2}$) dislocation density. (a) and (b) were measured on the same $\text{Cd}_{1-x}\text{Zn}_x\text{Te}$ sample as shown in Fig. 16 from regions that exhibited high and low FWHM, respectively.

Since dislocations induce local lattice tilting, the broadening of the TAD ω -scans in regions of low crystal quality can be attributed to the presence of dislocations. Further, this correlation has the implication that the TAD ω -scans can be used as a non-destructive tool (as opposed to the EPD measurements) to uniquely assess the crystalline perfection of $\text{Cd}_{1-x}\text{Zn}_x\text{Te}$.

2.3.5. Purity data

Impurities in CZT and their relationship to transport properties are of considerable interest and have been studied in some detail. However, this work has been complicated by wide variations in the measured values and the importance of how the contaminant is distributed in the lattice (i.e. point defects, complexes or inclusions). Results typical of impurity contents are shown in Table 3 [89]. These values were obtained from a HPB sample grown from relatively low purity (5–6N) using

Table 3
GDMS analysis of a first-to-freeze segment of HPB grown $\text{Cd}_{1-x}\text{Zn}_x\text{Te}$

Element	ppmw	Element	ppmw	Element	ppmw
Li	0.010	Ca	0.041	Ga	0.42
B	0.004	Ti	0.002	As	0.005
Na	0.16	V	0.0003	Se	0.69
Mg	0.47	Cr	0.021	Ag	<0.05
Al	450	Mn	0.088	In	<0.1
Si	0.020	Fe	1.0	Sn	<0.03
P	0.10	Co	0.004	Sb	<0.03
S	0.84	Ni	0.047	Pb	<0.005
K	0.005	Cu	0.036	Bi	<0.005

Al-doped starting material. All results are given in ppm by weight. Elemental analysis has also been done by inductively-coupled plasma source quadrupole mass spectroscopy (ICP-MS) [90] and also by secondary ion mass spectroscopy: the subject of numerous investigations. The impurities can originate from a variety of sources, such as the starting material, the transfer process, the containment vessel, fabrication procedures, and storage and handling, or a combination of these steps. Analyses are typically carried out using glow discharge mass spectrometry (GDMS) or inductively-coupled plasma mass spectrometry (ICP-MS). The minimum detection limits are typically in the few to tens of parts per billion range. Interpretation of the impurity data, particularly as it relates to the role of a specific contaminant on detector.

We note that the results of Table 3 are from the first to freeze segment of the boule and, in general, will not be representative of values at other positions along the axial (growth) direction due to segregation effects (see Section 3.1 and the following section). Apart from the major constituents and the dopant Al, the most abundant impurity is seen to be Fe. Other transition elements are also present but generally at concentrations below the ppm level. In addition a number of elements from groups IIIA, VA, and VIA regularly appear. Aluminum in the undoped material appears typically near the 1 ppm level, or less.

3. Materials characterization

3.1. Composition and nonuniformity

In slow, near-equilibrium melt growth methods such as high-pressure Bridgman, the concentration of an impurity in the crystalline phase differs from that in the melt due to thermodynamic considerations [91]. The ratio of concentration of a given atomic species in the solid phase to that in the liquid phase at equilibrium is called the segregation coefficient for that element and is denoted by K . The segregation coefficient for zinc in CdTe has been reported as approximately 1.35 [92]. Because $K > 1$, the zinc concentration in the solid is greater than that in the melt at the moment that portion of the crystal freezes; hence zinc is progressively depleted from the melt and the zinc concentration in the solid steadily decreases during growth. A simple model can be used to predict the zinc concentration as a function of position along the growth axis and this yields an expression for the zinc concentration, x [93]:

$$x(g) = Kx_0(1 - g)^{K-1} \quad (14)$$

where $g = N/N_0$ is the molar fraction of the original material which has crystallized, and x_0 is the zinc concentration in the initial melt. This equation is known as the normal freeze equation and describes the steady decline in zinc content as one moves along the growth axis of the boule. It is important to note that as one approaches the heel (last-to-freeze end) of the boule, not only does the average zinc concentration decrease, but the magnitude of the concentration gradient increases. That is, the material from near the heel has a large, inherent composition non-uniformity. In infrared detector substrate applications control of composition is important in order to maintain lattice matching. Some success in reducing zinc segregation along the growth axis has been achieved by controlling the partial pressures of Cd and Zn in the growth atmosphere [94] or by placing a solid source in contact with the melt [95]. Such measures have not been applied to nuclear radiation detector material.

Zn concentration used for radiation detectors has been primarily determined by the compositions that can be grown by the techniques at hand in high quality and in reasonable yields for commercial applications. Little work has been done to determine the optimum Zn composition for detector applications. The Zn concentration variation does change the average atomic number of the material (Zn being lower in atomic number than Cd), however, the change in bandgap with Zn variation is likely to be a much more significant effect on detector performance. Toney et al. [96] have investigated on a theoretical basis what the optimum Zn concentration (optimum bandgap) would be for room temperature nuclear detectors based on the effect that the Zn content has on bandgap and hence on noise and charge generation statistics. They conclude that for optimal performance a bandgap of about 2.0 eV would be best for planar geometry detectors, depending on photon energy, and this corresponds to a Zn fraction of 0.7–0.8. This work, however, ignores the very real practical limitations associated with growing this material. Yoon et al. [97] investigated the variation of resistivity of $\text{Cd}_{1-x}\text{Zn}_x\text{Te}$ along an ingot slice. They found that while the Zn concentration varied as expected according to the normal freeze behavior the resistivity did not vary in the same manner. Indeed, the “expected” relationship of higher resistivity with higher Zn concentration was not observed. In general, therefore, they concluded that the resistivity was controlled in $\text{Cd}_{1-x}\text{Zn}_x\text{Te}$ by a compensation mechanism involving both deep and shallow level defects in the material.

Impurities in CZT also segregate toward the top or heel of the ingot, depending on the value of the segregation coefficient for each element. Values for the segregation coefficient of several elements have been measured [79]. Most of the impurities tend to segregate toward the heel, causing the impurity content to be relatively high in the last-to-freeze position of the ingot.

3.1.1. Low-temperature photoluminescence spectroscopy

A typical 4.2 K photoluminescence (PL) spectrum for $\text{Cd}_{1-x}\text{Zn}_x\text{Te}$ is shown in Fig. 18. It consists of several regions [98]:

1. Near band-edge region: consisting of free and bound exciton peaks.

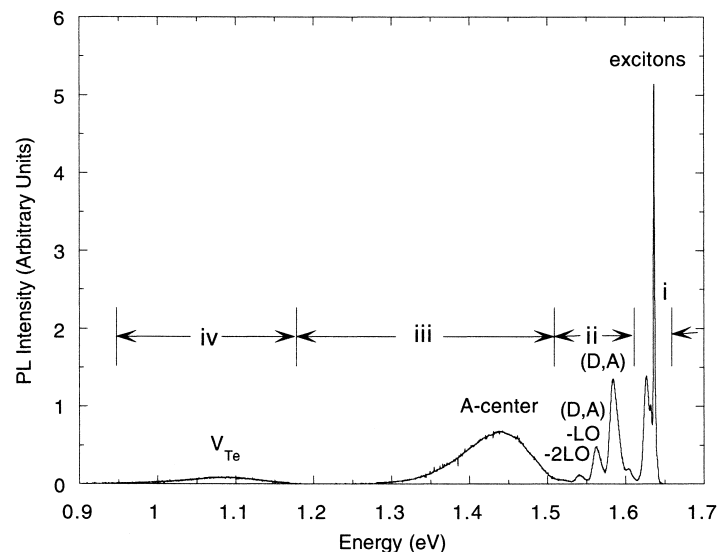


Fig. 18. Representative 4.2 K photoluminescence spectrum for $\text{Cd}_{1-x}\text{Zn}_x\text{Te}$ with $x \sim 0.1$. This spectrum includes (i) excitonic luminescence, (ii) donor–acceptor transitions, and (iii, iv) defect-related bands [193].

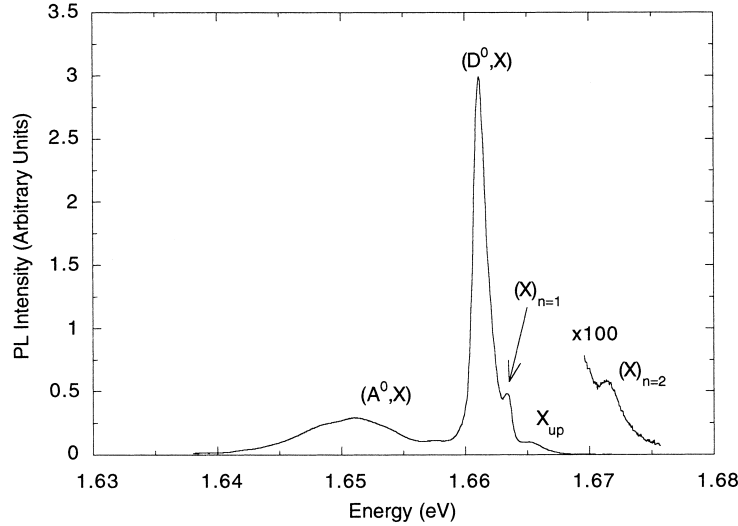


Fig. 19. Near-band-edge PL spectrum for a high quality $\text{Cd}_{1-x}\text{Zn}_x\text{Te}$ sample with $x \sim 0.1$. Visible are donor-bound (D^0, X) and acceptor-bound (A^0, X) excitons, ground state ($\text{X}_{n=1}$) and first excited state ($\text{X}_{n=2}$) free excitons, and upper polariton bands (X_{up}) [17].

2. Donor–acceptor region: consisting of a (D, A) transition and its first two phonon replicas. The phonon replicas of the excitonic luminescence also lie in this region.
3. A defect band centered at 1.4 eV of uncertain origin but ascribed by consensus to the A-center, which is a Cd vacancy in complex with a donor.
4. A band centered at 1.1 eV believed to be related to tellurium vacancies.

Region (i), the near-band-edge region, contains some of the most useful information in the low-temperature PL spectrum. Fig. 19 shows the near-band-edge spectrum for an especially high quality CZT sample with $x \approx 0.1$. The dominant peak is the donor-bound exciton (D^0, X), in contrast to CdTe and $\text{Cd}_{0.96}\text{Zn}_{0.4}\text{Te}$ grown by other techniques, where (A^0, X) is typically dominant. A ground state free exciton peak ($\text{X}_{n=1}$ or X_1), upper polariton band (X_{up}) and first excited state free exciton ($\text{X}_{n=2}$ or X_2) are also visible. Because of the greater degree of alloy broadening for $x = 0.1$ compared to $x = 0.04$, the free exciton peak is barely resolvable from the donor-bound exciton in this case; in poorer quality material the two peaks are not resolvable at all.

The spacing of the two free exciton peaks can be used to determine the free exciton binding energy. The first and second free exciton peaks in Fig. 19 are at 1.6633 and 1.6714 eV, respectively. Assuming hydrogen-like energy levels yields a value of the ground state energy $E_0 = 10.8$ meV. The donor-bound exciton dissociation energy can be read directly from the spectrum as 2.2 meV, so that the (D^0, X) peak lies 13.0 meV below the bandgap energy. This peak can therefore be used as a reliable indicator of the bandgap, and hence the zinc concentration, provided that a reliable relationship between the bandgap and the zinc fraction is available. The position of the donor-bound exciton peak in the 4.2 K PL spectrum of a longitudinal boule slice is shown in Fig. 20 as a function of distance from the boule tip. It shows a steady shift toward lower energy as one moves away from the tip, as expected based on the smaller bandgap (i.e. lower Zn concentration) and the normal freeze equation. To make a quantitative comparison with the normal freeze equation, one must have a relation between the (D^0, X) peak position, and hence E_g , and the alloy composition, x . Several groups have used photoluminescence in conjunction with X-ray diffraction or X-ray fluorescence to

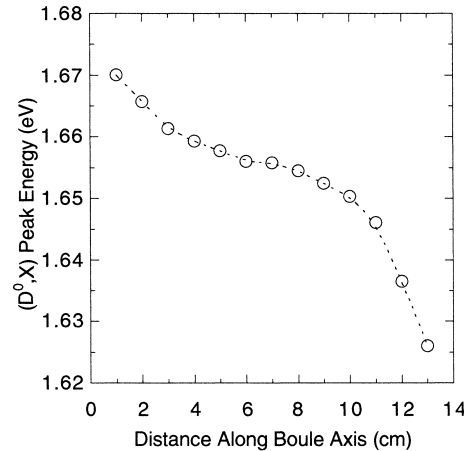


Fig. 20. Peak energy of the donor-bound exciton peak in the 4.2 K PL spectrum as a function of distance along the growth axis for vertical high-pressure Bridgman-grown $\text{Cd}_{1-x}\text{Zn}_x\text{Te}$ with $x_0 \approx 0.1$ [17].

determine a relation for $\text{Cd}_{1-x}\text{Zn}_x\text{Te}$ of the form

$$E_g(x) = E_0 + (\Delta E - a)x + ax^2 \quad (15)$$

where a is the bowing parameter. Unfortunately the published values of the bowing parameter vary substantially, from as low as 0.17 eV [99] to as high as 0.43 eV [100], and there is no obvious basis for choosing one value over the others. It may be that a depends on other parameters, such as residual strain, and must be determined experimentally for each crystal. By calculating x for the data points of Fig. 20 using each of the available equations and comparing the results to the normal freeze equation using a value of 1.35 for the segregation coefficient [92] and a nominal zinc fraction of 0.1 as shown in Fig. 21, it is found that the equation of Magnea et al. [101] provides the best match, while those of

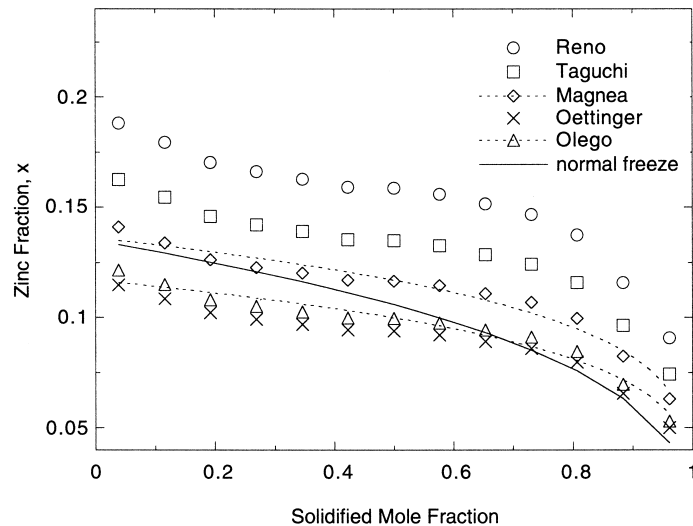


Fig. 21. Measured composition along the growth axis using several $E_g(x)$ relations from the literature compared to the normal freeze equation with $x_0 = 0.1$ and $K = 1.35$ (solid line). A χ^2 -fit (dotted line) gives $K = 1.22$ and $x_0 = 0.11$ (Mangea) or $K = 1.23$ and $x_0 = 0.09$ (Olego) [17].

Oettinger et al. [102] and Olego et al. [99] are also possibilities. The equations of Taguchi [103] and Reno and Jones [100] seem to be ruled out. Whichever equation is chosen, a better fit is obtained with a lower value of the segregation coefficient and a slightly higher or lower value for the nominal zinc concentration. This fact implies a relatively rapid growth, since the effective segregation coefficient decreases toward unity with increasing growth rate [104]. It is also clear that the actual composition profile deviates from the normal freeze profile.

3.1.2. Room temperature photoluminescence spectroscopy

While low-temperature photoluminescence provides a wealth of information about crystal quality and the presence of defect levels, it is somewhat inconvenient and expensive to perform, and the minimum obtainable spot size is relatively large because the sample is enclosed in a cryostat which makes focusing of the laser beam more difficult. A complementary technique that provides information about spatial variation of material properties on a micron scale is room temperature photoluminescence mapping.

To extract material parameters from a room temperature PL spectrum in a systematic way, one requires that the calculated line shapes for various types of transitions be combined. This approach has been used with some success in cadmium telluride [105], but in CZT the variation of the bandgap and phonon energies for different alloy compositions makes it a less tractable problem. A fruitful approach for composition mapping is to relate the peak position in the spectrum to the Zn composition in an empirical way and to recognize that while the extracted value of the zinc fraction may not be accurate, variations can be detected with precision. One difficulty with extracting accurate composition information from room temperature PL spectra is that the peak position depends on the excitation wavelength and intensity. Care must be taken to avoid local heating of the sample by the laser. When the intensities are too high, the heating is greater for higher-energy (blue) photons causing a greater fraction of each photon's energy to be converted to phonons and a larger change in the local bandgap both of which can change the peak position. To reduce the effect of this inaccuracy, composition maps are often expressed in terms of fractional deviation from the mean. The luminescence intensity is also a by-product of the curve fit, so that intensity and composition maps are produced simultaneously.

The most obvious non-uniformity is the systematic variation of zinc content along the growth axis. By performing high-spatial-resolution mapping, one can study the interface shape during growth [106]. A room temperature PL composition map showing zinc segregation along the growth axis of a CZT boule is shown in Fig. 22. In some cases, rather than the steady decline in zinc content expected from the normal freeze equation, a sharp increase in x is seen in a small region at the end. This phenomenon has been explained in terms of supercooling of the melt in the early stages of solidification [49]. Fig. 23 shows a one-dimensional, room temperature PL composition profile illustrating this phenomenon. Even aside from the initial supercooling, the composition profile of Fig. 23 deviates from the normal freeze equation, declining faster than expected near the tip, then remaining nearly constant in the middle before dropping rapidly near the heel. This profile is consistent with diffusion-limited segregation [104] rather than perfect stirring, as is assumed in deriving the normal freeze equation. In addition to the systematic variation in composition along the growth axis, local variations are sometimes seen. Fig. 24 shows two examples. The figure on the right-hand side shows a map that exhibits minute striations, perhaps indicating temperature fluctuations at the growth interface due to convection. The figure on the left shows a map of the adjacent portion of the same sample, showing a large discontinuity, perhaps indicating zinc segregation at a grain boundary or a sudden change in growth conditions.

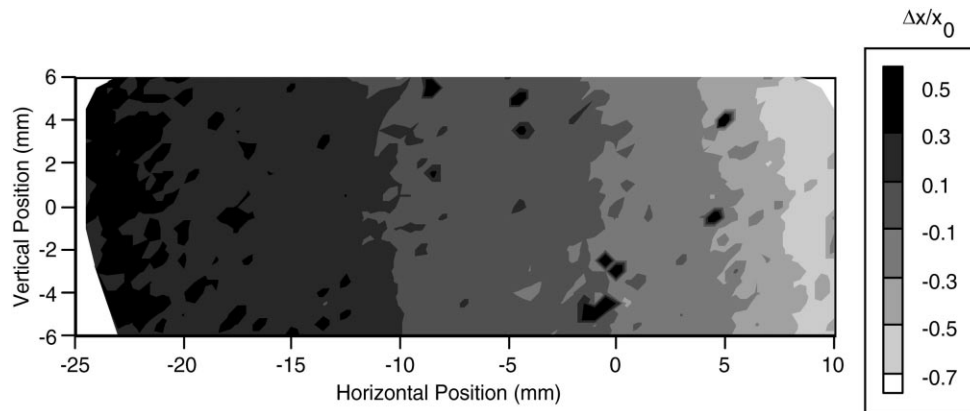


Fig. 22. Room temperature PL composition map for a longitudinal slice of cadmium zinc telluride boule. The steady decrease in zinc predicted by the normal freeze equation is clearly visible. The isolated dark spots are attributed to structural defects. The greyscale shows the deviation in the composition, x , from the average composition x_0 [230].

Photoluminescence mapping has been used for studying structural defects as well as zinc variation. The isolated dark spots seen in composition maps can be attributed to inclusions, probably of tellurium [107]. High-spatial-resolution PL maps of these inclusions show a region of near-zero PL intensity, surrounded by a region in which the bandgap is shifted to higher energy. EDX measurements show no increase in Zn content in or around the inclusions [108] so that the bandgap shift must be attributed to strain that develops as the ingot is cooled due to the difference in thermal expansion coefficients between the inclusion and the surrounding lattice. Fig. 25 shows a map of such inclusions.

3.2. Defect levels and compensation

Incorporation of impurities into as-grown CZT ingots involves (1) the addition of the dopants into the starting materials and (2) the extent to which the dopants are frozen into the ingot. The effect

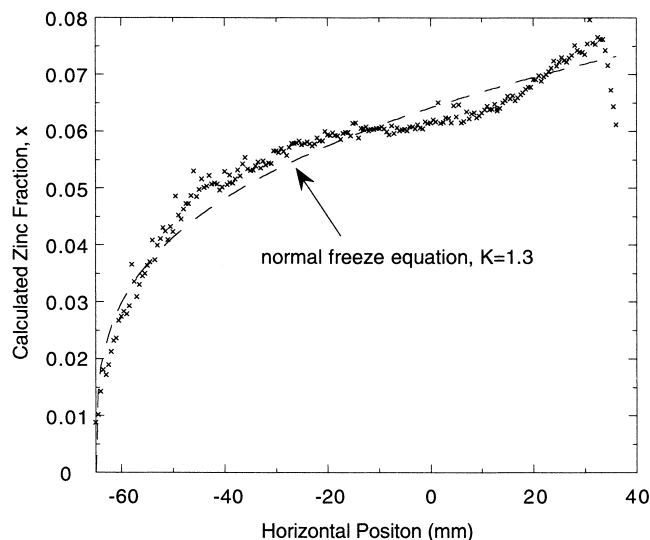


Fig. 23. One-dimensional, room temperature PL composition scan showing deviation from the normal freeze equation due to supercooling in the melt and diffusion-limited segregation [193].

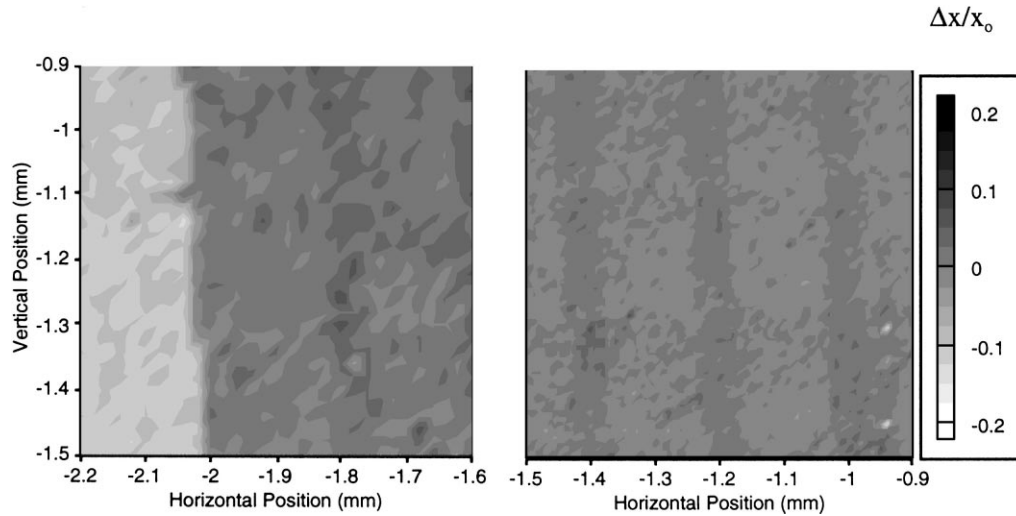


Fig. 24. PL composition maps showing a discontinuity (left) and striations (right). Spatial resolution is 20 μm for the map at left and 10 μm for the map at right [230].

of the dopant(s) on the electrical properties is dependent on its concentration, the lattice site occupied by the dopant, the presence of native defects and other impurities, and gettering of impurities into precipitates and other inclusions.

As discussed in the introduction X-ray and gamma-ray radiation detector applications require that the material have high resistivity and a minimum of carrier traps that contribute to incomplete charge collection and broadening or “tailing” in the photopeak. While $10^9 \Omega \text{ cm}$ and above is desirable, the minimum acceptable resistivity is approximately $10^8 \Omega \text{ cm}$ [109], although the precise value depends on the detector material, pixel size and applied bias. Material that meets this criterion is more properly described as semi-insulating rather than semiconducting. In the case of Ge, high resistivity is achieved by purifying the material of electrically active dopants to the level of $\sim 10^{10} \text{ cm}^{-3}$ and cooling with liquid nitrogen. Several electrically inactive impurities, including Si, C, O and H are present in substantially higher concentrations but do no harm [262]. For most materials purification to such high levels is unrealistic, and it is necessary to introduce dopants or defects that compensate the existing impurities. For compensation to work without excessive

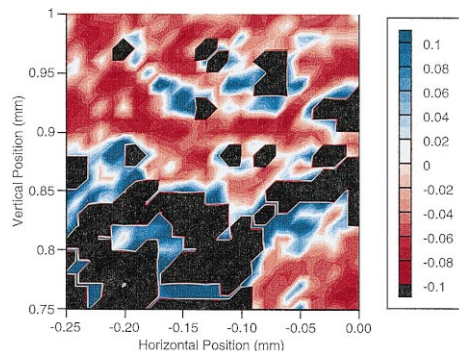


Fig. 25. Room temperature PL map showing inclusions (black) surrounded by regions of higher bandgap (blue). The scale is the deviation of the composition from the mean composition indicated by a value of zero [230].

trapping, there must be a mechanism by which a delicate balance between donors and acceptors can be achieved. The classic example is the use of lithium drifting to compensate boron in silicon, in which the Li atoms diffuse under bias and form neutral complexes with the B acceptors. In most materials, including CdTe and CZT, there is no easy way to achieve a precise balance between shallow donors and acceptors. Instead, compensation is achieved by the presence of deep levels. At the same time deep levels may also act as carrier trapping centers and thus the study of both compensation and carrier traps in CZT is critical in determining the potential of this material as a radiation detector [110].

Because of the importance of compensation and trapping in CZT for nuclear detector applications, and because of a broader interest in semi-insulating materials for applications for epitaxial substrates and electro-optical devices, there is considerable interest in trying to understand the mechanism of compensation. In general, both native defects and impurities can be effective as deep levels. In semi-insulating (SI) GaAs, for example, the deep levels created by the addition of Cr and O cause the compensation of the native defects and impurities, at the expense of significantly decreasing the carrier lifetimes [263]. But, alternatively, by controlling the stoichiometry during growth, one can control the resistivity of GaAs over eight orders of magnitude and grow SI GaAs without the addition of any impurities [111]. Another example of compensation is Fe in InP, in which Fe functions as a deep acceptor level to compensate for unintentional donors. For CZT used as radiation detector materials, significant efforts are in progress to understand and to control the compensation and trapping in the material, but definitive understanding has not been fully reached [50]. At the present time, CZT materials used for radiation detectors are typically grown by the high pressure Bridgman method [40] and under Te-rich conditions. Often, there is deliberate introduction of n-type impurities such as Cl, In, and Al. It is generally accepted that high resistivity in CZT is achieved through the pinning of the Fermi-level near midgap by compensation through a balance between shallow and deep level defects rather than through the growth of intrinsic material. Indeed, it has been reported [112] that attempts to use highly pure starting material to grow intrinsic CZT of high resistivity proved unsuccessful and instead Al was introduced as a dopant to obtain high resistivity. It is also known that high resistivity in CdTe is achieved through compensation and this has been discussed and summarized by Hage-Ali and Siffert [113]. In the case of CdTe, which may be a model for CZT, group III elements such as In and Al [114] on the Cd site have been suggested for compensation. Group VII substitutional impurities on the Te site have also been suggested [115–117]. In addition elements such as Ge, Mg, Se or Zn were also suggested [118] as have been Cu, Fe, and V [119–121].

The effectiveness of deep donors (acceptors) in compensating shallow acceptors (donors) is a consequence of the steepness of the Fermi–Dirac distribution near the Fermi-level. If the deep level is close to the intrinsic Fermi-level, large changes in the occupancy of the level can be achieved by small variations in the Fermi-level. Therefore, the additional free holes (electrons) created by the introduction of shallow acceptors (donors) will be neutralized by further ionization of the deep level. Because the presence of the deep level prevents the Fermi-level from moving significantly from its intrinsic position, this process is sometimes referred to as “pinning” of the Fermi-level.

The limits of compensation by deep levels are apparent from the above discussion. First, a given deep level can only compensate one type of shallow level (either donors or acceptors). For this reason most II–VI semiconductors can be doped easily only in one direction, making fabrication of pn junctions difficult. Second, the concentration of the deep level should be approximately equal to the net concentration of shallow levels depending on the binding energy of the deep defect. If the deep-level concentration is too low, the electrical resistivity will be too low, and if the deep-level concentration is too high, excessive charge trapping is expected. In growth from the melt,

segregation of impurities makes it difficult to maintain compensation over the full length of the boule while being careful to not incorporating too high a concentration of deep levels.

A simple model for compensation by deep levels has been applied to semi-insulating GaAs [122] and CdTe [123], and this same model is applied here to CZT.

The occupancy of the i th acceptor level, taking the top of the valence band as the zero of energy, is

$$f_A^i = \left[1 + g_A^i \exp\left(\frac{E_A^i - E_F}{kT}\right) \right]^{-1} \quad (16)$$

while that for a donor level is

$$f_D^i = \left[1 + g_D^i \exp\left(\frac{E_g - E_D^i - E_F}{kT}\right) \right]^{-1} \quad (17)$$

where $E_{A/D}^i$ is the ground state ionization energy of the acceptor/donor, E_F the Fermi-level, and $g_{A/D}^i$ is the degeneracy factor of the level, which depends on the multiplicities and energies of the excited states of the center [124]. The degeneracy factors are difficult to determine but typically are of order 1.

The concentrations of ionized acceptors and donors are

$$N_A^- = \sum_i f_A^i N_A^i, \quad N_D^+ = \sum_i (1 - f_D^i) N_D^i \quad (18)$$

where N_A^i and N_D^i are the concentrations of the i th acceptor and donor. There is no reason to distinguish between shallow and deep levels in the calculation. The Fermi-level is determined by the requirement of local charge neutrality

$$p + N_D^+ = n + N_A^- \quad (19)$$

In seeking a strictly numerical solution there is no reason to assume full ionization of shallow levels. The only ad hoc assumption which we make is that the Fermi-level is far from the band edges (non-degenerate case) so that the free electron and hole concentrations can be calculated as

$$\begin{aligned} n &= N_c \exp\left(-\frac{E_g - E_F}{kT}\right), \quad N_c = 2 \left(\frac{2\pi m_e^* kT}{h^2}\right)^{3/2}; \\ p &= N_v \exp\left(-\frac{E_F}{kT}\right), \quad N_v = 2 \left(\frac{2\pi m_h^* kT}{h^2}\right)^{3/2} \end{aligned} \quad (20)$$

where N_c and N_v are the effective densities of states in the conduction and valence bands and m_e^* and m_h^* are the electron and hole effective masses. An iterative procedure is used to find the value of E_F that is consistent with charge neutrality. The resistivity of the material is calculated as

$$\rho = \frac{1}{q(\mu_e n + \mu_h p)} \quad (21)$$

where μ_e and μ_h are the electron and hole mobilities, and q is the magnitude of the electron charge. Eqs. (16)–(21) constitute a simple but fairly complete model by to calculate the resistivity of a semiconductor given the energy levels and concentrations of all donors and acceptors. Of course this information is not easy to obtain in practice.

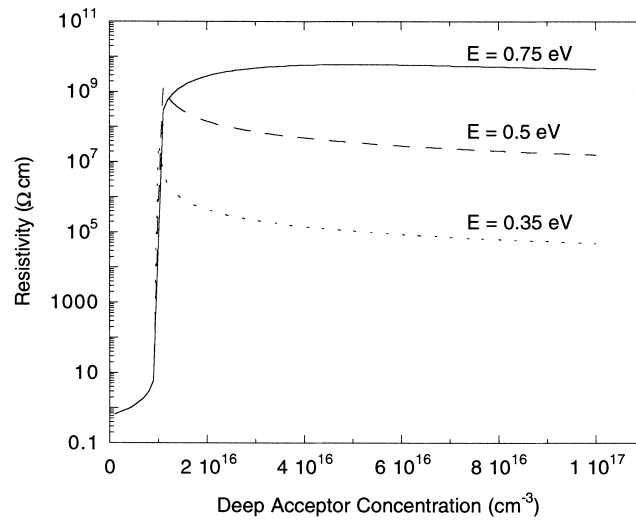


Fig. 26. Resistivity of $n\text{-Cd}_{1-x}\text{Zn}_x\text{Te}$ at 300 K in the presence of a single compensating acceptor as a function of the deep acceptor concentration and energy [193,230].

As an example, suppose that there is a single deep acceptor and that shallow donors outnumber shallow acceptors. The resistivity as a function of N_{DA} , the concentration of deep acceptors, is shown in Fig. 26 for several values of the binding energy, E_{DA} , of the deep level. If N_{DA} is less than the net shallow level concentration, $N_{\text{D}} - N_{\text{A}}$, the material is undercompensated and has high, n-type conductivity. If N_{DA} is very nearly equal to $N_{\text{D}} - N_{\text{A}}$, perfect compensation is achieved and intrinsic resistivity is obtained. If $N_{\text{DA}} \gg N_{\text{D}} - N_{\text{A}}$, the material is overcompensated, and the resistivity is somewhat lower. Note that the closer the deep level is to the intrinsic Fermi-level, the greater is the tolerance for overcompensation.

Fig. 27 shows the inverse resistivity, which is proportional to the leakage current at a given bias voltage, as a function of temperature for the same three trap energies. In analysis of temperature-

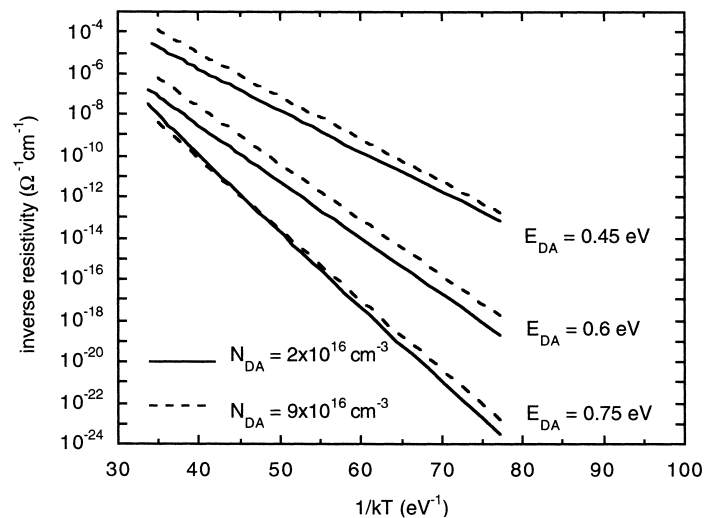


Fig. 27. Temperature dependence of leakage current for $n\text{-Cd}_{1-x}\text{Zn}_x\text{Te}$ with a single compensating deep acceptor. The slope of the curve on a log scale is *approximately* $-E_{\text{DA}}$ but varies slightly with deep acceptor concentration [193].

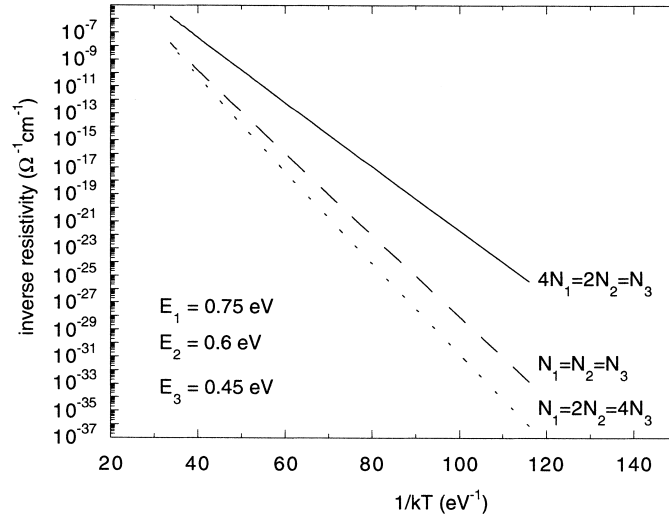


Fig. 28. Temperature dependence of leakage current for n-Cd_{1-x}Zn_xTe in the presence of three deep acceptors in varying combinations. The curve appears as a single line whose slope depends on the relative concentrations of the three deep levels [193].

dependent leakage current data, it is often assumed that a plot of $\ln(I)$ versus $1/kT$ will yield a straight line with slope $-E_{DA}$, but Fig. 27 demonstrates that this assumption is not strictly correct. In particular, the slope depends on the concentration of the deep level (and slightly on the degeneracy factors). Activation energies extracted from this type of data must therefore be interpreted conservatively.

Next we consider the temperature dependence of resistivity in the presence of multiple traps. As shown in Fig. 28, rather than being piecewise linear with the separate slopes corresponding to the several trap levels, the I versus $1/kT$ curve appears approximately linear with a slope between the energies of the traps involved. This fact makes it impossible to distinguish between a single dominant level and two or more levels acting in concert. Lastly, we consider whether the A-center may play some role in compensation. This defect is too shallow (<200 meV) [125] to be a dominant deep-level compensating center. However, if there is a deep center that is present in insufficient quantity to provide compensation on its own, the A-center can play an assisting role by reducing the net shallow defect concentration, as illustrated in Fig. 29 and is discussed further in the sections below.

3.2.1. Electronic point defects in CZT

The primary purpose of this section is to review electronic point defects in CZT and their relationship to electrical properties. Since most of the point defects are common to both CZT and CdTe, recent work on defects of CdTe will also be included. For $x = 0.10$, the typical Zn concentration in CZT for radiation detectors, the bandgap difference between CdTe and CZT is 62 meV at 300 K (from 1510 to 1572 meV) [99]. Since this is only a 4.1% increase, any shift in the ionization energies of defects are expected to be relatively small, and for simplicity we will ignore them. Because there are a multitude of factors relevant to the type and the concentration of defects, the reader is encouraged to consider (1) the growth method, (2) the grower, (3) any doping used, and (4) the Zn concentration, whenever possible.

Although commercially available CZT grown by the high pressure Bridgman method for nuclear detector applications contains Te precipitates, grain boundaries, and twins [108], these

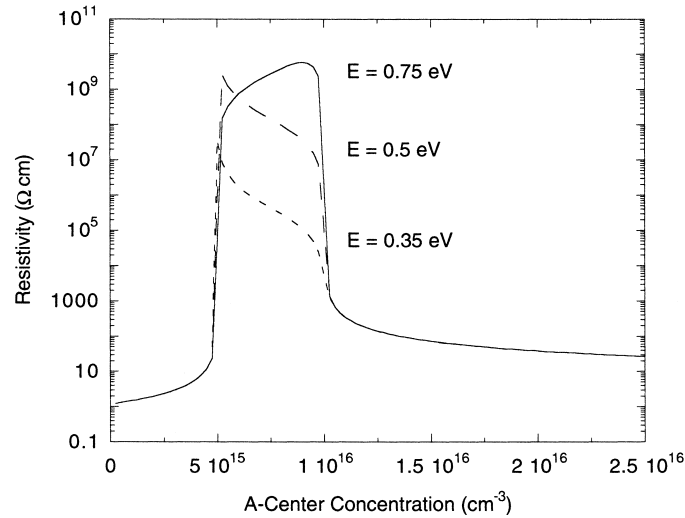


Fig. 29. Compensation of n-Cd_{1-x}Zn_xTe by a combination of a single deep acceptor and A-centers: $N_D - N_A = 1 \times 10^{16} \text{ cm}^{-3}$; $N_{DA} = 5 \times 10^{15} \text{ cm}^{-3}$ [193].

defects will not be discussed in this section. They indirectly affect the point defect densities by functioning as nucleation centers and getters or sources of impurities, depending on the partial pressure of Cd and the temperature [126]. For CdTe, in addition to Te precipitates, other precipitates have been reported. In heavily In-doped CdTe ($>10^{17} \text{ cm}^{-3}$), precipitates of In₂Te₃ were detected with an average size of 100–125 Å and a concentration of 10^{14} – 10^{16} cm^{-3} [127,128]. In heavily Cl-doped crystals ($>10^{17} \text{ cm}^{-3}$) precipitates of CdCl₂ were observed with average size of 150 Å and concentration greater than 10^{16} cm^{-3} . For precipitates annealed under high or medium Cd pressures and with In doping, cadmium interstitials are present and precipitation occurs to form Cd–In alloys [128]. One can expect similar behavior for CZT, although the observation of such has not yet been reported.

3.2.2. Methods used to study electronic defects

There are dozens of methods used for defect studies, and let us briefly review here some of the more popular methods used to study CZT and CdTe. For the shallow levels, photoluminescence has been used with a large degree of success to measure the ground state and excited state energies. Electron paramagnetic resonance has been used for both the shallow and the deep levels to infer the electronic states of the impurities, including crystal field splittings and impurity sites.

To study the deep levels, many methods have been used, but the investigations are made difficult by the high resistivity of the material, difficulty with determination of the trap types (whether electron or hole), and difficulty of making metal/semiconductor contacts. Some of the most widely used methods are thermally stimulated conductivity (TSC) and related methods [129,130], thermoelectric emission spectroscopy (TEES) [131], deep level transient spectroscopy (DLTS) [132], photo-DLTS [133], photoinduced current transient spectroscopy (PICTS) [134], and temperature-dependent Hall-effect (TDH) [264].

However, for n-type SI CdTe and CZT, their high resistivities are on the order of $10^9 \Omega \text{ cm}$ and their typical RT electron mobility is about $1000 \text{ cm}^2/\text{V s}$, implying free carrier concentrations on the order of $6 \times 10^6 \text{ cm}^{-3}$. Methods such as DLTS and TDH cannot be used for these resistivities since these methods require the free carrier concentration to exceed the impurity concentration. To

circumvent this problem, photo-DLTS was developed, and it allows study of deep levels when combined with optical spectroscopy [133]. PICTS has also been used to study defects in CZT [135–137].

In addition to the difficulties posed by high resistivity, the trap types are difficult to establish. TSC is a well-established method for studying SI materials, however, it is difficult to infer the trap type from TSC because both electron and hole traps give signals having the same polarity. By using Schottky contacts and biasing, one can try to measure only majority carrier traps, but defects due to the contact electrodes compete with the bulk defects of interest [138,139]. Furthermore, the Schottky contact resistance increases exponentially with decreasing temperature, which can severely distort the TSC spectra. The same considerations apply to DLTS and other methods. TSC has been used to study CdTe and CZT materials [13,140–144].

TEES can determine the trap types, but the TEES signal has been interpreted in the same manner as TSC by assuming that the sign of the TEES current directly gives the trap type [131]. TEES has been applied to high pressure Bridgman CZT by several groups [137,141–147]. TEES has also been applied to other CZT materials grown and processed using novel methods [5]. There is evidence now that the simple interpretation of TEES is not correct [143].

Thermoelectric voltage spectroscopy (TEVS) is a new method for determining the trap types and for studying compensation [144]. It was shown that TEVS, TEES, and TSC are related by a simple product rule and that the TEVS signal is a more fundamental quantity directly reflecting the compensation process.

In addition to measuring the trap properties, there has been considerable interest in the elemental analysis of the materials in order to correlate the electronic properties to impurities or dopants. In most such studies, intentional doping is done in the range from 10^{15} to 10^{18} cm⁻³. The elemental analysis of dopants and also of unintentional impurities is often done by glow discharge mass spectroscopy (GDMS), which has detection limits of a few parts per billion atoms for Ni, Na, and Li in good quality CZT [54]. The worst detection limit appears to be 50 ppb for Cu, since Cu and Zn are chemically very similar. It is useful to note these quantities in terms of atomic densities in order to be able to compare them to carrier and dopant concentrations. The density of CdTe is 6.2 g/cm³ and its formula weight is 240.00 g, implying 1 ppm atoms equals 3.11×10^{16} atoms/cm³. The density of ZnTe is 6.34 g/cm³ and its formula weight is 192.97 g, implying 1 ppm atoms equaling 3.96×10^{16} atoms/cm³. Interpolating, for CZT with Zn $x = 0.1$, 1 ppm is 3.19×10^{16} atoms/cm³.

3.2.3. Defects by groups I, III, IV, V, and VII elements

The point defects in CZT caused by many impurities are shallow levels. Since CZT is a II–VI element, all groups I, III, IV, V, and VII elements are expected to function as dopants. Considerable data exist on their defect energies and these will be reviewed here. Transition metal elements tend to give deeper levels, and they will be treated later, as will be the native point defects.

The ionization energies of groups I, III, IV, V, and VII elements are summarized in Table 4. Substitutional group V elements on anion (Te) sites are acceptor states. Group III elements on the cation sites and VII elements on the anion sites are donor states.

Group I elements are amphoteric in II–VI compounds; on cation substitutional sites, they act as acceptors, but, on interstitial sites, they act as donors [148]. For example, Li is an acceptor at Zn or Cd sites with a ground state energy of 58 meV but it is a donor at interstitial sites with a ground state energy of 14 meV [149]. Furthermore, the energy of formation of Li interstitials is low due to the small size of the Li atoms, for example, in ZnSe [148]. In addition, Li_{Cd} is easy to form due to the typical large concentrations of V_{Cd} in CZT. This has practical consequence that no reports of successful compensation using Li has been reported for CZT or CdTe, although, for Si and Ge, the

Table 4
Ionization energies of groups I, III, IV, V, and VII elements

Element	Photoionization, <i>E</i> (meV)	Thermal ionization, <i>E</i> (meV)	Method	Reference
Li	Acceptor: 58.0		PL	[149]
Na	Acceptor: 58.7		PL	[149]
N	Acceptor: 56.0		PL	[236]
P	Acceptor: 68.2		PL	[236]
As	Acceptor: 92.0		PL	[236]
Cl	Donor: 14			[170]
Cl	Donor: 14.48		PL	[237]
Cl–V _{Cd}	Acceptor: 120		PL, ODMR	[168]
Cl DX1		Donor: 220	Theory	[156]
Cl DX2		Donor: 470	Theory	[156]
Cl DX3		Donor: 210	Theory	[156]
Al	Donor: 14.05		PL	[237]
F	Donor: 13.71		PL	[237]
Ga	Donor: 13.83		PL	[237]
In	Donor: 14.08		PL	[237]
In DX		Donor: 300	Theory for Cd _{0.8} Zn _{0.2} Te	[156]
Ge	Donor: 950	Acceptor: 730	Photo-EPR	[238]
Sn	Donor: 850		Photo-EPR	[238]
Sn	Donor: 900		DLTS	Kremer et al. (1988)
Sn	Donor: 890, 430		QTS	[239]
Pb	Donor: 1280		Photo-EPR	[238]

ion-drift technique using Li are routinely used to produce semi-insulating regions by compensation of the acceptor impurities by interstitial Li ions [150,151].

Group IV elements appear to introduce both shallow and deep levels. Doping of THM grown CdTe by Si and C was done, but showed little electrical activity [140]. Pb and Ge doping EPR studies of CdTe have been reported [152]. P, Cs, and Sn doping of CdTe and observation of many shallow and deep levels, for each dopant, as characterized by DLTS, PITS and PC, has been reported [265]. Reported values of the ionization energies due to group IV elements are shown in Table 4.

We note that little work has been reported relative to the behavior of In on the transport properties of CZT. In CdTe, ρ increased to $>10^8 \Omega \text{ cm}$ upon In doping. Increases were confined to the narrow concentration range of $(3-6) \times 10^{15} \text{ In atoms/cm}^3$ [153], where a transition region between p- and n-type was indicated.

3.2.4. DX-centers and A-centers

The structure of CdTe has the international symbol for space group, $F\bar{4}3m$. This space group belongs to the invariant unitary subgroup T_d , which is the full tetrahedral group containing all the covering operations of a regular tetrahedron, including reflections. When there is interaction between a native defect and an impurity or between the lattice and an impurity, lattice relaxation occurs locally to minimize the energy. An impurity in a lattice that causes significant lattice relaxation and accompanying deepening of its energy level is called the DX-center, well-known examples being Se, Te, Si, and Sn in AlGaAs [154,155]. There is mounting evidence that DX-centers also exist in CdTe and CZT. A donor–vacancy complex is called an A-center, and it has been extensively studied in research involving compensation, especially for In and Cl.

The DX-centers in CZT have C_{3v} symmetry because they involve lattice relaxation along the $\langle 111 \rangle$ bond directions for the impurity and the surrounding atoms. From group theoretical considerations, with reduction in symmetry from T_d to C_{3v} , triply degenerate states T_1 and T_2 are

lifted in degeneracy to form a doubly degenerate state and a single state. In addition, local lattice relaxation occurs to deepen the impurity level.

Based on a first-principles calculation of CZT, for column III donors, one DX atomic configuration is found to be energetically favorable, and, for column VII donors, three atomic configurations are found to be possible [156]. The calculation also showed that, in CdTe, Ga forms a DX-center but Al and In do not. However, as the Zn concentration is increased in CZT, Al and In are predicted to become DX-centers. In addition, for CdTe, Cl, Br, and I are not DX-centers, but alloying with Zn is predicted to make 2 DX-centers for Cl and 1 DX-center each for Br and I. The calculated ionization energies of the DX-centers are given in Table 4.

There is some experimental evidence for the calculations. For In-doped CZT, there is an agreement between the predicted value of 0.29 eV and the experimentally observed value of 0.29 eV for the electron ionization energy of the In DX-center [255,157]. In addition, other properties characteristic of DX-centers were also found for In-doped CZT, including persistent photoconductivity, large Stokes shift for photoionization relative to the thermal ionization energy measured by DLTS (from 0.7 to 0.29 eV).

Persistent photoconductivity was also seen for Cl-doped samples, but the low free carrier concentration made the DLTS measurement difficult [157]. Persistent photoconductivity is characteristic of deep levels, including DX-centers. For Cl-doped CZT grown by the Bridgman method, persistent photoconductivity was observed and the thermal activation energy of the defect responsible for it was measured to be -4.5 meV for Zn $x = 0$, 35 meV for $x = 0.05$, 91 meV for Zn $x = 0.1$, and 270 meV for Zn $x = 0.25$ samples [158]. However, it is not clear whether there are DX-centers or not.

A supporting evidence for DX-centers in CZT is that the addition of Zn to CdTe has been observed to decrease the free carrier concentration and to cause persistent photoconductivity, despite constant incorporation of dopants into the lattice [266]. In CdTe, even 4% addition of Zn stiffens the lattice by 2%, giving it better structural quality [159,160]. The elastic constants, c_{11} , c_{12} , c_{44} , for CdTe are 5.35, 3.68, 1.99 [161] and for ZnTe are 7.22, 4.09, 3.08 [259], in units of erg/cm^3 . For CZT, Vegard's rule can be applied. The change of the elastic properties of the lattice causes more favorable conditions for the formation of DX-centers in CZT than in CdTe, in agreement with the first-principles calculation of DX-centers in CZT [156]. Furthermore, it was speculated that Zn segregation in CZT may cause a larger Zn alloying effect even for low Zn concentrations [156].

Group III elements are donors at the Cd site, but there is considerable evidence of self-compensation involving vacancy complexes (A-centers), especially for In. For CdTe, In_{Cd} is a shallow donor. At low In concentrations, $[\text{In}]$, in Bridgman grown CdTe under Cd over-pressure, the free carrier concentration $[n]$ increased linearly with $[\text{In}]$, indicating 100% doping efficiency, but at and above $[\text{In}]$ of $2 \times 10^{18} \text{ cm}^{-3}$, $[n]$ became independent of $[\text{In}]$ [162]. Since the solubility limit of In is known to be $1 \times 10^{19} \text{ cm}^{-3}$ or higher, this effect is seen as evidence of self-compensation, possibly due to the creation of an $(\text{In}_{\text{Cd}}^+ \text{V}_{\text{Cd}}^{2-})^-$ complex. The same results were also reported in a molecular beam epitaxial study of In doping of CZT ($x = 0.03\text{--}0.04$) under Cd over-pressure. When dopant concentrations were varied from 2×10^{16} to $3 \times 10^{18} \text{ cm}^{-3}$, as measured by SIMS, In donor activation efficiency of 100% was found between 2×10^{16} and $1 \times 10^{18} \text{ cm}^{-3}$, but strong self-compensation behavior was observed for higher concentrations [163]. Since Cd over-pressure was necessary for the high donor activation efficiency for the low doping concentrations, it was concluded that $\text{V}_{\text{Cd}}^{2-}$ formation is suppressed by Cd over-pressure and enhanced by low Cd partial pressure [163].

A direct evidence of the formation of the complex was given by positron lifetime measurements, which detect neutral or negative defects. A review of its use on II–VI materials can be found elsewhere [164]. For In-doped CdTe samples, it showed Cd vacancy concentrations which increased

with [In], consistent with self-compensation of In by V_{Cd} by the formation of $\text{In}-V_{\text{Cd}}$ complexes [165–167]. In principle, a Cd vacancy can be neutral, singly negative, or doubly negative, depending on the location of the Fermi-level. The positron lifetime measurements showed that the $\text{In}-V_{\text{Cd}}$ complex is either neutral or negatively charged.

Cl has been employed in CdTe to produce high resistivity material [113], and its use has therefore been investigated in CZT as well. Cl on a Te site is a shallow donor with a binding energy of 14 meV. PL showed the chlorine A-center to have a binding energy of 120 meV, and optically detected magnetic-resonance technique verified the A-center to consist of a Cd vacancy and a Cl donor on the nearest Te site [168]. Cl-doped CdTe shows a strong donor bound exciton line (D^0, X) in the PL. From positron lifetime measurements, near proportionality was found between the concentration of A-centers and the concentration of Cl [167]. TSC measurement of Cl-doped material showed a preponderance of electron traps 0.1–0.2 eV deep and hole traps 0.27–0.35 eV deep that may be due to $\text{Cl}-V_{\text{Cd}}$ complexes [267].

Photoluminescence spectra at 4.2 K for three Cl-doped CZT samples are shown in Fig. 30. There are several deep bands in the three spectra, and it is not immediately clear whether they are the same set of bands in each case. The near-band-edge spectra for the $x = 0.2$ and 0.35 samples show that (D^0, X) is the dominant peak, as would be expected for Cl-doped material. The position of the (A^0, X) peak (3 meV below (D^0, X)) is consistent with copper. Notably absent is the additional (A^0, X) band which often occurs approximately 10 meV below (D^0, X). This is attributed to the fact that the doped crystals came from a different supplier than the undoped crystals discussed above, rather than to the presence of chlorine.

Fig. 31 shows electron and hole photo-induced current transient spectroscopy (PICTS) spectra for $\text{Cd}_{0.5}\text{Zn}_{0.5}\text{Te}:\text{Cl}$. The trap levels which can be determined by the traditional Arrhenius-plot technique are labeled in the figures. The hole trap at ~ 0.13 eV is almost certainly due to the A-center, while the bands at 0.3 and 0.5 eV do not correspond to any previously reported results.

3.2.5. Transition metal impurities

It is found that II–VI semiconductors doped with transition metals are especially promising for their photorefractive effect and applications in optoelectronics. For materials used as radiation

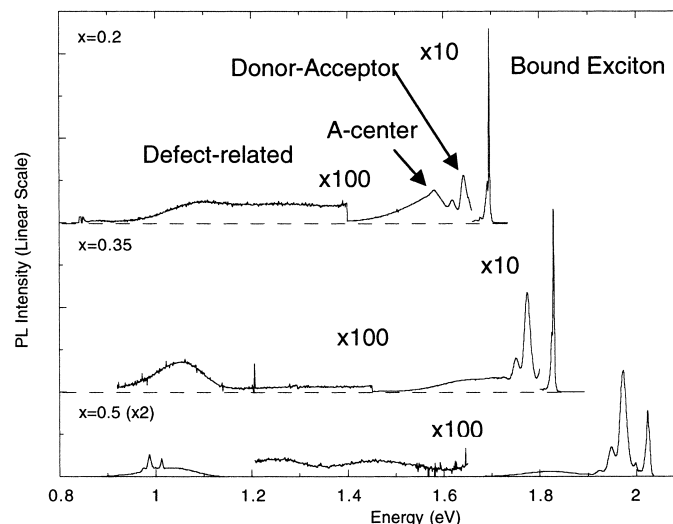


Fig. 30. A 4.2 K PL spectra for Cl-doped $\text{Cd}_{1-x}\text{Zn}_x\text{Te}$ of several compositions [136].

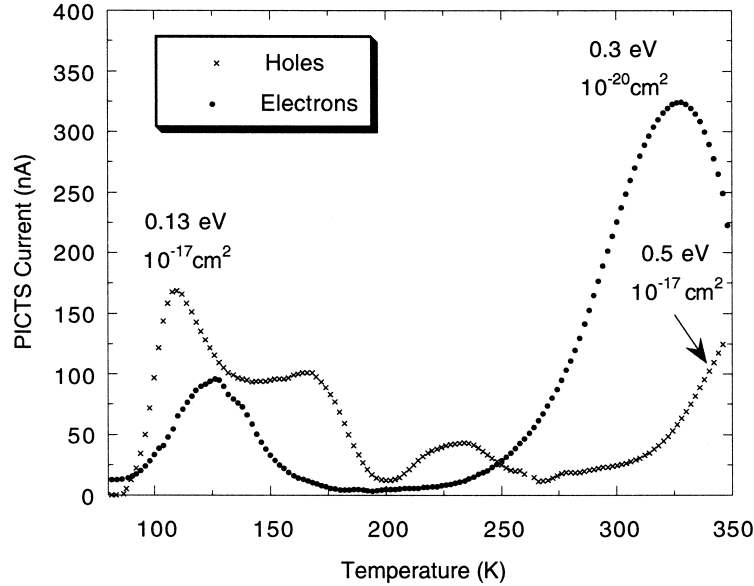


Fig. 31. Hole and electron PICTS spectra for $\text{Cd}_{0.5}\text{Zn}_{0.5}\text{Te:Cl}$ — $t_1 = 8$ ms; $t_2/t_1 = 8$. Indicated in the figure are the trap energy levels and their capture cross-sections [136].

detectors, they appear to be important in making the material semi-insulating. In moderately doped materials, the impurities commonly substitute for metal cations, and they can act as either donors or acceptors. The 3d transition metal elements, having partially filled 3d shells, have received the most attention. A summary of the ionization energies of transition metal impurities is given in Table 5.

The importance these elements for CZT radiation detectors were clearly seen once CdZnTe materials could be made semi-insulating. For example, a recent V doping study showed that doping with V in the range of $(1\text{--}10) \times 10^{18} \text{ cm}^{-3}$ can make CdZnTe semi-insulating with resistivities in the $10^9\text{--}10^{10} \Omega \text{ cm}$ range, for Zn $0 < x < 0.1$ [169]. An earlier study also showed the efficacy of V doping [170], and good CdZnTe radiation detectors were made using V and Fe-doped CdZnTe [121].

3.2.6. Copper-doped CZT

Cu has long been studied for its potential role in compensation and trapping in CdTe and due to the fact that both its diffusivity and solid solubility is high [113]. PL spectra for copper-doped samples exhibit a large range of qualitative behavior, including some cases in which there was pronounced exciton luminescence, and some in which the defect-related luminescence was dominant. An example is shown in Fig. 32. As would be expected, the copper-related acceptor-bound exciton peak is the dominant feature of the near-band-edge spectrum. There is a second pronounced peak at slightly higher energy, and it is unclear at first glance whether this peak is the donor-bound exciton or the free exciton. The energy spacing between the two exciton peaks (≈ 5.7 meV) is more consistent with the $X_1\text{--}(A^0, X)$ spacing, but additional evidence is needed.

In general, additional insight regarding the nature of bands in PL spectra can be obtained by studying how the spectrum evolves with changing temperature or excitation intensity. The weakly bound (D^0, X) is quenched quickly as the temperature is raised, as a larger fraction of excitons acquire enough thermal energy to dissociate from the donor. The less weakly bound (A^0, X) is quenched at a slower rate as the temperature is increased, and the relatively strongly bound free

Table 5
Ionization energies of transition metal elements

Element	Thermal ionization, E (eV)	Photoionization, E (eV)	Method	Reference
Sc		Donor: 0.0105	PL	[240]
Ti	Donor: 0.73	Donor: 0.008	PL, TDH	[240]
Ti		Donor: 0.83	DLTS, photo-DLTS	[257]
V		Donor: 0.67	Photo-EPR	[241]
V	Donor: 0.95		DLTS, photo-DLTS	[258]
V	Acceptor: 0.74		Theory	[242]
V	Acceptor: 0.51		TSC	[121]
Cr		Acceptor: 1.34	EPR, ODMR, PL	[243]
Mn	Donor: 0.05, 0.73		Hall	[244]
Fe		Donor: 1.45	Photo-EPR	[245]
Fe		Acceptor: 0.35	EPR, ODMR, PL	[238]
Fe	Acceptor: 0.43		TSC	[121]
Fe		Acceptor: 0.15	SPS	[246]
Fe		Acceptor: 0.2	CPM	[170]
Co		Acceptor: 1.25	EPR, ODMR, PL	[247]
Ni		Acceptor: 0.92	EPR, ODMR, PL	[238]
Ni		Donor: 0.76	CPM	[170]
Cu		Acceptor: 0.36; unknown: 0.6	PICT	[136]
Cu	Acceptor: 0.146		PL	[248]
Cu		Acceptor: 0.37	PICT	[135]
Ag		Acceptor: 0.1075	PL	[253]
Au		Acceptor: 0.263	PL	[254]

exciton/polariton is even more persistent. Thermal broadening is also observed, which causes the bands to become less well resolved as the temperature is increased, as is a shift of the spectrum to lower energy as the temperature is increased due to reduction of the bandgap. This decrease is due primarily to a rather subtle effect involving reduction in phonon frequencies with increasing

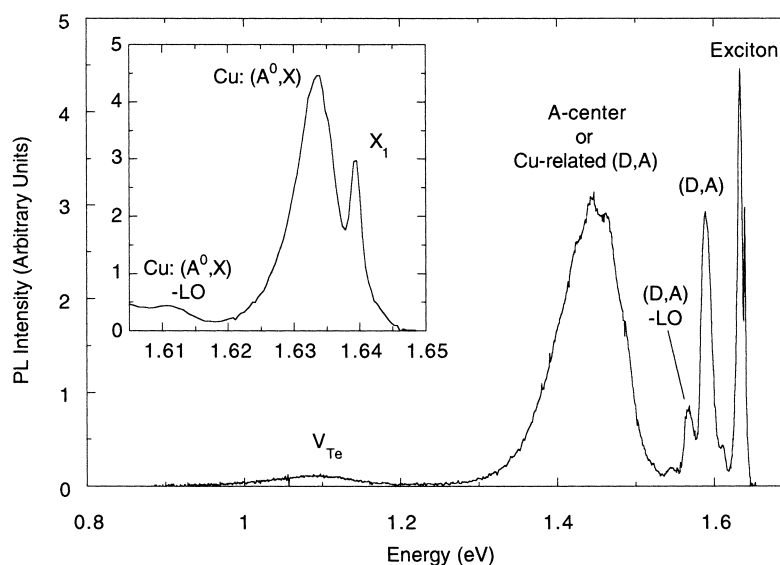


Fig. 32. A 4.2 K photoluminescence spectrum for $\text{Cd}_{1-x}\text{Zn}_x\text{Te}:\text{Cu}$. The near-band-edge region is shown expanded in the inset [136].

occupancy of the conduction band [28], but thermal expansion of the lattice also makes some contribution. The temperature dependence of the bandgap can be fit to the equation [171]:

$$E(T) = E_0 + \frac{\alpha T^2}{\beta + T} \quad (22)$$

but since this equation is completely empirical the extracted parameters are only of value for establishing the bandgap at various temperatures.

The temperature dependence of the spectrum in Fig. 32 provides the needed evidence to determine whether the higher-energy exciton peak is donor bound or free. Since it does not quench rapidly with increasing temperature, it must be the free exciton. This strong free-exciton luminescence and lack of an observable (D^0 , X) band is peculiar to these particular Cu-doped samples.

Perhaps the most noteworthy fact about the spectrum in Fig. 32 is that all the peaks observed in the Cu-doped CZT are routinely seen in spectra of undoped material. This fact is not surprising since Cu is known to be one of the common residual impurities (1–100 ppb concentration) in Bridgman-grown CdTe and $\text{Cd}_{1-x}\text{Zn}_x\text{Te}$. It also means that the acceptor bound exciton peak is the only clear evidence of Cu in the PL spectrum. Given the degree of alloy broadening in this material, it is unlikely that PL can be used as a reliable indicator of the presence of Cu in $\text{Cd}_{1-x}\text{Zn}_x\text{Te}$.

Fig. 33 shows photo-induced current transient spectroscopy (PICTS) spectra with IR excitation for two Cu-doped samples. The band at 0.37 eV for sample 1 has been previously identified as being due to substitutional copper acceptors [135]. The bands in the spectrum for sample 2 are broader and appear to contain multiple components, so that the trap parameters extracted by the two-gate method are unreliable. More sophisticated data analysis techniques based on the fast Tikhonov regularization method [172] are helpful in resolving the bands in cases like this. Fig. 34 shows relaxation time spectra for the two samples in the 200 K region. For sample 1 there is a single dominant level, while for sample 2 there are two clearly resolved levels. Trap parameters for these levels are determined from the Arrhenius plots in Fig. 35. The level at 0.5 eV has been reported as due to interstitial

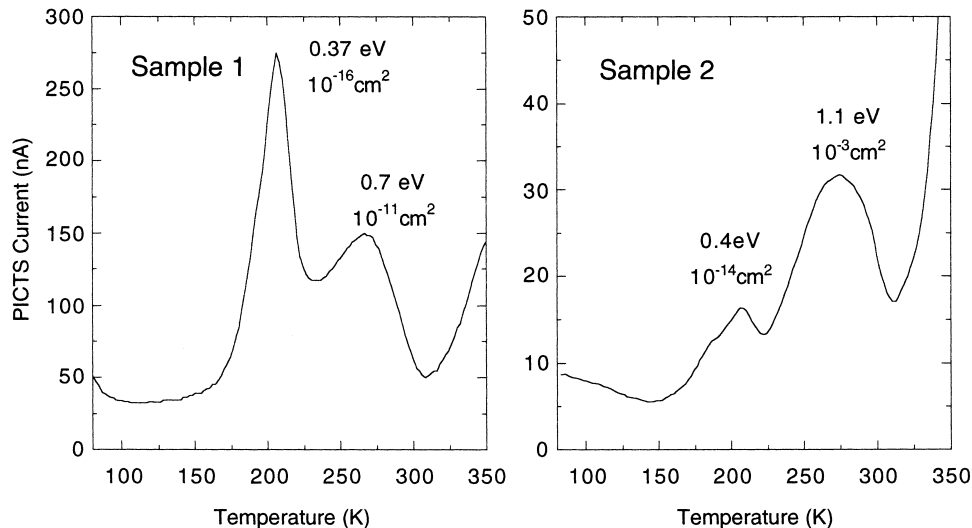


Fig. 33. PICTS spectrum for $\text{Cd}_{0.9}\text{Zn}_{0.1}\text{Te}:\text{Cu}$ — $t_1 = 8 \text{ ms}$; $t_2/t_1 = 8$. Because of the extreme breadth of the bands in the spectrum on the right, the extracted parameters are unreliable (Toney et al., 1998d).

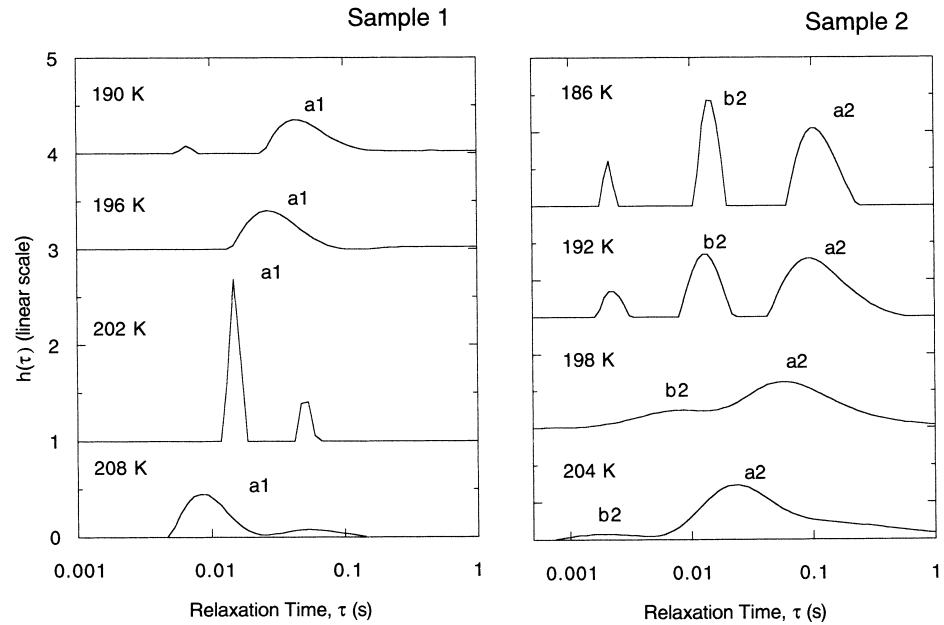


Fig. 34. Relaxation time spectra for the PICTS data of Fig. 33 (Toney et al., 1998d).

cadmium [135]. If the same analysis is performed on the 250–300 K band of sample 2, two levels are found: one with an activation energy of 0.76 eV and a cross-section of 10^{-11} cm^2 and the other with $\Delta E = 0.24 \text{ eV}$ and $\sigma = 10^{-19} \text{ cm}^2$. The latter does not match any previously reported result.

The role of Cu in the electrical behavior of CZT is not well understood. As previously noted, substitutional copper has been associated with a level at near 0.37 eV [135,136]. Evidence points to copper being an acceptor although not necessarily the most dominant hole trap at the concentrations found in most detectors. We note that in CdTe, copper doping has produced substantial

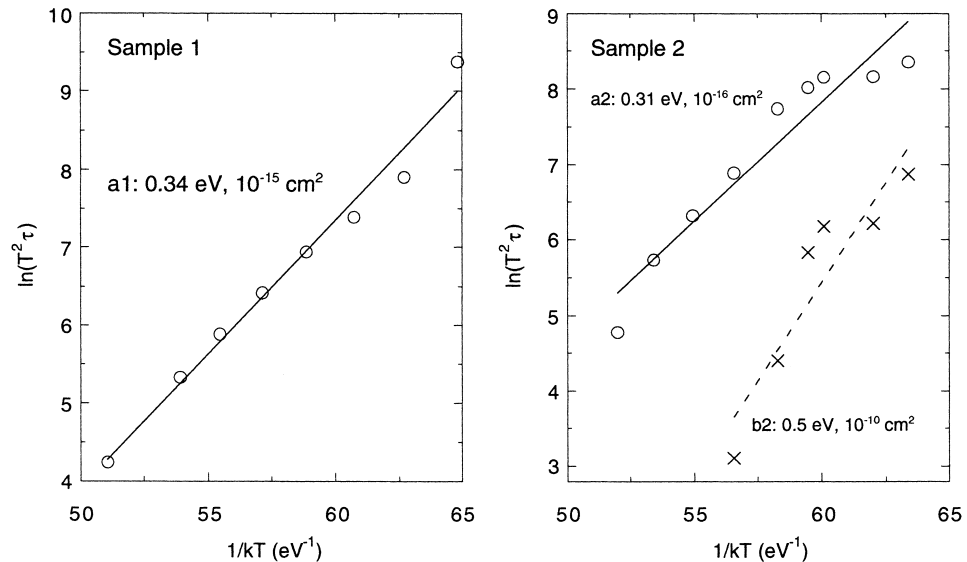


Fig. 35. Arrhenius plots for determining trap parameters from the relaxation time spectra of Fig. 35 (Toney et al., 1998d).

Table 6
Ionization energies of native defects

Defect	Thermal ionization, E (eV)	Photoionization, E (eV)	Method	Reference
V_{Cd}	Acceptor: <0.47	Acceptor: 0.78	Photo-EPR	[170]
V_{Cd}			PICTS	[113]
V_{Cd}	Acceptor: 0.2, 0.8		Theory	[175]
V_{Cd}	Acceptor: 0.1, 0.4, 0.76		DLTS, PICT	[223]
V_{Cd}	Acceptor: 0.1		Theory	[179]
V_{Cd}	Acceptor: 0.43	Donor: 1.4	TEES	[147]
V_{Cd}	Acceptor: 0.21; Donor: 0.73		TEES	[145]
Te_{Cd}	Donor: 0, 0.4		Theory	[175]
Te_I	Donor		Theory	[175]
$Te_{Cd}-V_{Cd}$	Neutral		Theory	[175]
V_{Te}			Photo-EPR	[166]
V_{Te}	Donor: 1.1		DLTS, PICT	[223]
V_{Te}	Donor: 0.4, 0.5		Theory	[175]
Cd_I	Donor: 0.64		DLTS, PICT	[223]
Cd_I	Donor: 0.54		PICT	[135]
Cd_I	Donor: 0.5		Theory	[179]
Cd_I	Donor: 0, 0.2		Theory	[175]

improvements in ρ , but it reduced the carrier lifetimes [113]. Clearly, copper doping is leading to a deep state that is effective at trapping of charge and pins the Fermi-level closer to the mid bandgap position.

3.2.7. Native defects

The native defects in CZT can be donors or acceptors. Both experimental results and theoretical predictions exist, and a summary of their ionization energies is given in Table 6. Experimentally, from EPR and photo-EPR, both the isolated Cd and Te vacancies were identified in CdTe [164,173]. The Cd and Te vacancy concentrations in CdTe were found to be less than $1 \times 10^{16} \text{ cm}^{-3}$. The V_{Cd}^{2-} position was found to be less than 0.47 eV above the valence band, the uncertainty being due to lattice relaxation energy.

Positron lifetime spectroscopy was used to measure the neutral and negative vacancy concentrations in: (1) CdTe and CZT grown by vertical Bridgmann technique; (2) CZT grown by traveling heater method growth technique, and (3) CZT grown by high pressure Bridgman technique [174]. In CdTe, mostly neutral V_{Cd} complexes were found in the high 10^{16} cm^{-3} range. For all Zn $x = 0.04$ and $x = 0.10$ CZT samples, the vacancy concentrations were less, suggesting that divancies formed.

An equilibrium ab initio defect study found that, under Te rich conditions, CdTe at high temperatures is highly compensated p-type with V_{Cd} as the dominant acceptor and Te_{Cd} as the compensating donor [175]. It is assumed that the native defect concentrations at high temperature is frozen in by quenching to low temperature. The assumption of Te-rich condition appears to apply to many recent experimental studies, the only possible exception being materials grown in the former Soviet Union [176]. Under Cd rich conditions, Cd_I is expected to dominate and make the material n-type. One should note, however, that it has been argued that significant point defect reactions occur during the cooling phase [177] and that mutual solid solubilities of Cd and Te are not experimentally established yet [178]. Another first-principles calculation found defect energies of V_{Cd} and Cd_I in rough agreement with experiment [179].

A new type of native defect called “double broken bond” has been suggested as a satisfactory explanation for persistent photoconductivity, optical threshold for it, and for the observation of a deep donor level in the PL measurements of p-doped ZnSe samples [180]. This has not yet been observed in CZT yet.

3.2.8. Photoluminescence of cadmium vacancies

As discussed above a great deal of information can be obtained from the low-temperature photoluminescence spectra of CZT. Peak positions and peak separations yield some information as was used, for example, to determine composition variation. In the 4.2 K PL spectrum for $\text{Cd}_{1-x}\text{Zn}_x\text{Te}$ shown in Fig. 19, a broad band centered at about 1.65 eV is observed which contains several components that are not well-resolved. One group has postulated that this band is luminescent as an acceptor-bound center in which the acceptor is a Cd vacancy [98], but more evidence is needed. Annealing measurements conducted over a range of Cd and Te over-pressures should be helpful in testing this model.

3.2.9. Impurity segregation

The segregation coefficient is commonly used to predict the variation in the concentration of each dopant as function of location along the growth direction. Values for the segregation coefficient are usually determined by mass spectrometry, although occasionally radiotracer profiles have been used. For CZT grown by the high-pressure Bridgman method, most of the impurities in CZT have segregation coefficients that are less than one (e.g. Li, Na, Ca, Cr, Fe, Mn, Ni, Ag, In, Sn, Sb, Tl, Bi, P, Ti, V, Si, Pb, Cu, and Ga), which leads to an accumulation of the impurities in the last-to-freeze section of the ingot [8]. Some impurities have values close to or exceeding one (e.g. Zn, Se, and S). Fig. 36 shows the variation in iron along the growth direction at four different locations for a $\text{Cd}_{0.9}\text{Zn}_{0.1}\text{Te}$ ingot grown by the high-pressure Bridgman method. Using Phann's law a segregation coefficient of 0.22 produces the best fit to the data [8].

Zanio [181] published segregation coefficient values for several other impurities in CdTe. Review of the literature (see, for example, Astles [182] and the references therein) reveals significant variations in the reported values for the segregation coefficients. This wide variability might be due to errors in the impurity analyses, minimum detection limits for GDMS and ICP techniques,

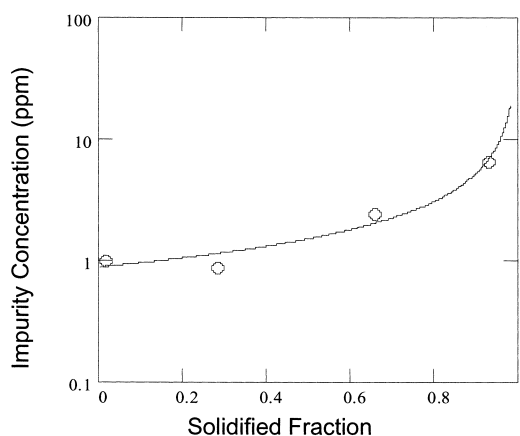


Fig. 36. Variation in the concentration of iron along the growth direction at four different locations for a $\text{Cd}_{0.9}\text{Zn}_{0.1}\text{Te}$ ingot grown by high pressure Bridgman. Using Phann's law a segregation coefficient of 0.22 produces the best fit to the data [8].

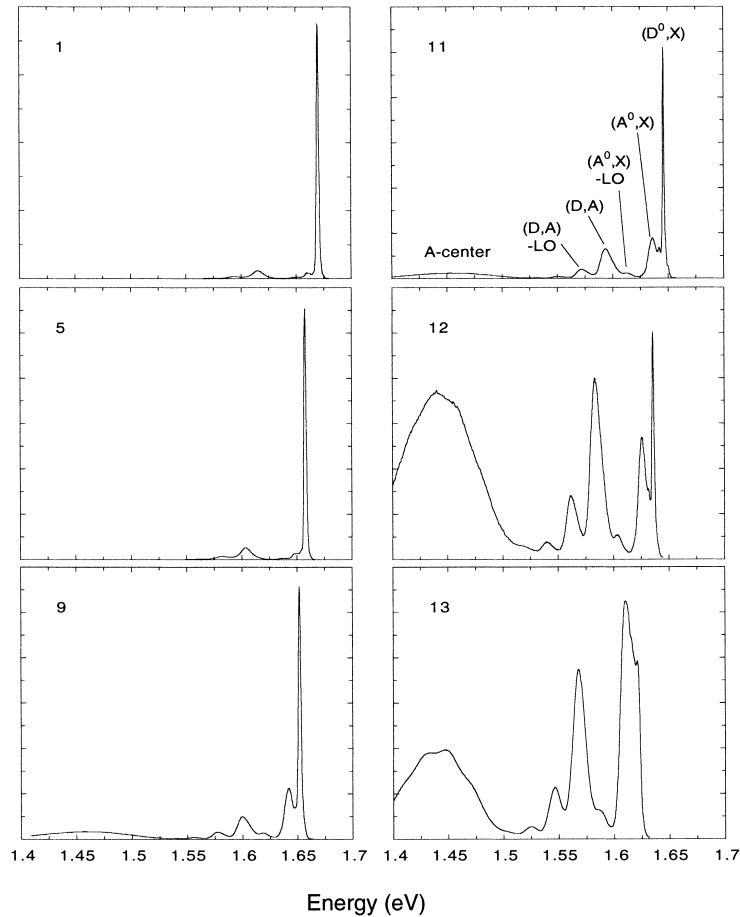


Fig. 37. Qualitative change in photoluminescence spectrum along the growth axis showing decreasing crystal quality as one approaches the heel [193].

diffusion of impurities in the solid phase during cool down, contamination during the growth process, variations in the Zn content within the CZT ingot, or the presence of inclusions containing a significant fraction of the impurity as a second phase. Values for the segregation coefficients have also been reported by Hermon et al. [79].

The consequence of this segregation of impurities is that the crystal quality is often degraded in the portion near the heel. Fig. 37 shows representative PL spectra at various positions along the boule axis. The number in the upper left corner of each plot corresponds approximately to the distance from the tip in cm. One factor that contributes to broadening of the peaks is composition variation. However, it is also clear that from the tip to the middle of the boule (1 and 5), the spectrum is completely dominated by the donor-bound exciton while closer to the heel (9 and 11) the (A^0, X) , (D, A) and A-center luminescence is more significant. At the very heel (12 and 13), the donor-acceptor and defect-related luminescence dominate, and the integrated intensity of (A^0, X) outweighs (D^0, X) , which signifies a growth of the shallow acceptors compared to the shallow donors as one approaches the heel of the ingot. This picture of decreasing crystal quality along the growth axis is true in general, but there can also be significant variations in quality on a millimeter-scale. Fig. 38 shows spectra from several points within a 1 cm^2 sample from the last to freeze end of

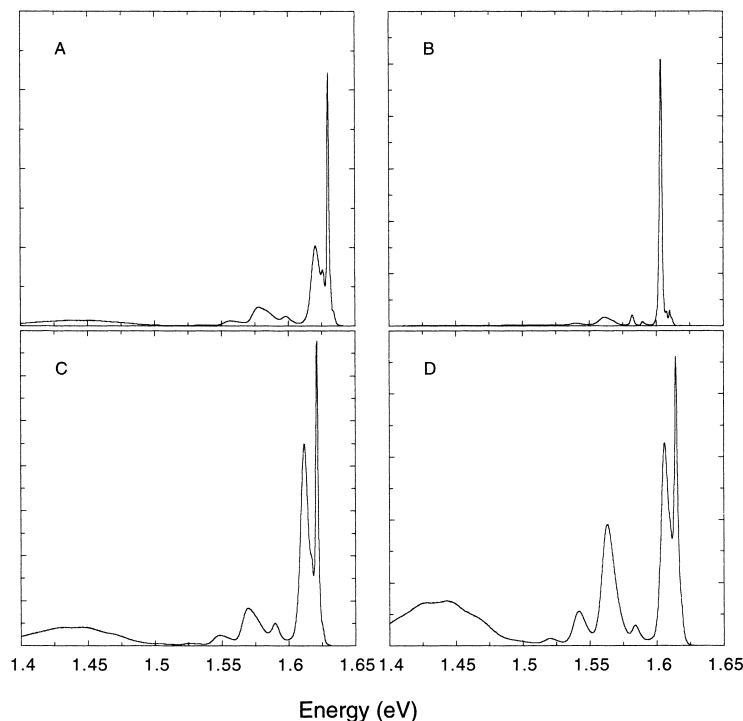


Fig. 38. Qualitative change in photoluminescence spectrum on a millimeter scale within a 1 cm^2 sample at the heel end of a boule. (A), (C), and (D) are qualitatively similar but (B) is more CdTe-like [193].

the boule. Comparison shows that there is substantial variation in the character of the spectrum on a millimeter scale. There is tremendous variation in crystal quality among the four points, all within a few millimeters of each other. The zinc content as evidenced by the bandgap also varies greatly.

One of the most remarkable features of Fig. 38 is the contrast between point B and the other points. At point B the spectrum is dominated by an acceptor-bound exciton, indicating a larger proportion of shallow acceptor states. Despite being at the very heel and surrounded by poor-quality material, this point has a spectrum that shows good crystallinity, exhibiting excited-state free exciton luminescence and good resolution between peaks.

3.3. Transport properties

We now discuss the effect of electron and hole transport properties on detector performance. Transport is characterized by two parameters for each carrier type: mobility, μ , and mean trapping lifetime, τ . The quantity which is directly related to detector performance is the product $\mu\tau E$, where E is the electric field. This quantity is the mean drift length, sometimes called the *schubweg*. Despite the underlying complexity of trapping phenomena, simple macroscopic models based on the use of the mean drift length predict detector behavior remarkably well. Details of the relationship between carrier transport and detector performance can be found in the literature [57].

3.3.1. Carrier mobility

One of the great strengths of CdTe compared to other high-Z materials is its relatively high electron mobility ($\sim 1100 \text{ cm}^2/\text{V s}$ at 300 K). The hole mobility, on the other hand, is about a factor

of 10 lower. It is typically found that the electron mobility of $\text{Cd}_{1-x}\text{Zn}_x\text{Te}$ is comparable to that of CdTe , while the hole mobility is somewhat lower than in CdTe .

Ideally carrier mobilities can be calculated from the scattering rates for acoustic phonon, polar optical phonon, piezoelectric, impurity and alloy scattering, with polar optical scattering being dominant for non-alloyed II–VI and III–V materials at room temperature [28,31]. Suzuki et al. [256] found that for $\text{Cd}_{0.8}\text{Zn}_{0.2}\text{Te}:\text{Cl}$ the hole mobility was limited by trapping–detrapping involving the A-center complex $(\text{V}_{\text{Cd}}\text{Cl}_{\text{Te}})^{-}$.

The dependence of the carrier mobilities on alloy composition is an important issue for future development of higher- x variants of $\text{Cd}_{1-x}\text{Zn}_x\text{Te}$. Two factors are relevant to this question: first, the alloy scattering rate varies as $x(1-x)$ and therefore is greatest in the middle of the composition range; second, all scattering rates increase with the effective mass of the carrier, which in turn increases with bandgap [29]. One can, in principle, obtain an estimate of the effective mass from the PL spectrum. Having determined the free exciton binding energy previously, one can determine the Bohr radius of the exciton. The dielectric constant is assumed to be a linear interpolation between CdTe ($\epsilon = 10.9$) and ZnTe ($\epsilon = 9.7$) [26] and using a zinc fraction of 0.13, as determined from the PL spectrum, a Bohr radius of 62.6 Å is predicted. From this one can obtain an exciton reduced mass of $0.090m_0$, which implies a hole effective mass of $0.40m_0$, which is a little below the conductivity effective mass ($0.47m_0$ for ZnTe , $0.53m_0$ for CdTe).

Toney et al. [96] have calculated the electron mobility as a function of x by iterative solution of the Boltzmann transport equation, following Rode [184] and Chattopadhyay [185]. Assuming an isotropic (in k -space) conduction band, this involves solving for the perturbation function, $f(E)$, from the equation:

$$[S_0(E) + \tau_{\text{ac}}^{-1}(E) + \tau_{\text{pz}}^{-1}(E) + \tau_{\text{al}}^{-1}(E)]\phi(E) = 1 + S_+(E)\phi(E + kT_0) + S_-(E)\phi(E - kT_0) \quad (23)$$

where $S_0(E)$ is the scattering-out rate due to LO phonon scattering, and τ_{ac} , τ_{pz} and τ_{al} are the mean scattering lifetimes for acoustic phonon, piezoelectric and alloy scattering, respectively. $S_{\pm}(E)$ is the scattering-in rate by emission/absorption of a LO phonon, and kT_0 is the LO phonon energy at the zone center. Here, T_0 is sometimes referred to as the Debye temperature, but for optical phonons it is more properly called the Einstein temperature. Expressions for all of the scattering rates are given in [185]. In this calculation the two-mode phonon structure of $\text{Cd}_{1-x}\text{Zn}_x\text{Te}$ is accounted for by using two terms, weighted by the alloy composition. The composition dependence of each mode frequency was taken as a linear interpolation between the end points calculated by Talwar et al. [186].

Eq. (23) is solved by iteration, with the $f(E \pm kT)$ terms on the right hand side being set to zero in the first pass. After each iteration the mobility is calculated as

$$\mu = \frac{e}{m^*} \frac{\int_0^\infty E^{3/2} (\partial f_0 / \partial E) \phi(E) dE}{\int_0^\infty E^{3/2} (\partial f_0 / \partial E) dE} \quad (24)$$

where f_0 is the equilibrium Maxwell–Boltzmann distribution function.

Fig. 39 shows calculated electron mobilities for CdTe and ZnTe as a function of temperature, using the material parameters given by Rode [187]. Many authors adjust the parameters to fit the data, but we feel that this procedure is unjustified given that the Boltzmann equation itself is only a first-order perturbation method. In any event, one is generally concerned with the trend of μ versus x rather than the precise value of μ .

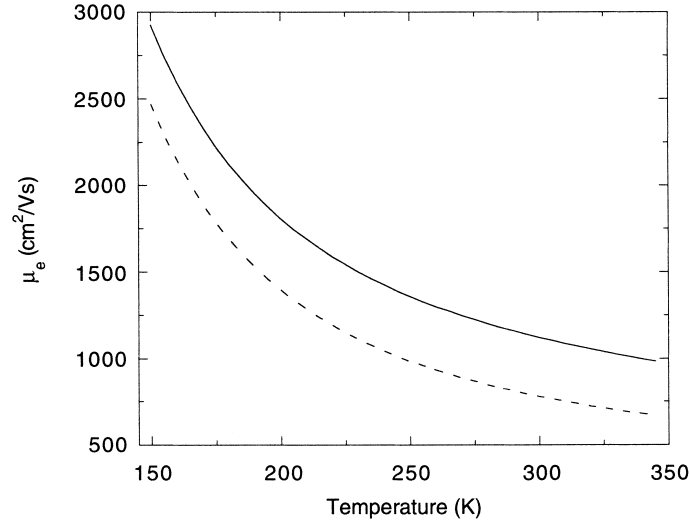


Fig. 39. Calculated electron mobilities for CdTe (solid) and ZnTe (dashed) as a function of temperature [96].

For studying the composition dependence of the mobility in $\text{Cd}_{1-x}\text{Zn}_x\text{Te}$, one is particularly interested in the alloy scattering rate, which is

$$\tau_{\text{al}}^{-1} \propto x(1-x)(m^*)^{3/2} |\Delta U|^2 a^3 E^{1/2} \quad (25)$$

where ΔU is the alloy scattering potential, a quantity that is always determined by fitting of experimental results. In the case of $\text{Cd}_{1-x}\text{Zn}_x\text{Te}$ there are conflicting results: Chattopadhyay [185], using the data of Burshtein et al. [188], reports $\Delta U_e = 0.3$ eV, while Suzuki et al. [183] report $\Delta U_e = 0.7$ eV, $\Delta U_h = 0.1$ eV. The latter result is more intuitively pleasing, since ΔU is often identified with the band offset between the constituents, and we expect the conduction band offset to be much greater than the valence band offset for CdTe/ZnTe, based on the common-anion rule [31]. Which choice is correct is not clear though the choice of 0.7 and 0.1 for the alloy scattering of electrons and holes seems more plausible since direct measurements of the valence band offset between CdTe and ZnTe have shown that it is no more than 15% of the bandgap difference [189,190]. On the other hand Szeles et al. [146] have argued that the composition dependence of hole trap ionization energies implies that either the inert atomic-like character of localized levels or the small valence band offset is invalid. This may be a moot point since Singh [31] has pointed out that the alloy scattering potential is a fairly ill-defined quantity. It is not clear theoretically whether it corresponds to the difference in electron affinities, the difference in bandgaps, the band offsets, or some other quantity. Furthermore, clustering effects also affect the alloy scattering rate. Hence, alloy scattering potentials are determined by fitting of experimental data, and it is therefore ultimately not well defined to ask which is the “correct” value. Given two radically different experimental results and no clear basis for choosing between them, the best course of action would be to allow for the possibility that either set of values or some value intermediate between them may be correct.

The lattice constant, a , and effective mass, m^* are taken as a linear interpolation between CdTe and ZnTe. Fig. 40 shows the calculated electron mobility of $\text{Cd}_{1-x}\text{Zn}_x\text{Te}$ at $T = 300$ K as a function of x , using both Chattopadhyay’s and Suzuki et al.’s values of ΔU_e . A linear interpolation between

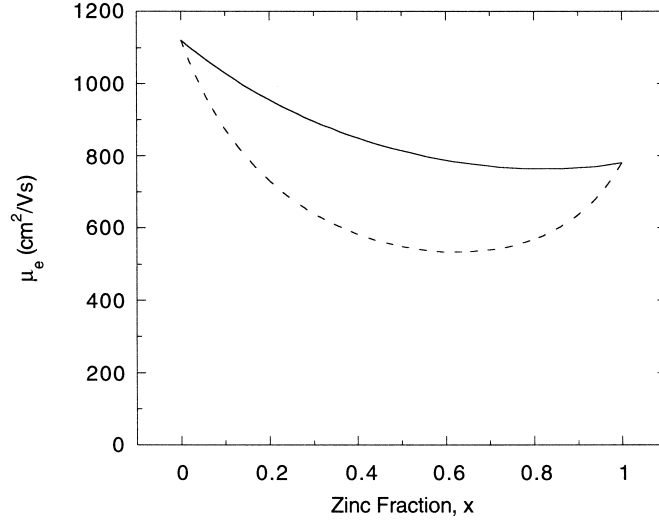


Fig. 40. Calculated electron mobility of $\text{Cd}_{1-x}\text{Zn}_x\text{Te}$ at $T = 300$ K as a function of x using $\Delta U_e = 0.3$ eV (solid) and $\Delta U_e = 0.7$ eV (dashed). Here ΔU_e is the alloy scattering potential for electrons [96].

CdTe and ZnTe was used for all parameters, and the parameters of the constituents were taken from [187].

Accurate calculation of hole mobility is much more difficult than for electrons, because of the more complex valence band structure. First, valence band wave functions have p-like symmetry rather than s-like, which makes the matrix elements that appears in the scattering probability more difficult to evaluate. Second, scattering between the heavy-hole and light-hole bands must be taken into account. These issues have been dealt with in the literature [30,191], but not in a way which makes the calculations easily adaptable to the alloy. We, therefore, choose to implement a greatly simplified calculation in which we use the s-like scattering rates and ignore interband scattering. After Wiley [192] the mobilities are calculated separately for light-hole and heavy-hole bands, and the overall mobility is then estimated as:

$$\mu = \frac{\mu_{hh} + \mu_{lh}(n_{hh}/n_{lh})}{1 + (n_{hh}/n_{lh})} \quad (26)$$

where n_{hh}/n_{lh} is the ratio of occupancies of the two bands, which is approximately equal to

$$\frac{n_{hh}}{n_{lh}} = \left(\frac{m_{hh}^*}{m_{lh}^*} \right)^{3/2} \quad (27)$$

The approximate hole mobility as a function of alloy composition is shown in Fig. 41 for $\Delta U_h = 0.1$ and 0.3 eV.

3.3.2. Experimental determination of mobility

A commonly used method to study the transport properties in detectors is based on their response to α -particles. This method requires a specialized apparatus that allows the radiation source to be in close proximity to the detector, since α -particles will not penetrate more than a few microns through solid matter and will scatter inelastically even from air.

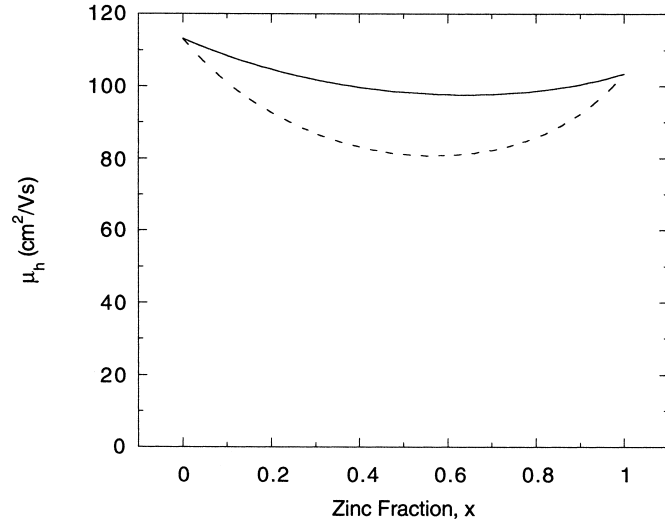


Fig. 41. Estimated hole mobility of $\text{Cd}_{1-x}\text{Zn}_x\text{Te}$ at $T = 300$ K as a function of x using $\Delta U_h = 0.1$ eV (solid) and $\Delta U_h = 0.3$ eV (dashed). Here ΔU_h is the alloy scattering potential for holes [96].

Because the penetration depth of α -particles is only a few microns, the single-particle Hecht relation can be written as [193]:

$$Q(V) = \frac{qVN_0(\mu\tau)_e}{d^2} \left[1 - \exp\left(-\frac{d^2}{(\mu\tau)_e V}\right) \right] \quad (28)$$

where N_0 is the number of charge carriers created by the incident radiation, Q the total charge collected, d the distance between the anode and cathode, q the electronic charge, and V is the applied bias. By measuring the charge collection with a long shaping time as a function of bias and fitting the data to the above equation, one can extract the $\mu\tau$ product for electrons. By reversing the bias, the same can be done for holes, provided that the hole transport is good enough to generate a measurable signal. Representative Q versus V data and curve fits for both electrons and holes for a spectrometer grade detector are shown in Fig. 42.

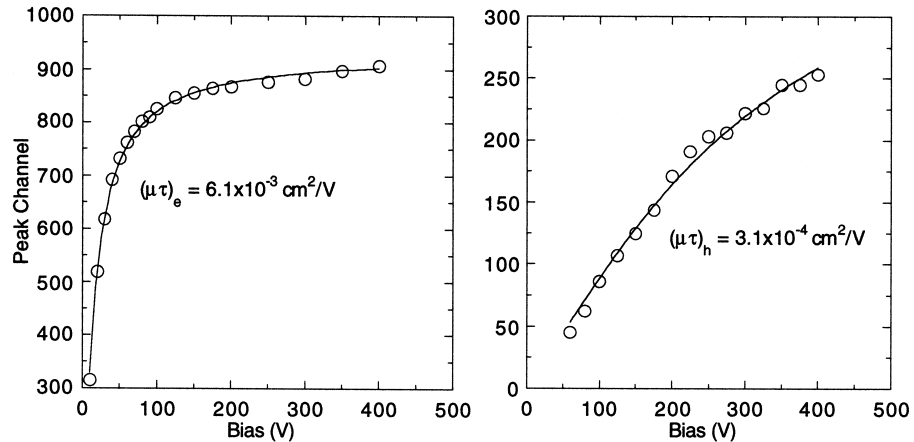


Fig. 42. Determination of electron (left) and hole (right) mobility-lifetime products from the bias dependence of α -particle response [230].

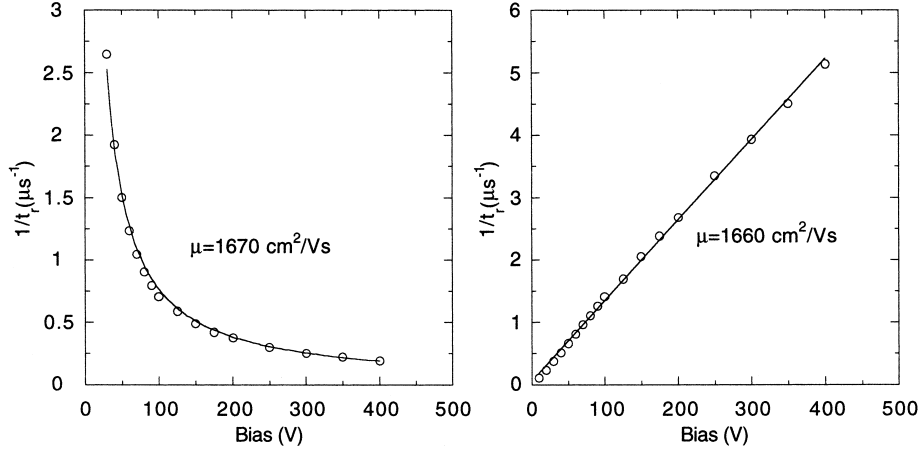


Fig. 43. Determination of electron mobility from bias dependence of the α -particle response rise time (left) or its reciprocal. In the former case the lifetime is held fixed to avoid unphysical results but the results for μ are relatively insensitive to the value of τ [193].

An alternative measure of transport properties using α -particle response is the pulse rise time. From the time-dependent form of the Hecht relation, one can derive the 10–90% rise time as

$$t_r = \tau \ln \left[\frac{0.9 + 0.1 \exp(-d^2/\mu\tau V)}{0.1 + 0.9 \exp(-d^2/\mu\tau V)} \right] \quad (29)$$

The bias dependence of the rise time can also be used to extract the $\mu\tau$ product, as in Fig. 43 (left), but it is more difficult to obtain a good curve fit with this equation. In particular standard algorithms tend to converge to unphysical values for τ . If τ is held fixed at a realistic value, a reasonable estimate for μ can be obtained. On the other hand, if the transit time is less than the carrier lifetime, a plot of $1/t_r$ versus V gives a nearly straight line which yields an estimate of the mobility as shown in Fig. 43. The two methods generally give consistent values for μ . The mobility value extracted from the plots in Fig. 43 seem slightly higher than one would expect — the highest reported value of μ_e for CZT is 1350 cm²/V s [188]. It is possible that the apparent transit time has been reduced by the presence of a dead layer near the contacts, or that the electric field is not uniform in the sample.

Lastly, one can attempt to extract both the mobility and lifetime by fitting the pulse waveform itself to the charge collected as a function of time

$$Q(t) = \frac{q\mu\tau V N_0}{d^2} [1 - e^{-t/\tau}], \quad t \leq t_c \quad (30)$$

but this method is limited by noise; it is not possible to average pulses because of jitter and the bandwidth of typical electronics. The pulse must be captured at relatively low bias for the exponential character to be evident, which reduces the current level. Fig. 44 shows an example of an electron pulse from the same spectrometer grade detector as in Fig. 42, along with a fit to Eq. (30) which yields a value of 0.97 μ s for the electron lifetime. The transit time is determined directly from the width of the pulse as 0.8 μ s, and the mobility is then calculated as 3300 cm²/V s, for a $\mu\tau$ product of 3.3×10^{-3} cm²/V. This mobility value is clearly unrealistically high. Brunett et al. [194] have reported that the apparent lifetime determined by this technique decreases with increasing bias, and

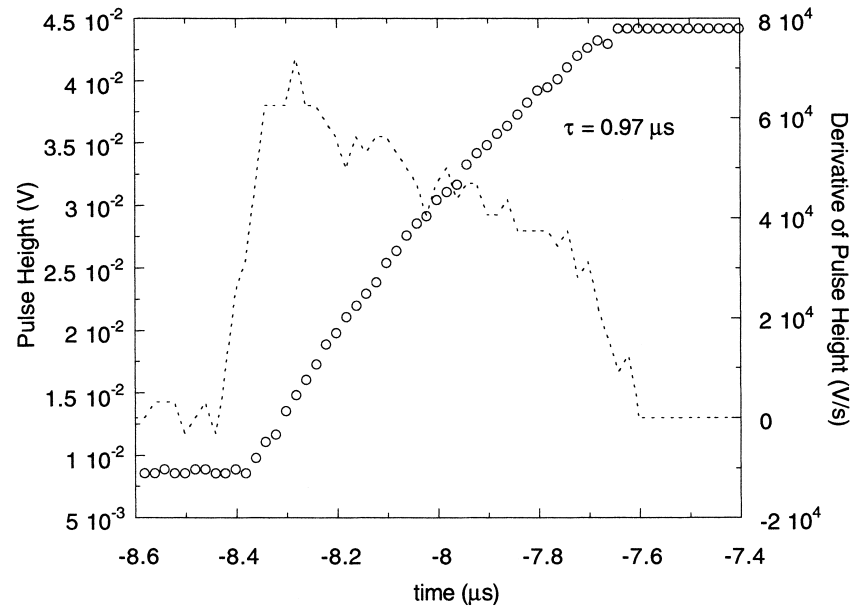


Fig. 44. The α -particle response pulse (circles) and time derivative (dotted line): $V = 60$ V; $d = 0.4$ cm [193].

no physical explanation has been offered for this observation. In short, while the method is suitable for determining the mean trapping lifetime, it does not provide reasonable mobility values.

Also shown in Fig. 44 is the slope of the pulse, which should be a simple decaying exponential with time constant τ_e . The fluctuations in this case are primarily due to noise. In many cases, however, pulses exhibit slope changes which suggest a non-uniformity in either the electric field or the mobility.

A measure of the variations found in measured mobilities is shown in Table 7, where both μ and $\mu\tau$ values from a number of authors are presented. While exceptions are not uncommon, μ_e values tend to be in the region of $1000 \text{ cm}^2/\text{V s}$ with μ_h typically being around $50 \text{ cm}^2/\text{V s}$. A more comprehensive list can be found in a paper by Jung [195].

The α -particle rise time maps for a $\text{Cd}_{1-x}\text{Zn}_x\text{Te}$ detector are shown in Fig. 45. This type of map along with the photocurrent mapping discussed below can, in principle, be used to determine the spatial variation in the mobility-lifetime product in a material such as CZT. In the upper map the rise

Table 7

Selected transport properties of cadmium zinc telluride ($\text{Cd}_{1-x}\text{Zn}_x\text{Te}$)

μ_e ($\text{cm}^2/\text{V s}$)	μ_h ($\text{cm}^2/\text{V s}$)	$(\mu\tau)_e$ (cm^2/V)	$(\mu\tau)_h$ (cm^2/V)	x	Reference
1000–1100	50	8×10^{-4} – 8×10^{-3}	3×10^{-6} – 3×10^{-5}	0.1	[249]
1000	7	—	2.8×10^{-5}	—	[250]
—	—	4×10^{-4}	8×10^{-5}	0.1	[229]
1050	90	6×10^{-4}	3×10^{-5}	—	[78]
880	51	—	—	0.2	[183]
1000	50	4×10^{-3}	9×10^{-5}	—	[10]
1350	120	—	—	0.2	[188]
1000–1300	—	$(2.4\text{--}8.9) \times 10^{-3}$	—	—	[251]
700–800	30–50	$(5\text{--}11) \times 10^{-3}$	$(2\text{--}8) \times 10^{-5}$	0.1	[43]

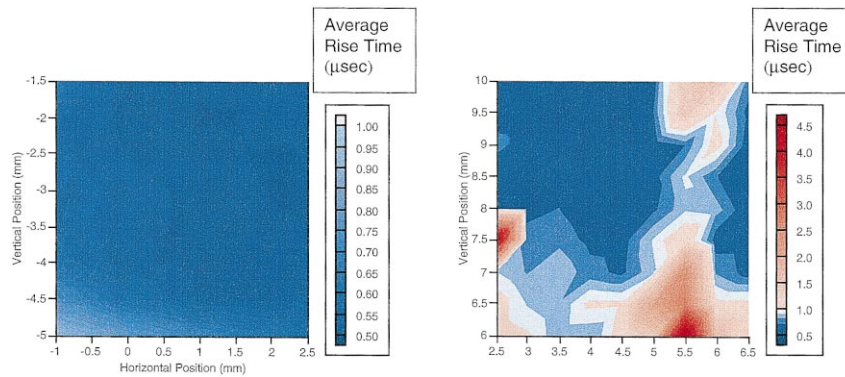


Fig. 45. The α -particle rise time maps showing nearly uniform response except for fringing of the electric field near the edge of the circular contacts (left) and rise time map showing regions of very slow response attributed to fast detrapping (right) [193].

time is essentially uniform except for a steady increase as one approaches the edges of the circular contact due to electric field fringing. Because of the limited spatial resolution (2 mm), the extent over which the electric field is reduced is somewhat exaggerated. A less typical map is also shown in this figure. In addition to the nearly uniform (blue) areas, there are areas where the average rise time is increased by an order of magnitude (red). A look at the typical pulse waveforms from the two areas shows a qualitative difference between the two. The waveforms from the slow areas have a short, fast linear portion followed by a long, slow exponential. This is typical of de-trapping phenomena [196]. The map, therefore, reveals a distribution of defects with a short de-trapping time.

Fig. 46 shows a photocurrent map obtained from the cross-sectional edge of a CZT detector using 632 nm excitation from a He–Ne laser. Ideally the contours of constant current should be horizontal, and that underlying structure is apparent in the figure. However, there is a great deal of other variation, much of which is probably due to roughness of the surface. By examining a one-dimensional line normal to the constant-current contours, one can obtain a Hecht-like curve and extract an electron mobility-lifetime product. The shape of the curve is often too insensitive to the value of $(\mu\tau)_h$ for that parameter to be determined. In many cases the curve deviates from the Hecht-

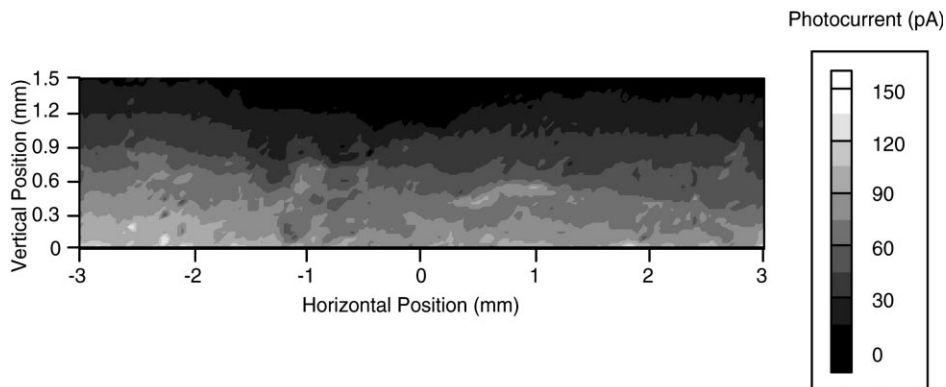


Fig. 46. Photocurrent map using 633 nm light from a He–Ne laser. Ideally the constant current contours should be horizontal [193].

like shape, suggesting an increase in the electric field or the mobility near the cathode. Evidence of an enhanced electric field near the cathode has also been seen in CZT planar detectors by electro-optical measurements [197].

Several investigators have developed mathematical models that utilize transport properties and weighting potentials to predict detector performance. These models are normally applied to different electrode geometries. Simulations by Prettyman [198,199] using a quasi-steady state model for detector operation yielded spectra in good agreement with experiment for a hemispheric CZT detector. Good results were also obtained for a unipolar CZT detector having a laterally-contacted design [200]. Similarly Lund [11] successfully simulated the performance of a large ($1\text{ cm} \times 1\text{ cm} \times 1\text{ cm}$) device with planar electrodes. Manfredotti and co-workers [201–203] have successfully generated simulated spectra for a number of materials, including CZT and CdTe. These studies have proven to be particularly useful in evaluating and optimizing detector designs and in helping to formulate material improvement strategies. The benefits of increasing the carrier lifetimes toward producing better detectors are apparent from the simulations.

4. Electrical contacts and current versus voltage measurements

While not discussed specifically to this point, it is nonetheless clear that the application of contacts is a prerequisite to any electrical measurements of CZT or its use as a detector. Before contacts are applied, the surface must be polished smooth; for $\text{Cd}_{1-x}\text{Zn}_x\text{Te}$ this is typically accomplished by polishing with grit followed by chemical etching. The most commonly used etchant is bromine in methanol, typically 5% Br by volume. Chen et al. [204] have studied other etchants and found that a smoother surface and reduced leakage current are obtained if the standard etch is followed by immersion in a 20% lactic acid/2% bromine in ethylene glycol solution. Chemomechanical polishing with a more dilute Br solution, 0.5% by volume, has been shown to produce a smoother surface, which is especially important for epitaxial growth on CZT substrates [205].

4.1. Electrical contacts

Gold and platinum are the most commonly used contact materials, and they can be applied by evaporation, sputtering, or electroless deposition. Burger et al. [206] have found that sputtered contacts have better adhesion, while electroless contacts have lower leakage current. No work has been published on optimization of parameters for sputtering. A related issue is passivation of surface states to reduce surface leakage current. Some researchers have found that oxidation of the surface by boiling in hydrogen peroxide [207] or by atomic bombardment [208] can reduce surface leakage current, but that there is an optimal degree of oxidation at which point additional soaking in H_2O_2 or exposure to an oxygen plasma causes the leakage current to increase. Passivation with organic polymers has also been effective in reducing surface leakage [209].

The current–voltage characteristic of a metal–semiconductor junction is determined by the barrier height at the interface. The simple Schottky–Mott theory of metal–semiconductor contacts [210] implies that high work function metals like Au form blocking contacts to n-type material and Ohmic or injecting contacts on p-type material, while for low work function metals such as In the opposite is true. For semi-insulating material it is more relevant to say that high (low) work function metals tend to be blocking (injecting) for electrons and injecting (blocking) for holes. This fact has long been the basis for CdTe p-i-n detectors, in which Au or Pt forms one contact and In the other

[211,212]. In most cases the short hole lifetime means that the injected holes contribute relatively little dark current. In fact it has been observed [213] that high leakage current is often a sign of good material with a relatively long hole lifetime. p-i-n type geometries [214] have been used in an attempt to reduce leakage currents but these devices tend to suffer from polarization problems. A similar structure was investigated with CZT but charge collection difficulties were encountered [215]. On the other hand, Sudharsanan et al. [216] have produced a true p-i-n device using evaporated p-ZnTe and n-CdS films on a CZT substrate, and [217] have done the same with liquid phase epitaxy of n- and p-type HgCdTe on CZT.

All of these contact schemes use blocking contacts, but it has been proposed [218] that the hole tailing problem could be greatly reduced if Ohmic contacts were fabricated, since charge carriers would be injected from the contacts to replace the trapped carriers. The same author claims to have fabricated a CdTe detector with Ohmic contacts that exhibited excellent resolution at 662 keV [219], but he has revealed few details about the fabrication process or the variation in the energy resolution with choice of contact material or crystal supplier. The disadvantage of this scheme is that the detector cannot rely on the aid of blocking contacts to suppress leakage current. Although more work is needed to verify the role of the In contacts, it is well accepted that techniques to overcome the effects of hole trapping would be of tremendous benefit to the technology area.

While contacts continue to be an area of much activity within this technology and while it is certainly the case that the contact material should not introduce new defects into the CZT, it does appear that the particular choice of deposition method used is not critical once an appropriate set of surface processing and electrode deposition conditions are identified. Of far greater concern is the choice of electrode material and in particular whether, for example, a high or low work function material is employed.

4.2. Current–voltage characteristics

Observed current–voltage characteristics for high-pressure Bridgman-grown $\text{Cd}_{1-x}\text{Zn}_x\text{Te}$ with metal contacts vary substantially with the characteristics of the crystal and the conditions under which the contacts are deposited. Near-Ohmic contacts are sometimes achieved, especially with electroless deposition, but in many cases the I – V curve has a pronounced non-linearity. The I – V characteristic is often described by an empirical relationship of the form:

$$I = aV^b \quad (31)$$

where b is called the Ohmicity and is equal to 1.0 for Ohmic contacts. I – V curves are observed with $b > 1$ and $b < 1$ [78].

A slight asymmetry about the origin is often observed in measured I – V characteristics. The origin of this effect is unclear, but it may be as simple as different levels of oxidation on the two surfaces. On the other hand, grossly asymmetric I – V curves are also sometimes seen. A striking example is shown in Fig. 47 which presents I – V curves for two halves of the same CZT sample with electroless gold contacts. Portion I has a highly asymmetric I – V curve, while portion II is nearly symmetric. One explanation for this phenomenon is a structural defect at the interface that exhibits a type of thermionic emission. These asymmetries in I – V characteristics do no real harm, since the detector can be biased with the polarity that gives the lower leakage current. Another phenomenon which is sometimes observed in I – V curves is a transition from linear to quadratic behavior at moderate bias, as shown in Fig. 48. This behavior can be explained as a transition to the space–charge limited regime due to perfectly injecting contacts [220].

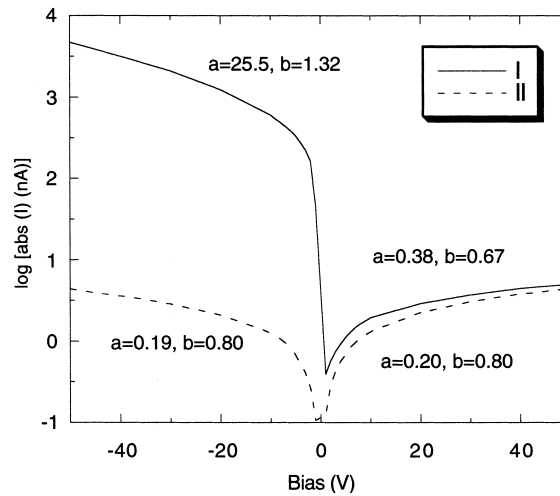


Fig. 47. Grossly asymmetric (solid) and nearly symmetric (dashed) I - V characteristic for two portions of the same $\text{Cd}_{1-x}\text{Zn}_x\text{Te}$ detector with electroless Au contacts [193].

4.3. Leakage currents

By mapping the leakage current of the wafer shown in Figs. 11 and 12, cracks were found to have a direct correlation to the leakage current; regions along and near the cracks exhibit as much as three orders of magnitude higher leakage current than regions away from the cracks. The results are shown in Fig. 49. The greyscale representing the values of the leakage current varies from 0.1 to 100 nA, and all measurements were performed at a detector bias of 100 V. The upper limit of the ammeter used to measure the leakage current was set as 100 nA (detector noise simply dominates any signals generated at this leakage current). It is worth noting that the electrical probe used to measure the leakage current was equipped with a guard ring which minimizes any surface leakage

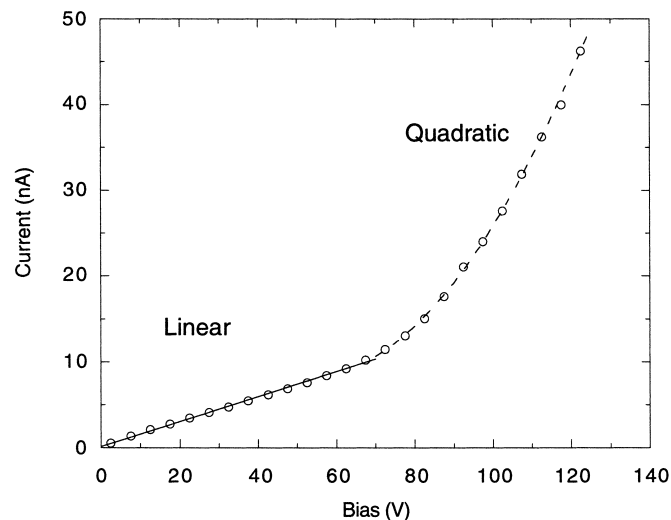


Fig. 48. I - V curve showing a transition to space-charge limited current at approximately 70 V. Every other data point is shown (circles) along with linear (solid) and quadratic (dashed) fits [193].

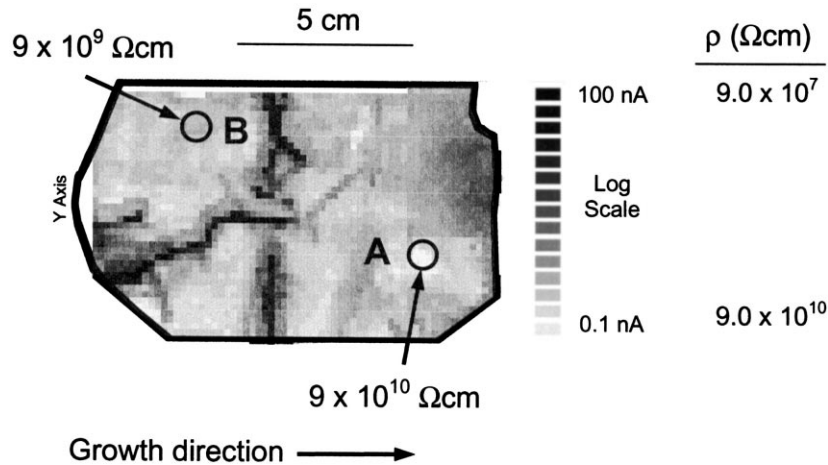


Fig. 49. Leakage current mapping data of the polycrystalline HPB $\text{Cd}_{1-x}\text{Zn}_x\text{Te}$ wafer investigated in Fig. 11. The greyscale values are shown in both current (A) and resistivity (Ωcm) [81].

current that may be present [221], and hence, the measured values are believed to correctly represent the bulk property. The bulk resistivity can be calculated from the measured leakage current, and it ranges from 9×10^7 to $9 \times 10^{10} \Omega\text{cm}$.

Although the width of the crack on the surface of the wafer is on the order of a few 10 of microns, the effect on the leakage current extends beyond the mm length scale. This is attributed to the geometry of the crack throughout the thickness (0.55 cm) of the wafer, the extent to which the secondary phases have accumulated onto the cracks, and the geometry of the probe tip. The average leakage current value is more than one order of magnitude higher along the cracks (23 versus 1.8 nA). In fact, the average along the cracks is probably grossly underestimated since the ammeter was set to a compliance of 100 nA. The results give evidence of an electrically shorted device along the cracks, with a conductive pathway that propagates through the entire thickness of the wafer. The enhanced leakage current along the cracks is most likely due to the impurities, tellurium or processing solutions which can decorate or infiltrate the cracks. For example, the cracks were found to be rich in carbon and zinc, and the metallic nature of these species lowers the local resistivity of the material and hence leads to excess leakage current along the cracks. Another possible source of metallic impurities along the cracks is the electroless gold deposited completely over one side of the wafer. As electroless deposition involves applying a chemical solution to the surface of the crystal, it is possible for the gold solution to have infiltrated the cracks [50]. In addition the excess tellurium, which has a lower melting temperature than CZT, during cooldown of the grown ingot can run along the sides of the ingot and infiltrate the cracks during the cooldown of the ingot.

The addition of zinc is expected to result in a lower detector leakage current due to the higher bandgap and hence higher resistivity of ZnTe. Clearly, this expectation is for an ideal situation, namely one in which the materials have uniform chemical and structural properties and the Fermi-level is pinned near mid bandgap. The semi-insulating property of HPB $\text{Cd}_{1-x}\text{Zn}_x\text{Te}$ is however a result of compensation mechanisms [147,222,223], possibly similar to the mechanisms involved in semi-insulating GaAs [29,93]. The variation in the composition may influence the amount and energy levels of the defects associated with the compensation mechanisms, and hence it is of interest to study this issue. High resistivity is indeed routinely achieved in HPB $\text{Cd}_{1-x}\text{Zn}_x\text{Te}$; for example, the resistivity is about $3 \times 10^9 \Omega\text{cm}$ for $x = 0$, $2.5 \times 10^{10} \Omega\text{cm}$ for $x = 0.04$, and $1.5 \times 10^{11} \Omega\text{cm}$

for $x = 0.20$ [41]. Some ingots do occasionally turn out to be of lower resistivity due to an inadequate concentration of deep levels to compensate for the shallow defects. In addition, the relationship between electrical resistivity and Zn composition is usually more complicated than the results reported by Butler et al. [41].

The leakage current mapping data (and the corresponding resistivity values) of the axial $\text{Cd}_{1-x}\text{Zn}_x\text{Te}$ wafer are presented in Fig. 49. Disregarding for the moment the regions in which the leakage current is dominated by the cracks, there appears to be no clear systematic distribution of the leakage current along the growth direction. For example, it is evident from Fig. 49 that there are regions with lower-content zinc that exhibit relatively high resistivity (marked as A) and regions with high-content zinc that exhibit low resistivity (marked as B), i.e. one order of magnitude difference in resistivity. These results clearly indicate the non-ideal distribution of the resistivity with Zn composition throughout the ingot (even by disregarding the regions dominated by the cracks). The amount of resistivity variation observed may be explained by considering that the material inhomogeneities give rise to fluctuations in the electron and hole concentrations (n and p), mobilities (μ_e and μ_h), and concentrations of compensating defects.

5. Relationship between material properties and detector performance

In this section, we discuss correlations between material properties and detector performance which have been suggested by both experiment and model calculations. One of the central issues related to CZT detector performance is the role of non-uniformities. More specifically, we have tried to answer, and provide quantitative justification for, the following questions:

1. Is the uniformity of CZT crystals available today an important factor in determining the performance of radiation detectors?
2. If uniformity is a problem, what types of inhomogeneities are the worst offenders in present day CZT?
3. If uniform material were available, would it be suitable for producing detectors useful in medical imaging and nuclear spectroscopy?

As a prelude we show in Fig. 50 an α -particle spectrum (^{244}Cm , 5.8 MeV), captured with a cadmium zinc telluride detector, which exhibits a dual peak. This is a fairly commonly observed problem that is probably due to differences in transport properties in different portions of the detector. This spectrum illustrates that even though material properties may be generally good, non-uniformity in those properties are often detrimental to detector performance, especially if one is interested in producing imagers where large areas of uniform material are required.

5.1. Correlation with gamma-ray mapping

With the above questions posed, an example of the uniformity of typical CZT material is shown in Fig. 51, where a gamma-ray imaging system was employed to map the response of this particular sample. This sample was graded by the manufacturer as a select counter, and the overall spectroscopic performance (shown in Fig. 51) confirms the manufacturer's grade. However, the spectral response from a "uniform" region (a) exhibits much better performance. In this example the majority of the device surpasses the performance required for any detector grade at 122 keV. If the cause of the non-uniformity could have been avoided, this device would probably have performed as a select discriminator, if not a spectrometer.

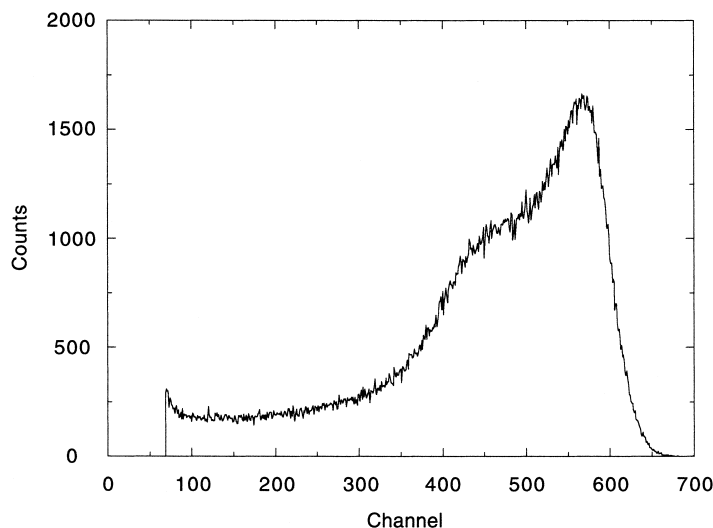


Fig. 50. An α -particle spectrum (^{244}Am , 5.8 MeV) showing an anomalous double peak due to a non-uniformity in detector response [193].

Material uniformity can be considered at different levels. First, CZT is known to be polycrystalline, so the gross uniformity in terms of grain density or volume can be discussed. On another level, the uniformity of the material and detector response within a single crystal grain can also be discussed. Most data available today pertains to inter-grain uniformity though some techniques to examine the material variation on a much smaller scale (within one grain) have been employed and these are also presented.

A detailed study of CZT uniformity and its relation to detector performance was performed by Brunett on a set of 15 samples to identify the crystalline features causing degradation in the detector performance. This work is discussed in detail in [224] along with a qualitative model confirming the conclusions reached regarding the effects of both grain boundaries and twins. Here, we summarize

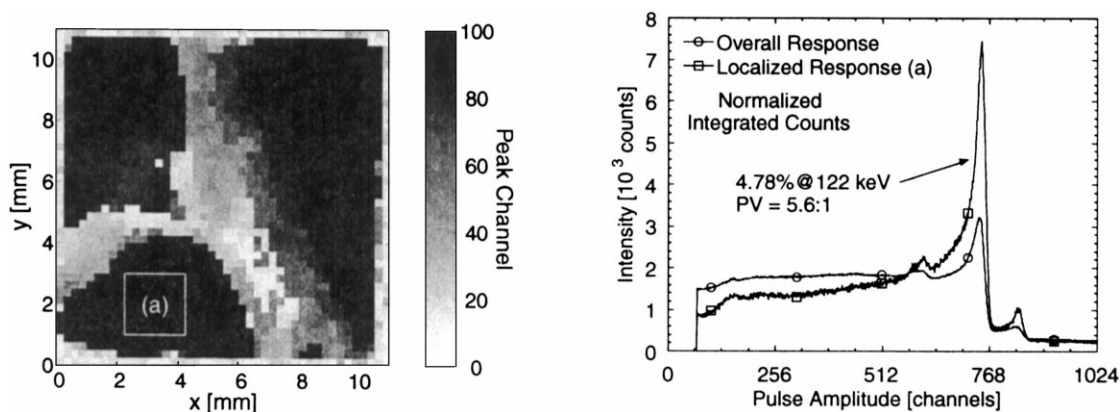


Fig. 51. Map showing the non-uniformity of commercially available CZT material (left). This map represents the channel at which the photopeak occurs over the area of the sample for 122 keV photons. A uniform device would not have the large regions exhibiting a low photopeak channel position. Also shown is a plot of the overall and windowed (a) spectral response. The non-uniformity of the material severely reduced the spectroscopic performance of this device.

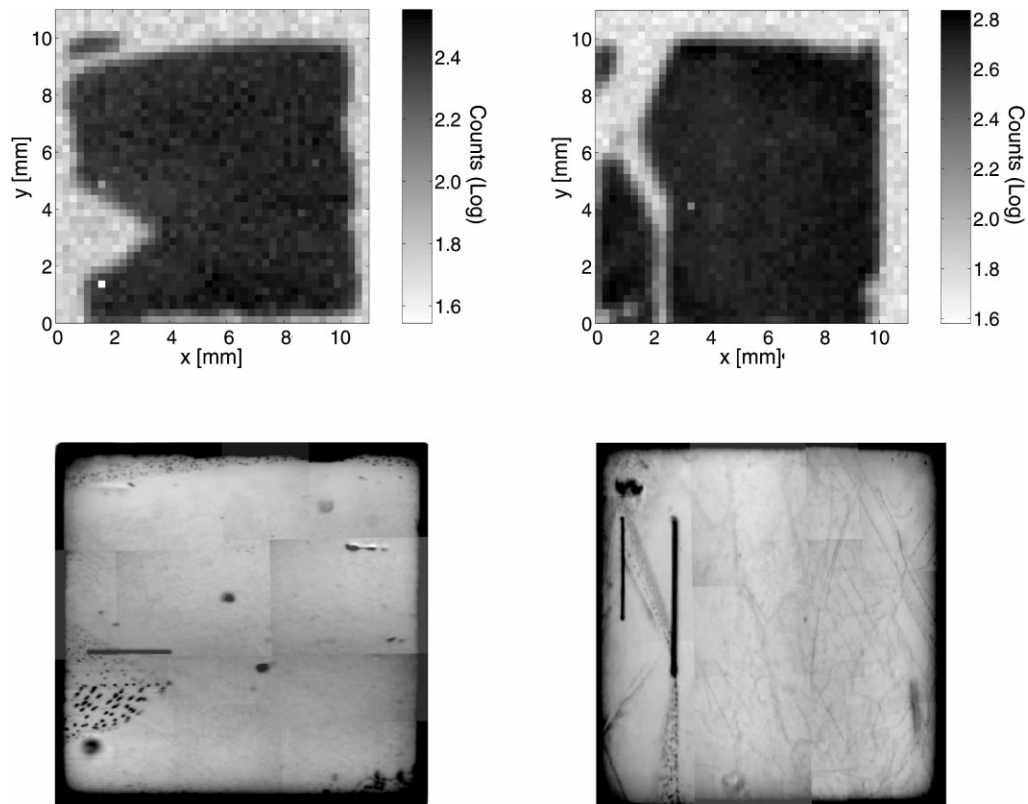


Fig. 52. Examples of typical detector response maps for CZT in which the contribution to the photopeak in the pulse height spectrum is shown (top). Also shown are the IR transmission images for each sample (bottom). The regions of the detector which exhibit poor spectroscopic response (top) also show defects in the detector material (bottom). The dark spots in the transmission are precipitates which usually segregate to crystalline boundaries. Nearly all instances of detector performance degradation are correlated with defect decorated crystalline boundaries within the detector.

the conclusions reached in that work providing, also, examples of the uniformity mapping data obtained with both gamma-ray and PL mapping.

An example of the results obtained in the IR/gamma-mapping is given in Fig. 52. The spatial response of each point at the photopeak is shown in the top plot and the IR transmission images are shown below. The regions which show reduced charge collection correspond to crystalline boundaries which are decorated with (Te) precipitates.

Two types of non-uniformity were observed, a charge trapping effect and a charge channeling effect. The most common effect (observed in 12 non-uniform samples) was a reduction of the measured charge within certain spatial regions, i.e. charge trapping. These features correlated with the decorated crystalline boundaries are shown in Fig. 52. A decorated boundary type of defect is also the most detrimental to the overall performance of the detector. A second, more subtle feature, charge channeling, was also observed in three of the non-uniform samples. The charge channeling feature was observed as a deficit of counts in a particular region of the pulse height spectrum. One would expect a loss of events for a region within the crystal that exhibits very low charge transport properties, but it should affect all channels above a threshold rather than simply a “window” in the pulse height spectrum. An example of a sample containing both types of defects is shown in Fig. 53.

The spatial contribution to one channel at the photopeak (i) and one channel within the low energy tail (ii) in the overall pulse height spectrum is shown in Fig. 53. Also shown is a plot of the

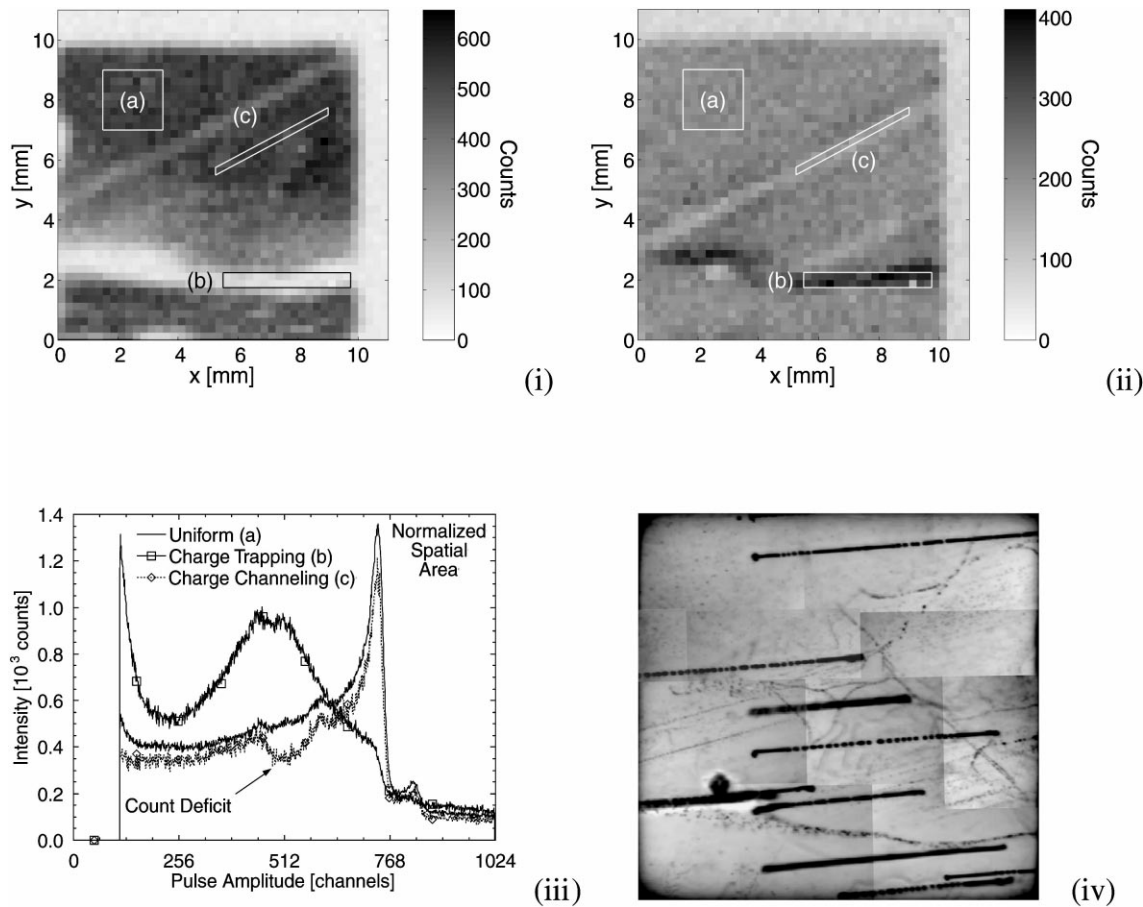


Fig. 53. Spatial detector response maps showing the contribution to one channel within the photopeak (i), and a channel in the low energy tail (ii) of the overall pulse height spectrum. Also shown is a plot of the detector response (iii) for several regions (a–c) over the device area. An IR transmission image (iv) showing the crystalline defects in the same detector is also shown. A typical charge trapping defect (b) is visible in the IR image and will cause a “dead” region in the photopeak response which corresponds to an increase in counts in the low energy tail as seen in (i), (ii), and (iii). A channeling defect (c) only affects a small “window” in the pulse height spectrum, which shows up as a spatial dependence in the detector response maps (the position of (c) changes as different channels are examined with the spatial maps). The defect causing the channeling response is not obvious in the IR image. The response of a uniform region (a) is shown for comparison in (iii).

spectral response (iii) for several spatial regions (a–c), along with the IR transmission image for this sample (iv). Typically the charge trapping response observed for a decorated boundary (b) will show a spreading of the counts from the photopeak into lower channels of the pulse height spectrum. A charge trapping defect will not show a spatial dependence in the spatial detector response maps. Referring again to Fig. 53, the charge trapping response is observed as an increase in counts in the low energy tail and a reduction of counts in the photopeak channel over the same spatial region (b) in (i), (ii), and (iii). A charge channeling type response (c) exhibits a spatial dependence in the detector response maps, and there is no corresponding reduction of counts in the photopeak over the same spatial region. Additionally, no obvious defects in the crystal are found in the IR image at the region where charge channeling is observed. If (c) were a charge trapping type defect, we would expect a large area between the diagonal lines of (i) and (ii) to show a significant reduction in the counts contained in the photopeak, along with a visible feature in the IR image (iii).

We have used the name “channeling” since a plausible explanation is a boundary which channels the charge encountering the boundary in the direction of the boundary. A second explanation would be that there is simply less charge generated near the region of the boundary. We do not believe that reduced charge generation is a viable explanation, since the bandgap of the material would have to be significantly altered in the boundary region to cause the observed response.

A crystalline boundary model was developed by Burnett [224] and is capable of supporting several possible effects caused by the boundary; including effects at the boundary itself and differences in the properties of the regions separated by the boundary. Three cases were considered: (1) a grain boundary which traps a fraction of the charge which encounters it, (2) a twin boundary which channels charge along its length, and (3) an inert boundary with each “grain” of the device exhibiting differing charge transport properties. Usually several of these boundary effects occur concurrently, but there are particular isolated examples of two of these effects in the experimental data.

The most common defects that are observed in commercial CZT material are grain boundaries. The effect of a grain boundary on detector performance is almost always catastrophic, and these defects must be avoided for all spectroscopic and most counting applications utilizing CZT. An example of the effects of a grain boundary is shown in Fig. 54, where the spatial detector response is plotted for a channel in the low energy tail of the photopeak in the overall PHS. The region in the lower left corner of the device contains a grain boundary which significantly alters the charge collection properties. A narrow band can be seen where there is a lack of counts, and a greater intensity of counts can be seen on either side of this band. The rectangular box indicates the location where individual PHS were extracted for comparison with the simulations.

A series of simulated PHS for several boundary positions is given in the left plot of Fig. 55. The PHS obtained when the boundary is at either the cathode or the anode are the same as if there were no boundary, since essentially all of the thickness of the detector is unaffected. If the boundary occurs one quarter of the detector thickness away from the cathode, an additional peak in the lower

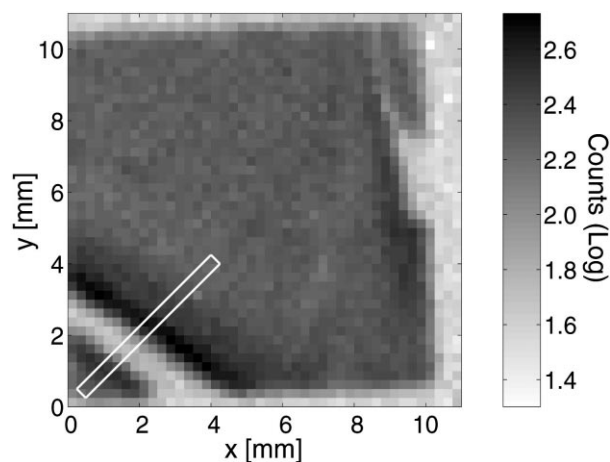


Fig. 54. Plot showing the spatial spectroscopic response of a detector to 122 keV photons from ^{57}Co . Each pixel represents the contribution of that spatial point to a window of eight channels, which is centered in the low energy tail of the integrated pulse height spectrum. A white box represents the region from which several spectra were extracted for comparison with the simulated data.

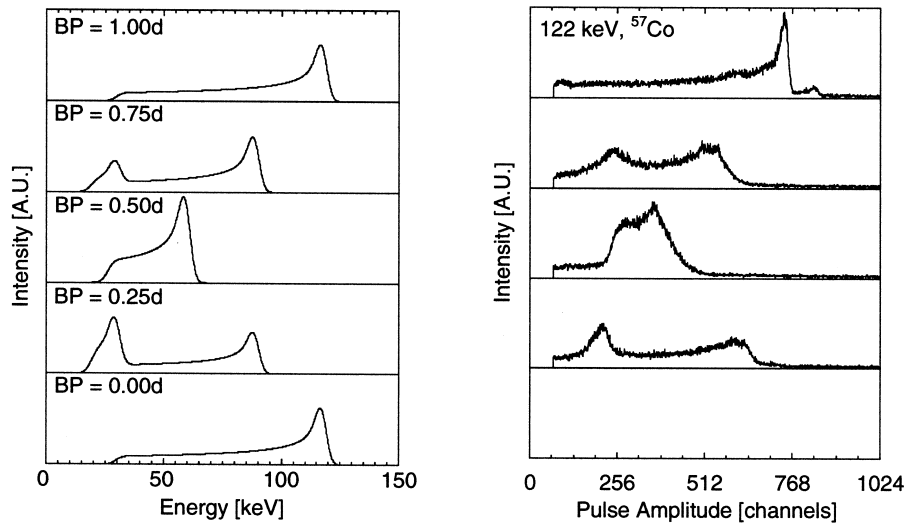


Fig. 55. Plots showing the expected spectral response for a 100% charge trapping boundary for several positions of the boundary through the detector thickness (left). The experimental results extracted from the region indicated in Fig. 54 are also shown (right). Notice that the relative amplitudes of the separate peaks for boundary positions 0.25d and 0.75d are consistent between the simulations and experimental data.

channels is observed, along with the shifting of the main peak to somewhat lower channels. The lower channel peak results from the motion of the carriers created above the boundary, which are limited to a quarter of the possible drift length. The higher channel peak results from the carriers created below the boundary, which can travel three-quarters of the thickness. At a boundary position of one-half, the carriers can travel one half of the possible drift length, and a single photopeak will occur at an amplitude channel which is approximately half of the “normal”. Since the carriers can only travel half of the thickness of the detector, only half of the maximum charge is measured and a lower photopeak channel occurs in the PHS.

Several experimental results and analytic simulations suggest that twins play a subtle but important role in CZT detector performance. Twins are common in CZT and appear as a single twin plane, a narrowly spaced ($\sim 100 \mu\text{m}$) pair forming a band, or as a series of several twins forming a “banded” region in the detector. However, twins are difficult to detect with infrared transmission, which is used to identify other types of crystalline boundaries, because of their tendency to be undecorated with inclusions. At one point, twinning defects were assumed to be relatively harmless [225], and they frequently are for simple planar devices. However, as CZT technology has improved and imaging devices were investigated, strange efficiency values were observed for neighboring imaging elements. One particular pixel would have a low efficiency while a nearby element would give greater than 100% efficiency [226]. After further investigation, a twinned region was found to be “channeling” the charge from under one pixel to pixels as far as several mm away. Fig. 56 gives the response observed for a region containing a twin band [227].

The PHS for the overall device is shown in the top left plot of Fig. 56, along with three specific pulse height indices (43, 68, and 93). Also shown in Fig. 56 are three maps corresponding to the spatial response at pulse heights 43, 68, and 93. A narrow diagonal region is visible where a slight deficit of counts occurs; a rectangular box has been placed on the maps to highlight the deficit region. Also shown on each map is the vertical position of the count deficit band. The spatial position of the feature exhibits a dependence on the channel index chosen. Based on the experimental data, a

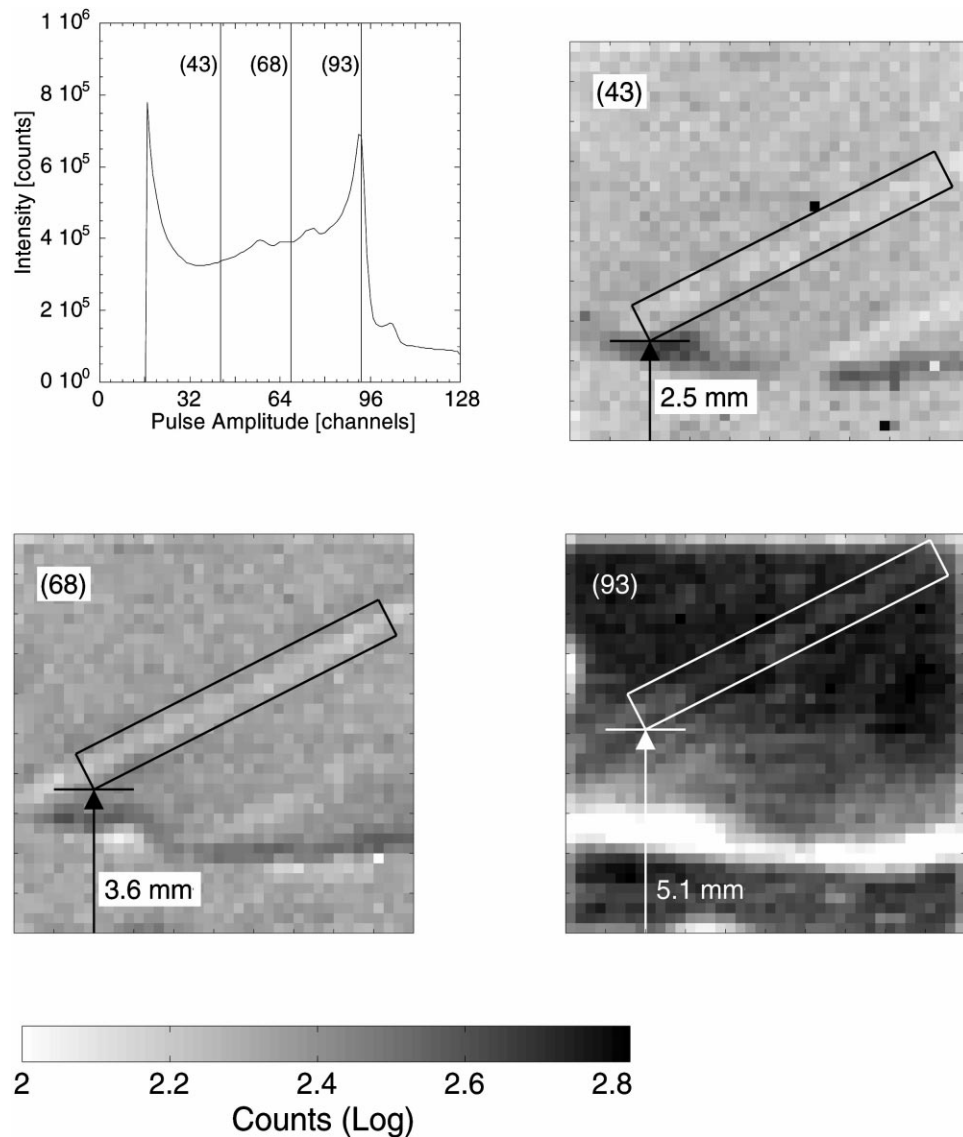


Fig. 56. Plots showing the spatial dependence of the channeling feature (twin boundary) as a function of channel index. The particular channels used to generate the spatial maps are shown in the top left plot. The resulting spatial maps show the change in spatial position of the count deficit as indicated by the rectangular regions.

twin boundary does not extensively affect the collection of carriers encountering it. Carriers which encounter the twin boundary still contribute to the majority of the measured charge, giving rise to a photopeak in the PHS.

A simulation at several different boundary positions is shown in the left plot of Fig. 57. Here a narrow notch in the PHS is observed which is a function of boundary position. The counts normally occurring at the notch position are shifted to slightly lower channels. The intuitive explanation for a charge channeling response type is that the increase in the path length traveled by carriers moving along the boundary increases the amount of charge trapping, which causes a slightly lower amount of charge to be induced when compared to unimpeded carrier motion.

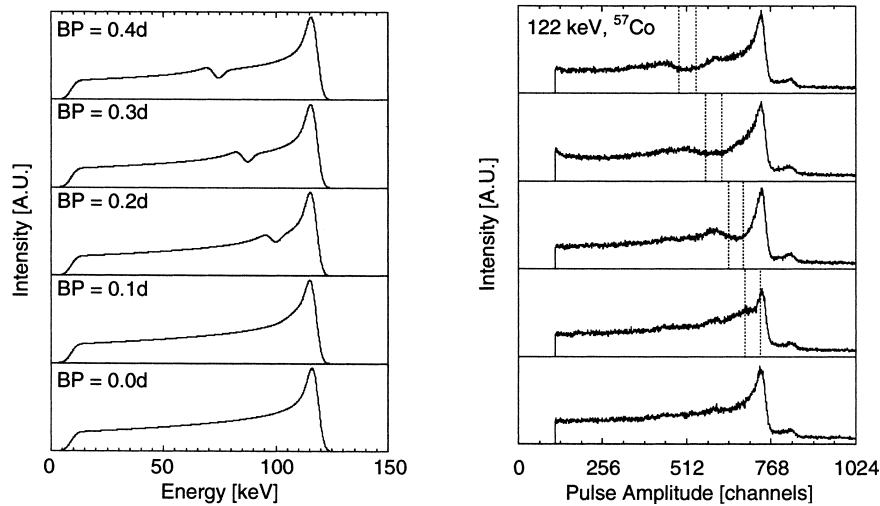


Fig. 57. Plot showing the expected pulse height spectra for a channeling boundary located at different positions within the detector (left). Experimental data extracted from regions like those indicated by the rectangles in Fig. 56 are also shown (right). The similarity between the experimental data and the simulations suggests that an inclined charge channeling twin boundary exists within the detector.

5.2. Correlation with photoluminescence

5.2.1. Low-temperature photoluminescence

The low-temperature PL spectrum gives an excellent overall picture of material quality, and it is natural to expect that it would be valuable as a predictor of detector performance. Fig. 58 compares PL spectra for a high-quality detector and a non-detector-grade sample. The clearest indicator of the difference in quality is that the spectrum of the detector-grade sample is dominated by the excitonic luminescence, while that of the poor-quality sample is dominated by defect-related luminescence. Another indicator which is not obvious is the sharpness of the spectrum, that is, the extent to which

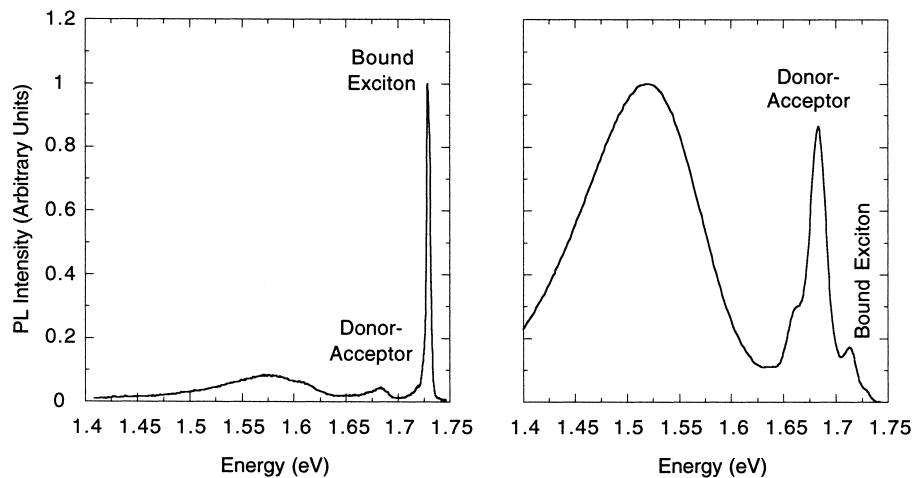


Fig. 58. A 4.2 K PL spectra for detector grade (left) and non-detector grade $\text{Cd}_{1-x}\text{Zn}_x\text{Te}$ samples. A clear correlation (peak widths and near-band-edge PL intensity) is seen between the material quality in terms of PL and in terms of detector performance.

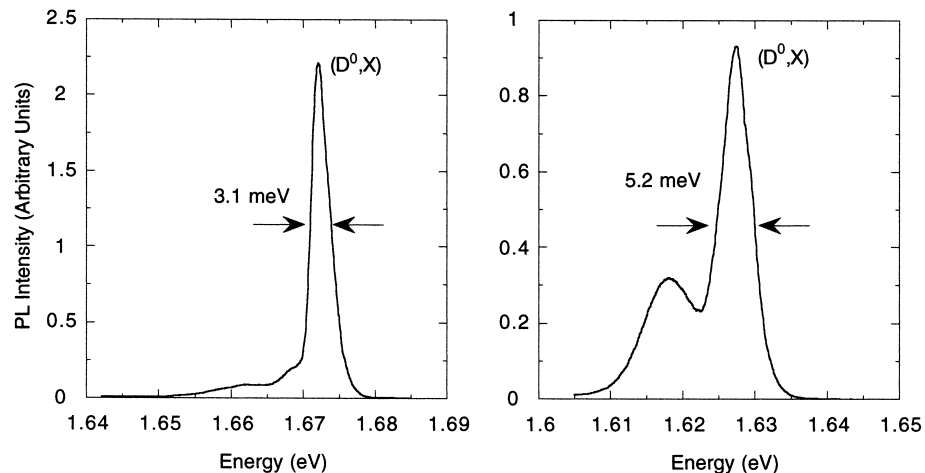


Fig. 59. A 4.2 K PL spectra for spectrometer grade (left) and counter grade $\text{Cd}_{1-x}\text{Zn}_x\text{Te}$ detectors illustrating the use of the FWHM of the donor-bound exciton peak as a qualitative measure of quality [193].

adjacent peaks can be resolved. A third indicator which applies to CZT and which is not well understood, is that in high-quality samples the donor-bound exciton (D^0, X) peak tends to be dominant, while in lower-quality samples the acceptor-bound exciton (A^0, X) luminescence is stronger.

For quantitative comparisons there are at least two measures of material quality which one can use: the ratio of the excitonic luminescence intensity to the defect or donor–acceptor luminescence, and the width of the excitonic peaks. One can use the width of the donor-bound exciton (D^0, X) peak as the basis for evaluating detector or material quality. For this measurement the laser beam is unfocused so that it illuminates a large portion of the sample surface. Since the (D^0, X) peak tracks the bandgap closely, and the bandgap varies with x , macroscopic differences in composition will cause broadening of the peak in addition to that caused by microscopic alloy fluctuations and defects. Fig. 59 compares near band edge PL spectra for spectrometer-grade (high performance) and counter-grade (poor performance) detectors. The excitonic luminescence of the spectrometer-grade sample is clearly much sharper.

Fig. 60 shows the peak-to-valley ratio for the 59.5 keV photopeak in the pulse height spectrum of ^{241}Am versus the FWHM of the (D^0, X) peak in the PL spectrum. There is a surprisingly direct relationship between the two, except for a few outlying points. The effectiveness of this particular measure as a predictor of detector performance is a consequence of the fact that the same material factors that reduce performance, such as defects, microscopic alloy fluctuations and macroscopic composition variation, also cause variations in the potential felt by excitons, resulting in a broadening of the (D^0, X) peak.

5.2.2. Room temperature photoluminescence mapping

One of the most important differences between gamma-ray characterization and RTPL analysis is the volume of the detector that is probed. The RTPL excitation is not deeply penetrating radiation, and therefore only a small fraction of the sample depth is probed. The same sample containing a twin band, examined earlier, was analyzed using the RTPL-mapping system. The RTPL response was first measured with a coarse map over the entire device area, which identified a line feature with the correct orientation to be responsible for the behavior observed in the gamma-response maps described above (Fig. 56). A high-resolution RTPL map over a 1 mm^2 area at a spatial resolution of

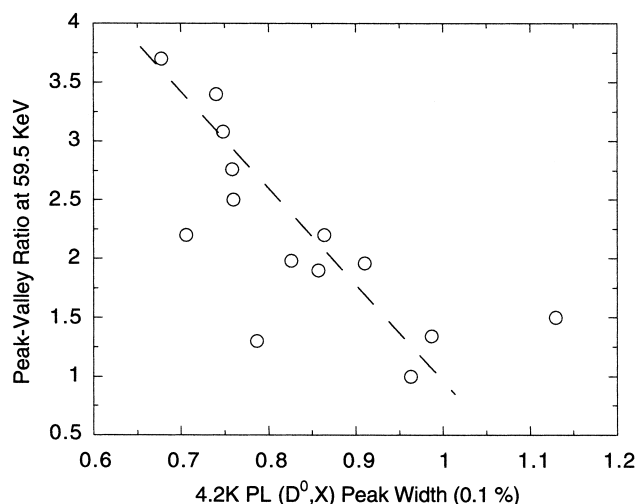


Fig. 60. Correlation between detector performance and width of (D^0, X) peak in the PL spectrum. The dashed line is a least-squares fit excluding the three outlying points [193].

10 μm is presented in Fig. 61. A linear feature composed of two parallel lines are seen in the bandgap variation map of Fig. 61(a). The RTPL signal intensity shown in Fig. 61(b) is sensitive to surface features, such as scratches on the sample. Most of the features observed in the RTPL intensity map are not found in the bandgap variation map. Only the two parallel lines are visible in both maps, which implies that these features are caused by defects in the crystal and not simply surface scratches. A linear sampling of the measured bandgap was extracted from the horizontal line indicated by the arrow in Fig. 61(a) and plotted versus position in Fig. 61(c). The linear features appear as two spikes in the measured bandgap about 250 mm apart. These spikes exhibit tails on the right side, indicating that the feature is inclined into the sample on the right side of the feature. In addition to an elevated bandgap at the feature itself, the spectral width of the RTPL spectrum is greater as shown in Fig. 61(d). Typically, spectral broadening in photoluminescence is attributed to poorer crystalline quality of the material.

In some samples, the spectroscopic quality of the CZT detector was correlated with the uniformity measured by RTPL mapping. An example is given in Fig. 62, which shows the gamma-response, RTPL bandgap variation, and IR transmission image. The map in Fig. 62(i) shows the spatial variation in the counts appearing in the 122 keV photopeak. The lower third of the detector exhibits much greater spectroscopic capability as shown in Fig. 62(ii). This plot gives the integrated pulse height spectrum in the regions indicated by (a) and (b). A decorated crystalline grain boundary separates the lower third of the detector and is visible in Fig. 62(iii). Several linear features are apparent in the coarse RTPL bandgap measurement (Fig. 62(iv)), including the crystal boundary isolating the region of enhanced spectroscopic performance. Even the coarse RTPL bandgap variation data show differences in bandgap variation on opposite sides of the boundary. The bandgap variation extracted from the RTPL data is plotted in Fig. 63. The boundary is clearly visible as a nearly horizontal line in the map of the bandgap. The bandgap at the boundary is higher, suggesting that either a larger zinc fraction occurs at the boundary or that the material at the boundary is under strain which alters the bandgap of the semiconductor. This higher variation in bandgap coincides with the region of the detector exhibiting lower spectroscopic performance.

In a room temperature photoluminescence map one can use the standard deviation, σ , of the zinc fraction divided by its mean, x_0 as a figure of merit for Zn uniformity. The 59.5 keV peak-to-valley

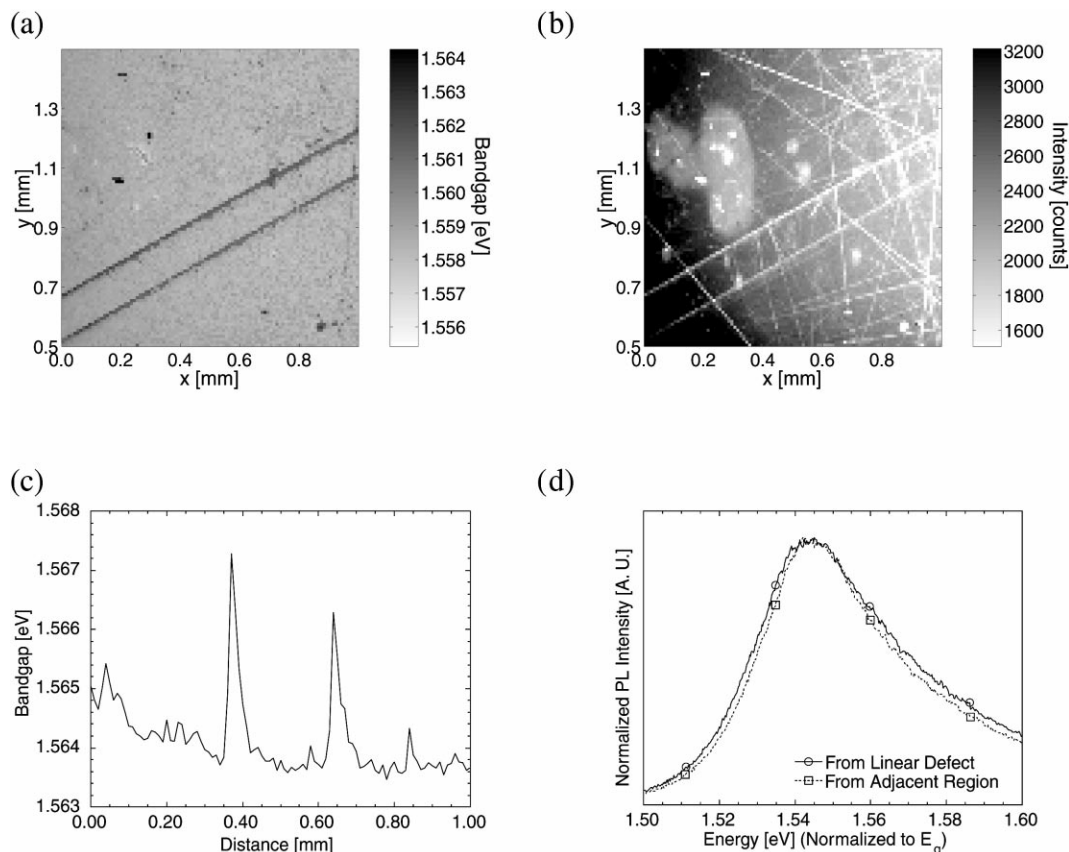


Fig. 61. A high-resolution RTPL map showing the bandgap variation as a function of position over a portion of the region indicated in Fig. 56. The spatial resolution was 10 mm and an acquisition time of 1 s was used. Notice the two diagonal lines where the bandgap shifts to higher energy. Also shown (b) is a plot of the intensity of the free exciton recombination (X_1). Notice that the measured bandgap is not directly correlated with the signal intensity of the RTPL, implying that the variation in the bandgap is due to crystalline defects and not variation in the RTPL intensity related to surface features. A plot showing the variation of the bandgap as a function of position is also given (c). The data were extracted from a horizontal line in the area indicated by the arrow in map (a). The two lines in map (a) appear as peaks in the measured bandgap of plot (c). The peaks exhibit a “tail” on the right side implying that the defect responsible for these features is inclined to the bottom right into the sample. In addition to the higher bandgap, the linear features also exhibit a broadening of the RTPL spectrum as shown in plot (d).

ratio is plotted against σ/x_0 in Fig. 64. As with the low-temperature PL correlation, there is a fairly direct relationship, but with a greater degree of scatter and with the outlying points being farther from the main trend line. The origin of at least one of the outlying points is understood based on the PL map for that detector (see Fig. 65). The figure reveals a large inclusion, as well as a chain of smaller inclusions. The latter may be distributed along a grain boundary. Because the PL spectrum shifts to higher energy near these inclusions, as discussed previously, the measured variation is unusually high. On the other hand, the effect of these inclusions on the performance of the detector appears not to be as great as their impact on the uniformity measurement. It may be that inclusions of this type do not generally have much impact on detector performance, or it may be that the small region on the sample surface which was mapped was not representative of the bulk of the sample.

Larger area room temperature PL maps covering $5 \text{ mm} \times 5 \text{ mm}$ in $250 \text{ }\mu\text{m}$ increments have also been performed [193], and these show strong correlation with no extreme outlying points. This result

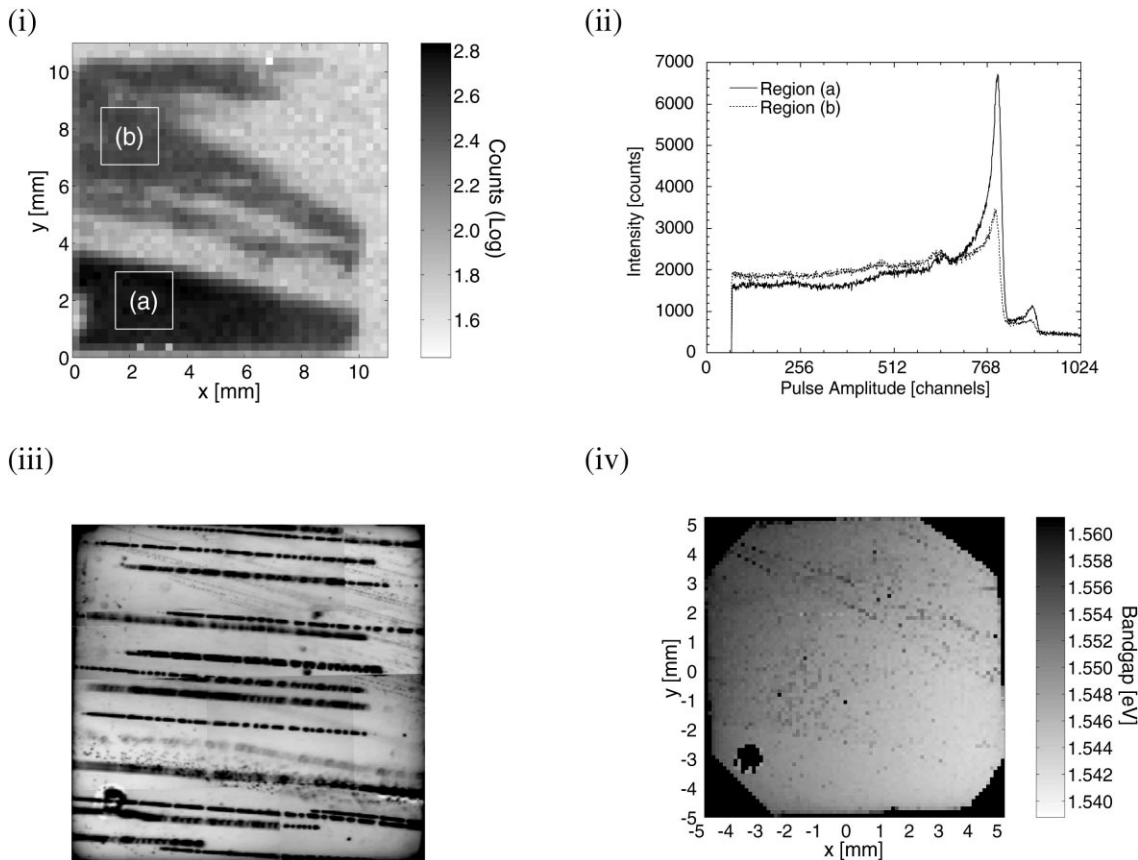


Fig. 62. A map showing the spatial contribution to the 122 keV photopeak from ^{57}Co is given in (i). The difference in the quality of the resulting pulse height spectrum from two spatial regions is shown in plot (ii). Several grain boundaries and pipes are present in the detector identified in the IR transmission image (iii). The bandgap variation over the detector surface as measured by RTPL is given in map (iv). The intersection of several grain boundaries with the surface of the sample appear as linear features in the RTPL map. The lower third of the sample exhibited greater uniformity in the measured bandgap, which corresponds with the enhanced spectroscopic performance observed over the same area in the gamma-response map (i). The region indicated by the box in (iv) was examined using RTPL mapping at higher resolution to study the effects of a grain boundary.

suggests that it may be valuable to have a materials selection system with adequate throughput to permit large area mapping.

While plots such as Fig. 60 are useful for seeing a general trend, it is desirable to have a quantitative measure of how well a measured parameter predicts detector performance. If a linear regression is performed on the data of Fig. 60, a correlation coefficient of 0.73 is obtained, the implication being that 53% of the variation in peak-to-valley ratio can be predicted by the (D^0, X) line width using a linear relationship. An additional predictor that has been considered is leakage current. Adding this parameter only increased this percentage to 60% in one study [193], so that incorporating the leakage current improves the predictive value only slightly over the single-parameter correlation.

Thus, it has been shown that material uniformity is definitely an important factor determining the performance of CZT radiation detectors. In fact, gross defects due to grain boundaries are probably the most significant factor limiting the performance of many CZT devices. Specifically, two types of crystalline boundaries that lead to performance loss have been identified. A grain

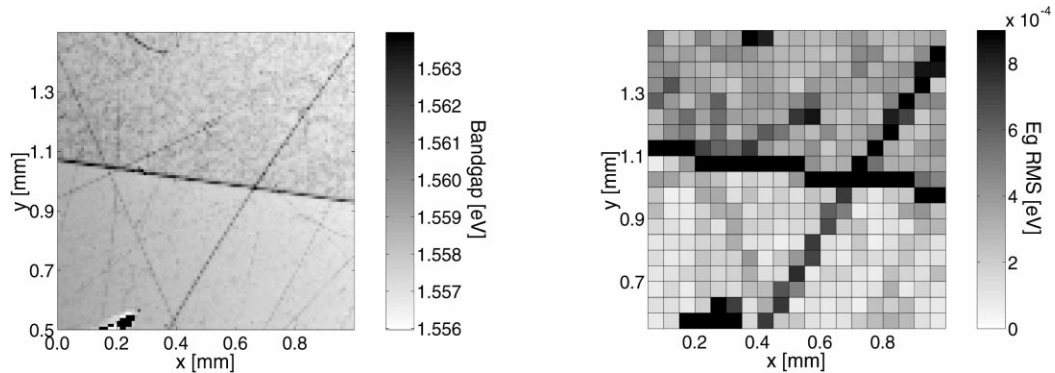


Fig. 63. A high-resolution map showing the bandgap variation (left) across the grain boundary highlighted by the white square in Fig. 62 (iv). This measurement was performed at a spatial resolution of 10 mm with a 1 s acquisition time. The spatial map was broken into blocks containing 25 spatial points each, and the RMS value of each block was calculated. The resulting map is shown at right. The region of the crystal above the boundary shows a higher average spatial-RMS value for the bandgap variation. The material below the boundary is more uniform, which is supported by the superior detector response observed in the gamma-response map (Fig. 62).

boundary is the most common, and will greatly reduce the performance of the region of the CZT device containing the grain boundary. The second crystalline boundary identified, the twin boundary, will cause charge to channel along its length. The charge channeling effects of twins will be less significant in planar CZT devices, but may have serious performance implications for imaging or unipolar devices which rely on particular carrier trajectories.

5.3. Charge collection efficiency

The effects of cracks on electron charge collection efficiency (e^- CCE) have been analyzed, and as an example this has been measured on the same axial $\text{Cd}_{1-x}\text{Zn}_x\text{Te}$ wafer previously discussed. The e^- CCE mapping results are shown in Fig. 66. The raw data obtained from the e^- CCE mapping measurements are peak channel values from the α -particle pulse height spectrum (PHS) taken at each

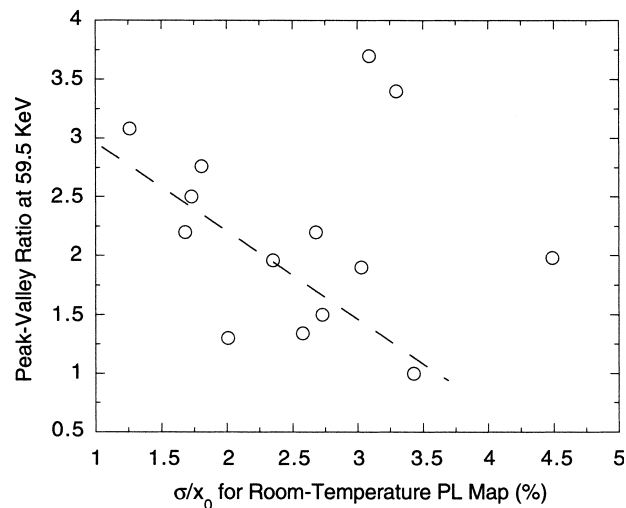


Fig. 64. Correlation between detector performance and variation in the room temperature PL map. The dashed line is a least-squares fit excluding the three outlying points [193].

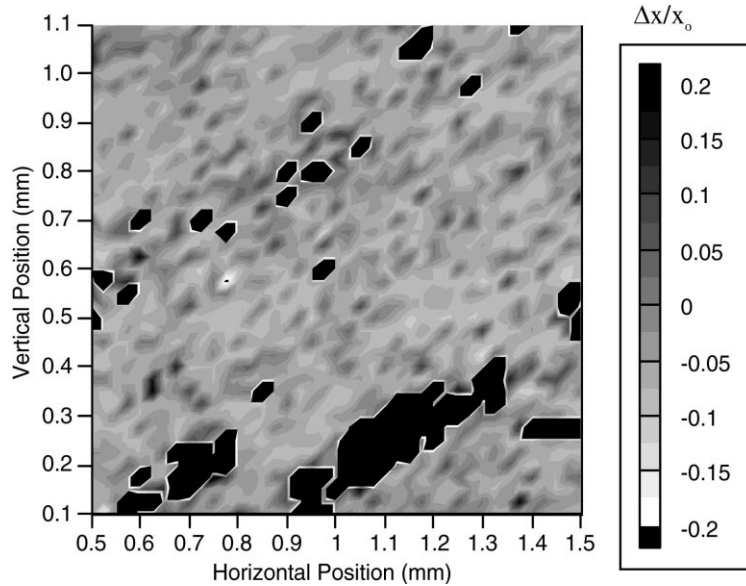


Fig. 65. Room temperature PL map for the outlying point in Fig. 64 showing inclusions (black) of various sizes [268].

2 mm increment position under a detector bias of 100 V. As an example, two PHS are also shown in Fig. 66 representing low peak channel (low $(\mu\tau)_e$) and high peak channel (high $(\mu\tau)_e$). By comparing the spatial locations of the cracks (Fig. 12) to the e^- CCE mapping in Fig. 66, it is clearly evident that low e^- CCE corresponds to the regions of the cracks. The cracks which project entirely through the

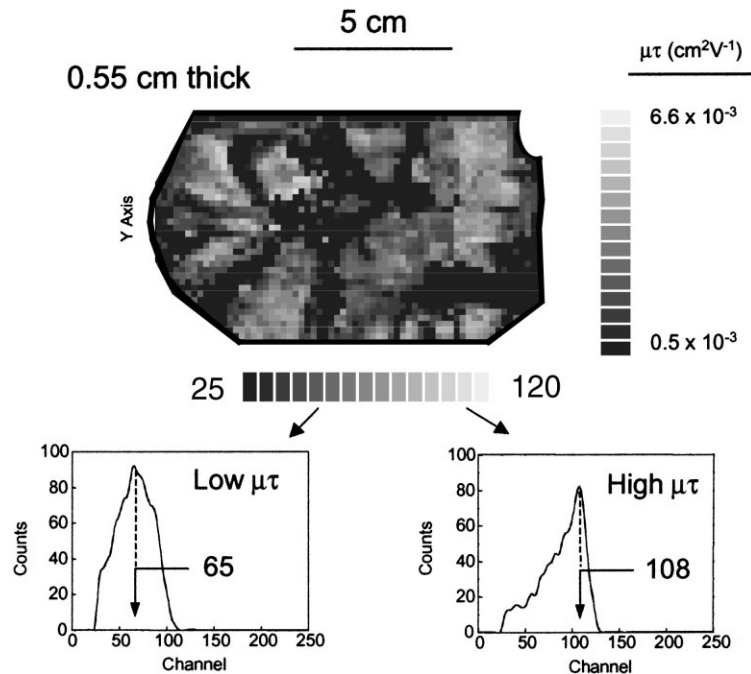


Fig. 66. Electron charge collection efficiency (e^- CCE) map of the same $\text{Cd}_{1-x}\text{Zn}_x\text{Te}$ wafer shown in Fig. 12 performed at a detector bias of 100 V. Two pulse height spectra are shown representing low and high peak e^- CCE. Low e^- CCE is measured along/near cracks as well as across grain boundaries and within particular grains [81].

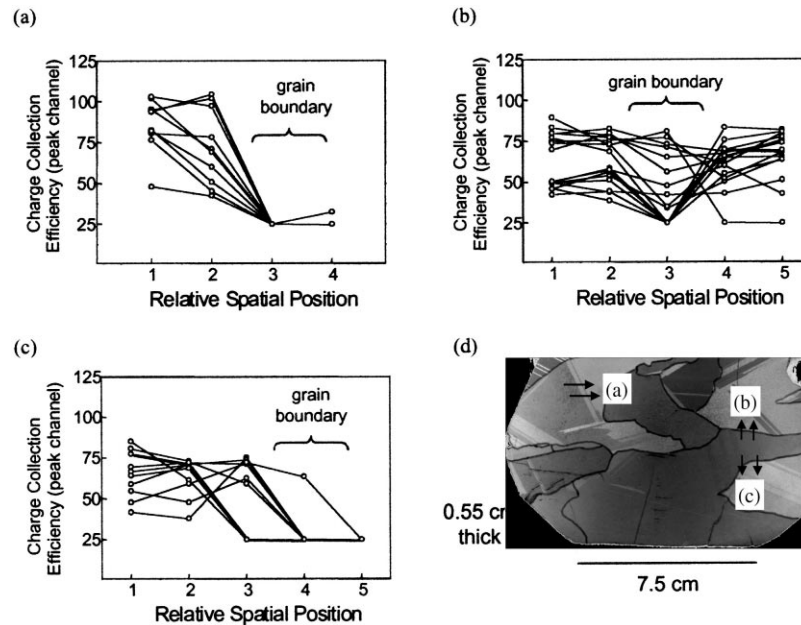


Fig. 67. Three examples showing grain boundaries that lie in the path of electron transport, which lower the charge collection efficiency.

thickness of the wafer act as shorting paths ($I_L \geq 100$ nA), while those that do not traverse the entire thickness show no shorting effect (but show higher I_L than non-crack regions). This observation gives evidence that small cracks or microcracks that do not propagate through the detector mainly limit the charge collection by serving as recombination sites, and not necessarily by serving as regions of excessive leakage current. As a final note, it has been reported [82] that the occurrence of cracks in the HPB $\text{Cd}_{1-x}\text{Zn}_x\text{Te}$ ingots has been significantly reduced mainly by improving the thermal environment during crystal growth.

An analysis of the electron charge collection efficiency mapping of Fig. 66 reveals that grain boundaries clearly impede the electron transport. The extent to which it affects the charge transport depends on the particular projection of the grain boundary through the thickness of the wafer near the measurement region. Fig. 67 provides three examples which illustrate this behavior. In this figure, (a), (b), and (c) plot the charge collection efficiency (data taken from Fig. 66) as a function of relative spatial position (each spatial position = 2 mm) for the three grain boundary “crossings” indicated in (d). The grain boundary crossing shown in (a) is a clear example; moving from left to right across the boundary, the amount of charge collected abruptly decreases to a minimum. Similar results are observed in (b) and (c), although clearly, not all “crossings” show this behavior. This can be attributed to the projection of the grain boundary through the thickness of the wafer, and also to the possibility that the 2 mm increment stepping may skip over most of the grain boundary. These results are in agreement with that of Luke and Eissler [228], who demonstrated charge trapping effects of a grain boundary in a $\text{Cd}_{1-x}\text{Zn}_x\text{Te}$ detector. He showed that a grain boundary in the path of the traveling electrons abruptly stopped the charge movement, hence giving rise to a lower charge signal.

An analysis of Fig. 66 indicates that twin boundaries tend to have little degrading effects on the electron charge collection efficiency. In other words, the twin boundaries do not appear to serve as catastrophic charge trapping sites. This might be explained by the fact that unlike grain boundaries, twin boundaries typically do not contain broken bonds. These results are also consistent with that

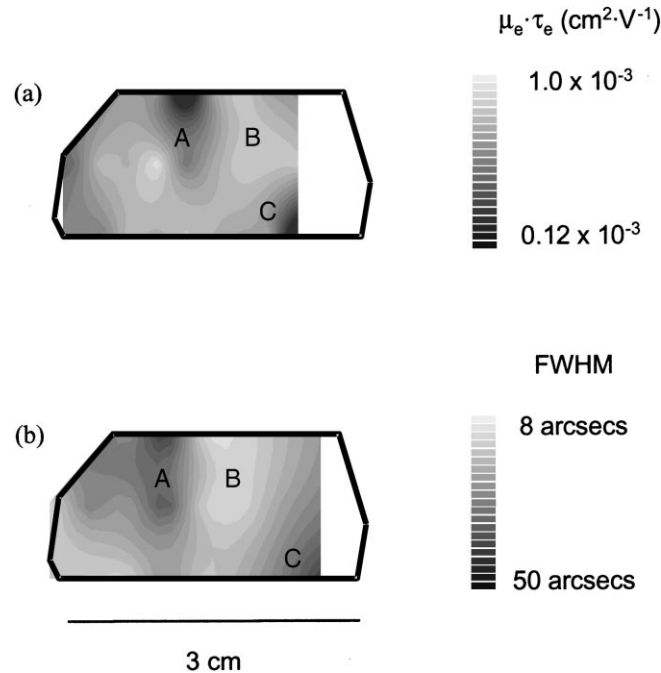


Fig. 68. Experimentally measured (a) electron charge collection efficiency (normalized $(\mu\tau)_e$) of the sample shown in Fig. 16. The crystal quality mapping from Fig. 16 is reproduced in (b).

observed by Luke and Eissler [228], who showed that full charge collection was obtained “through” twin boundaries. However, the electron charge transients showed two different slopes, suggesting the presence of a non-uniform electric field distribution across the detector region containing the twin boundary.

Fig. 68 presents a comparison of the e⁻CCE mapping to the TAD ω -scan mapping (reproduced from Fig. 15) for a single crystal Cd_{1-x}Zn_xTe sample. For the e⁻CCE mapping, the contour shades represent $(\mu\tau)_e$ values, i.e. the raw data have been converted to $(\mu\tau)_e$ using the Hecht relationship. Some clear correlations exist. For example, in Fig. 68, regions marked A, B, and C correlate higher crystal quality to higher $(\mu\tau)_e$ and mosaic/tilt regions to lower $(\mu\tau)_e$. However, there are also regions that do not show this relationship, such as the lower left corner region of the sample shown in this figure; this region has a relatively high crystal quality but low $(\mu\tau)_e$ was measured. Clearly, other factors (namely chemical imperfections) affect the charge transport properties. However, in terms of the relative effects of the structural defects on detector performance, one consistent correlation is always obtained: poor crystal quality is always associated with lower e⁻CCE. Further considerations related to e⁻CCE and detector performance are discussed by Nemirovsky et al. [229]. In general, most measurements show that the biggest problem limiting the CCE's of electrons and holes is the density of grain boundaries, and that the most important property to improve detector performance is to increase the size of the single crystals within the ingots without creating new trapping sites within the single-crystal volumes.

5.4. Modeling of uniformity effects on detector performance

The experimental studies described in the previous section are useful in that they demonstrate that certain material characterization techniques can be employed to a certain extent, as predictors of

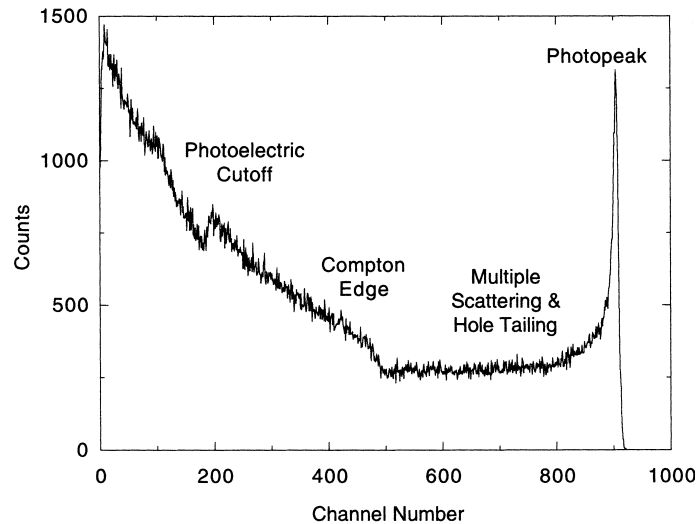


Fig. 69. Simulated pulse height spectrum for 300 keV radiation incident on a $\text{Cd}_{1-x}\text{Zn}_x\text{Te}$ detector with $(\mu\tau)_e E = 5.0$ cm, $(\mu\tau)_h E = 1.0$ mm, $d = 0.4$ cm, and $E = 1000$ V/cm [230].

detector performance. However, they reveal little about the mechanisms by which the material properties affect detector operation. In this section simple models are discussed to calculate pulse height spectra in the presence of material non-uniformities. The simplest mechanism by which composition variation affects detector performance is through the electron–hole pair production energy, ε , which equals approximately 3.1 times the bandgap for zincblende compounds [193]. The bandgap, in turn, varies quadratically with zinc fraction, x . Hence, any spatial variation in x leads inevitably to a variation in the number of electron–hole pairs generated by photons of a given energy, which degrades the detector’s energy resolution. Non-uniformity in the electron and hole drift lengths, $(\mu\tau)_e E$ and $(\mu\tau)_h E$, will also degrade the detector performance. Because the mobility, lifetime and electric field appear as a product, it is generally not possible to separate the effects of the three parameters. Detailed Monte Carlo simulations of pulse height spectra for $\text{Cd}_{1-x}\text{Zn}_x\text{Te}$ detectors have been carried out [198]. Toney et al. [230] having incorporated material non-uniformity effects. A representative simulation for 300 keV photons is shown in Fig. 69.

5.4.1. Zinc segregation along the growth axis

Since boules are often cut longitudinally into thin slices before being diced into detectors, a portion of the composition gradient along the boule appears across the face of the detector. Since this gradient becomes steeper as one approaches the heel (last to freeze) end of the boule, detectors that are cut from near the heel have a substantial, unavoidable non-uniformity in the Zn composition. Fig. 70 shows simulated spectra for 300 keV radiation for detectors cut from various positions along the growth axis and compares them with a completely uniform detector. It is clear that the energy resolution of the detector from the tip (first to freeze) is nearly the same as for the uniform detector, while the resolution of the detector from the heel is significantly poorer. The variation in energy resolution along the growth axis is greatest in the middle energy range; at lower energies the statistical fluctuations are dominant, while at higher energies hole tailing becomes more important. At 300 keV the composition gradient broadens the photopeak by as much as 1%. This effect is rather small, but still significant compared to the statistical limit. Furthermore, the effect is more pronounced for larger area detectors.

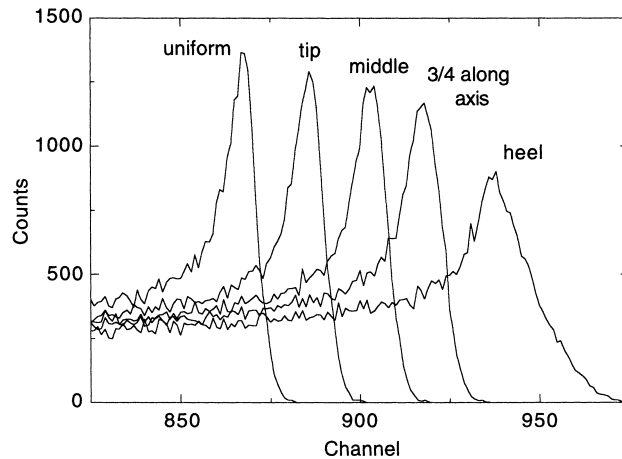


Fig. 70. Simulated photopeaks for 300 keV radiation incident on a 1 cm wide detector taken from various positions along the growth axis: $(\mu\tau)_e E = 5.0$ cm; $(\mu\tau)_h E = 1.0$ mm; $d = 0.5$ cm [230].

The effect of the composition gradient can be largely eliminated in principle by slicing the crystal perpendicular to the growth axis rather than parallel. However, one then runs the risk of shorting out the electrodes through the pipe defects which run along the growth axis [82]. Fig. 71 shows simulated spectra for 300 keV radiation for detectors from various positions along the growth axis, but with the detector axis parallel to the growth axis. The improvement over the spectra in Fig. 70 has three origins. First, since the thickness of the detector typically is not as great as the width, a detector with this orientation spans a smaller fraction of the boule length than the previous geometry. This advantage does not apply to cube-shaped detectors, however. Second, because of the exponentially decreasing probability distribution for the interaction depth, the incident radiation samples the composition gradient less strongly in this orientation. This effect is weak for higher-energy gamma rays, which illuminate the detector almost uniformly throughout its volume. Lastly, there is a small compensation effect, in which the variation in the average number of electron–hole pairs created at different positions along the growth axis tends to counteract the hole tailing in a

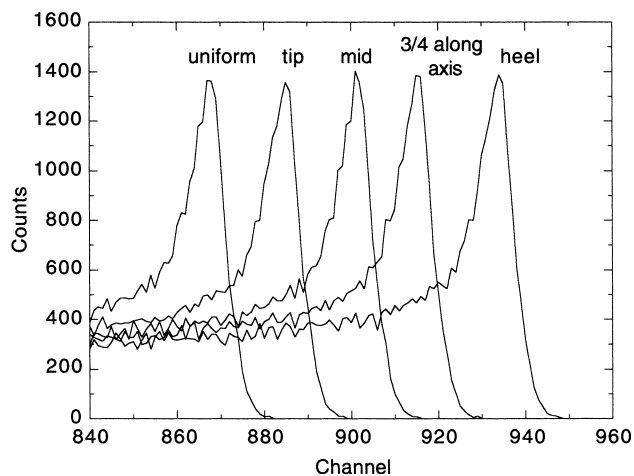


Fig. 71. Simulated photopeaks for 1 cm wide detector taken from various positions along the growth axis, with the detector axis parallel to the growth axis [230].

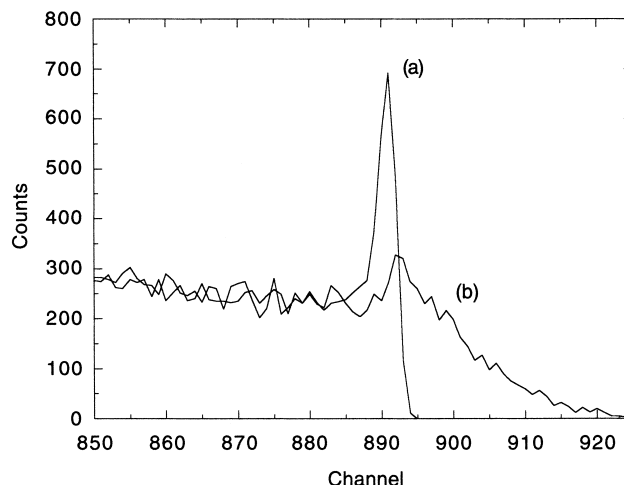


Fig. 72. Simulated photopeaks for 1 MeV radiation incident on a 1 cm wide detector taken from near the heel with detector axis (a) parallel and (b) perpendicular to the growth axis [230].

small region near the photopeak. This last effect is subtle but does make a substantial difference. Fig. 72 shows simulated spectra for 1 MeV radiation using a $1\text{ cm} \times 1\text{ cm}$ detector from the heel of the boule, in each of the two orientations. Since in this case the detector width and thickness are equal, and the penetration depth of the radiation is much greater than the detector thickness, the great difference between the two spectra can only be due to a charge generation versus charge collection compensation effect.

These simulations predict that a substantial improvement in energy resolution may be obtained by orienting the detector axis parallel to the growth axis. Experimental verification of this has been carried out which has demonstrated an average improvement of 25% in the peak-to-valley ratio for the 122 keV line of ^{57}Co for radially sliced detectors compared to axially sliced detectors [4]. Representative spectra for axially and radially sliced detectors are shown in Fig. 73. The fact that

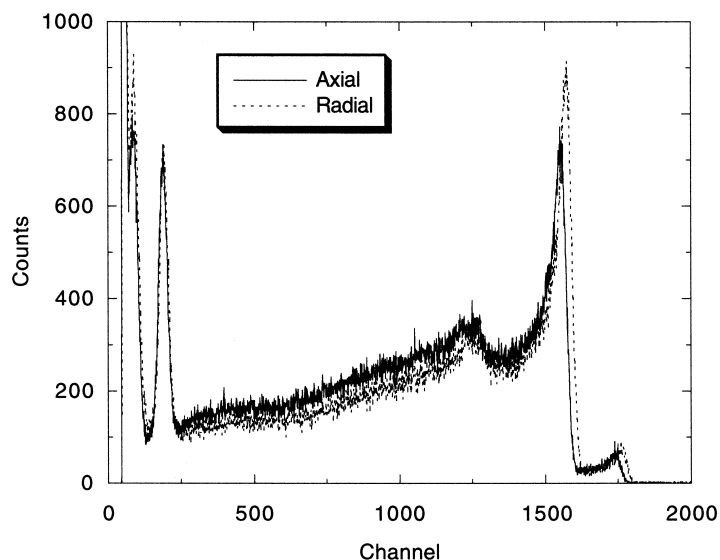


Fig. 73. ^{57}Co pulse height spectra for 2 mm thick $\text{Cd}_{1-x}\text{Zn}_x\text{Te}$ detectors sliced axially (growth axis perpendicular to detector axis) and radially (growth axis parallel to detector axis) [41].

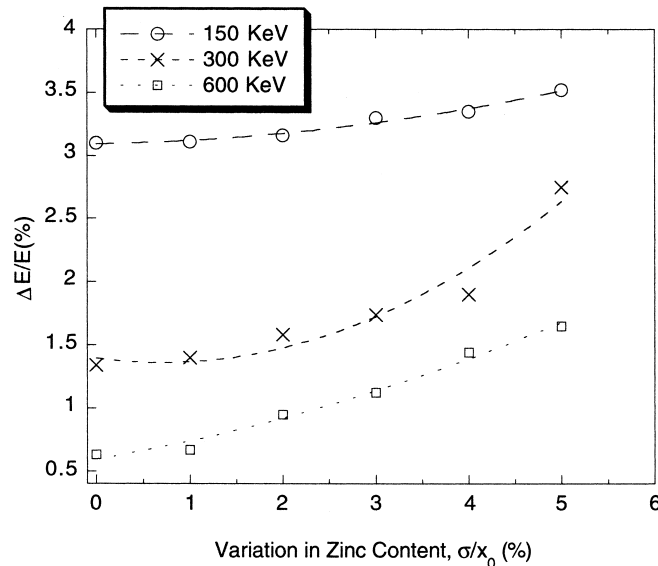


Fig. 74. Photopeak broadening due to random zinc variation [230].

there is a significant dependence of detector performance on axis orientation at such low energies indicates that the problem of uniformity along the growth axis is even worse than predicted by the simple models of the previous section.

5.4.2. Composition fluctuations and impurity segregation

In addition to the systematic decrease in zinc content along the growth axis, impurity segregation has also been observed. Energy resolution versus σ/x_0 for 300 keV radiation is shown in Fig. 74. At $\sigma/x_0 = 5\%$, which is near the upper limit of the observed variation, the non-uniformity broadens the photopeak by about 1%. If one assumes that impurity segregation produces a systematic variation in carrier lifetime, due to the presence of a dominant lifetime controlling trap, one obtains progressively worse energy resolution as one approaches the heel of the boule, as shown in Fig. 75(a).

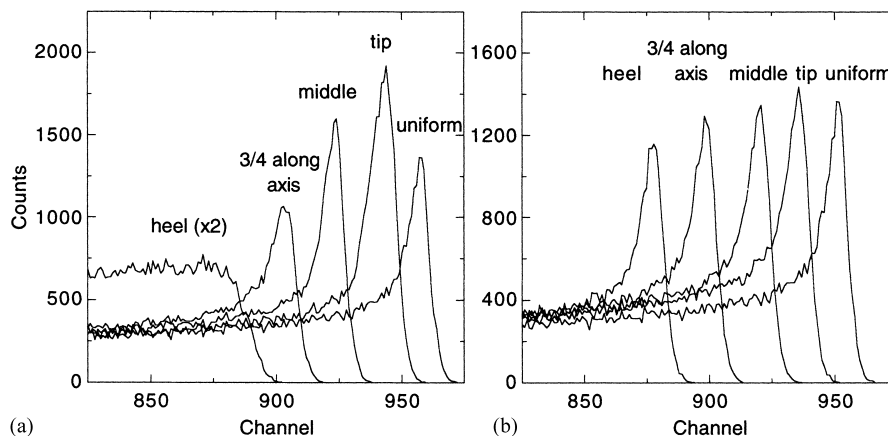


Fig. 75. Simulated photopeak for 300 keV radiation at various positions along the boule axis assuming that the electron and hole lifetimes are limited by an impurity with a segregation coefficient of 0.75, with (a) detector axis perpendicular to growth axis and (b) detector axis parallel to growth axis [230].

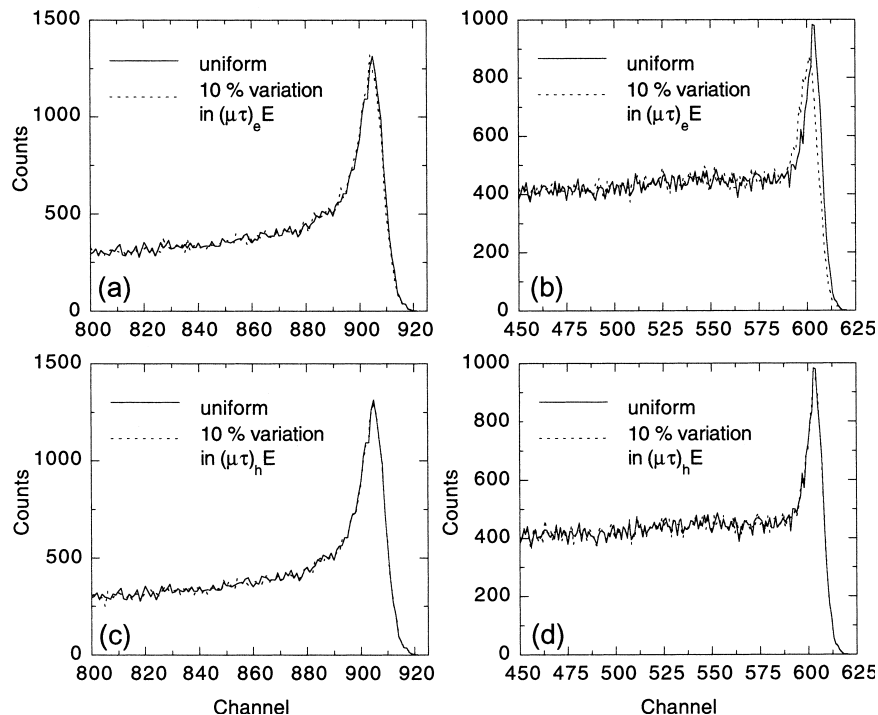


Fig. 76. Simulated photopeaks for 300 keV radiation in the presence of random variations in electron or hole drift lengths. For (a) and (c) $((\mu\tau)_e E)_{\text{nom}} = 5.0$ cm and for (b) and (d) $((\mu\tau)_e E)_{\text{nom}} = 1.0$ cm [230].

Also as with zinc segregation, the problem can be reduced by orienting the detector axis parallel to the growth axis, as in Fig. 75.

5.4.3. Random variation in drift lengths

It has been observed by α -particle mapping experiments that there are local variations in $\mu\tau E$ products that do not correspond to systematic segregation of an impurity along the growth axis [81]. Fig. 76(a) shows that if the electron transport is good $((\mu\tau)_e E \gg d)$ then even a relatively large variation of 10% in the electron drift length has no observable effect on energy resolution. If, however, the electron transport is poor $((\mu\tau)_e E \ll d)$ as in Fig. 76(b), then there is a noticeable degradation of energy resolution with a 10% variation in $(\mu\tau)_e E$. These conclusions also apply to the case of fluctuations in the electric field, as have been reported based on electro-optical measurements [231]. On the other hand, random variations in the hole transport are unimportant. Fig. 76(c) and (d) show that a 10% random variation in $(\mu\tau)_h E$ has no observable effect.

The total contribution to broadening of the photopeak due to these uniformity effects can be as much as 2%. This broadening is certainly significant, given that the pulse processing techniques and electron-only devices can produce an energy resolution of about 2% at 662 keV for good quality, 1 cm-thick detectors. Indeed these uniformity effects may help to explain why the electron-only devices sometimes achieve 2% resolution and sometimes only 3–5%. On the other hand, the gradual variations discussed here are inadequate to explain the strong experimental correlation between uniformity and detector performance. One must, therefore, consider structural defects and inclusions which can introduce much stronger variations in the transport properties.

In room temperature PL composition maps alternating bands of higher and lower zinc composition, as well as compositional discontinuities have been observed. Each of these effects

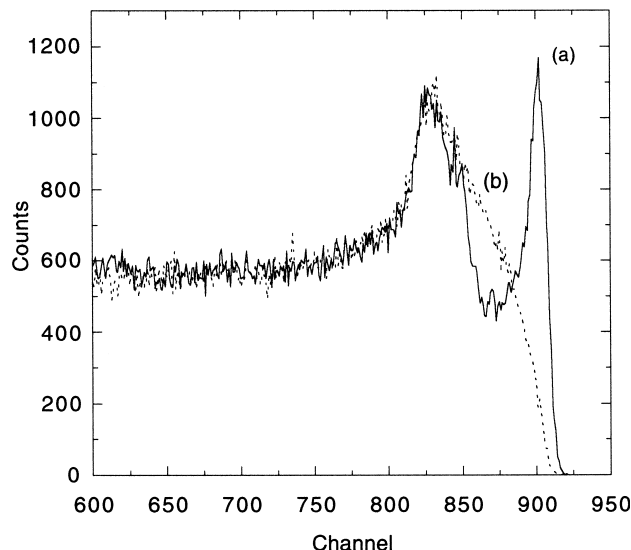


Fig. 77. Simulated photopeak in the presence of strong trapping at a grain boundary, which runs diagonally across (a) part or (b) all of the detector [230].

could lead, in principle, to a double photopeak in the pulse height spectrum though in reality it is more likely that noise would cause them to blend together producing a greatly broadened photopeak.

Another effect which has been considered is strong trapping at a grain boundary, as reported by Luke and Eissler [228]. The result of simulating this is shown in Fig. 77. If the grain boundary is taken to span the entire detector, the degradation of the spectrum is extreme, with the photopeak being completely replaced by a broad hump. If the grain boundary spans only part of the detector, the effect is relatively minor, with a hump appearing below the photopeak.

6. Radiation damage

CZT, like other wide bandgap semiconductor detector materials and the common cryogenic semiconductor detector materials is susceptible to radiation damage. While a complete understanding of radiation damage effects in CZT is not yet available, important features of the phenomenon are emerging. Radiation damage in semiconductor detectors is manifest as degradation of spectral resolution, normally specified in terms of the full width of a monochromatic peak at the half intensity point (FWHM), shifts in peak position, and changes in the device leakage current. In the case of neutron exposures, activation of the constituent elements may occur resulting in the registration of gamma ray peaks from the device itself. The latter are particularly troublesome if the activated constituents are among those being sought. Most of the radiation damage information to date on CZT has evolved from interest in applying the material to astrophysics and space applications, where exposure to heavy charged particles and neutrons is expected. Radiation effects data are typically obtained by measuring pulse height spectra (and other device characteristics) from either a photon or α -particle source before and after exposure. Factors affecting the radiation response include fluence, flux, particle energy, bias conditions, and device temperature.

Radiation damage studies on CZT have been carried out with protons (1.3 and 200 MeV), neutrons (moderated fission spectrum), and α -particles (5 MeV). The results are summarized in Table 8.

Table 8
Summary of radiation damage data on cadmium zinc telluride

Radiation energy	Fluence level	Effects
Proton — 200 meV	$5 \times 10^9 \text{ p/cm}^2$	Downward peak shift \propto fluence Two-fold increase in FWHM (one device) >25% gain shift (strip detector) Small FWHM increase in biased (planar) >45% FWHM increase in unbiased planar Gain shifts biased and unbiased
Proton — 1.3 meV	10^{10} p/cm^2	Increased interstrip leakage (strip detector)
	10^{12} p/cm^2	Increased bulk leakage
Neutron — moderated fission spectrum	10^{10} n/cm^2	No change in FWHM activation
	10^{11} n/cm^2	Significant increase in FWHM
Alpha — 5 meV	$1.5 \times 10^{10} \alpha/\text{cm}^2$	60% FWHM increase linear decrease in peak position

Although of importance, neither bias conditions nor device temperature during exposure are generally available. We note also that the data are from a very small sampling, and frequently the conclusions are based on a single device.

Considerable work has been reported in the region of 200 meV. In one study [232] 2 and 3 mm thick planar detectors were irradiated with up to $5 \times 10^9 \text{ p/cm}^2$ and resolution degradation was found in the thicker device. The initial unirradiated FWHM values at 59.6 and 122 keV of 3.2 and 3.9 keV, respectively, degraded to 4.1 and 4.3 keV after 10^9 p/cm^2 and to 6.2 and 9.2 keV after $5 \times 10^9 \text{ p/cm}^2$. The 2 mm device showed no degradation at either energy after like exposures, however. A downward shift in peak channel with increasing fluence was found for both the thick and thin detectors. The degradation in energy resolution was attributed to radiation induced electron trapping.

In a similar study [233] both strip and planar detectors were exposed to 200 meV protons. The strip detectors ($15 \text{ mm} \times 15 \text{ mm} \times 2 \text{ mm}$) were exposed under bias to fluences from 10^8 to $5 \times 10^9 \text{ p/cm}^2$. A small gain shift (3%) was noted after a fluence of $1 \times 10^9 \text{ p/cm}^2$ and a significant shift (>25%) after $5 \times 10^9 \text{ p/cm}^2$. No consistent pattern of resolution degradation was found. The resolution of one detector exposed to 5×10^9 was unchanged at 59.6 keV but significantly degraded at 122 keV while small losses (gains) were found at 1×10^8 and $1 \times 10^9 \text{ p/cm}^2$. In this study the outputs of the three strips in each detector were summed; one detector was used for each fluence level ($1, 10$ and $50 \times 10^8 \text{ p/cm}^2$). Two planar devices ($10 \text{ mm} \times 10 \text{ mm} \times 2 \text{ mm}$ and $15 \text{ mm} \times 15 \text{ mm} \times 2 \text{ mm}$) were exposed to a fluence of $5 \times 10^9 \text{ p/cm}^2$; one under bias and the other unbiased. Gain shifts and energy resolution were measured at photon energies of 14.4, 17.8, 59.6 and 122 keV. Gain shifts were found at all energies for both biased and unbiased detectors. Significant (>45%) resolution losses were found at 59.6 and 122 keV in the unbiased device. Minor changes (both positive and negative) were found in the biased case.

Also reported was a study of a single $10 \text{ mm} \times 10 \text{ mm} \times 2 \text{ mm}$ strip detector exposed to 1.3 meV protons. The bulk leakage current was found to increase significantly after 10^{12} p/cm^2 [233]. The interstrip leakage current increased significantly after about 10^{10} p/cm^2 .

Neutron irradiation results with a moderated fission spectrum source (Cf-252) at fluences up to 10^{11} n/cm^2 have been reported on a single detector [234]. The detector ($10 \text{ mm} \times 10 \text{ mm} \times 2 \text{ mm}$) was biased during exposure. No resolution degradation was found in photon peaks at 14.4, 26.3 59.6, and 122 keV for fluences up to 10^{10} n/cm^2 . Significant resolution losses were found after $7 \times 10^{10} \text{ n/cm}^2$, however. It is worth noting that resolution losses were largely recovered after 12 weeks of annealing at room temperature. Evidence of neutron activation, in the form of gamma-ray lines from cadmium and tellurium isotopes, was apparent at fluences beyond about 10^{10} n/cm^2 .

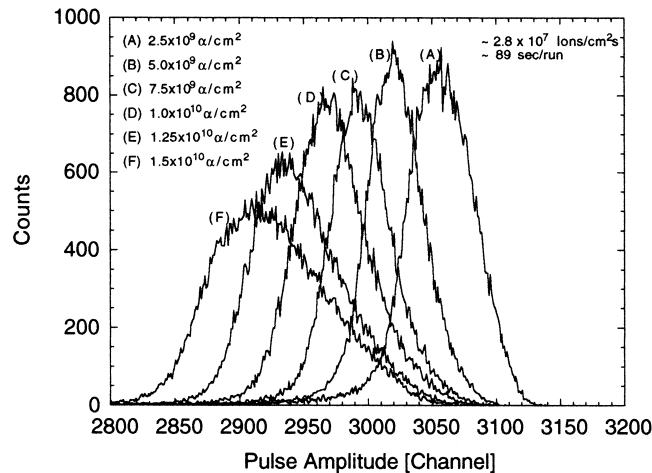


Fig. 78. Spectra of 5 MeV α -peak obtained with 3 mm \times 3 mm \times 2 mm CZT detector at various fluence levels. The α -particle flux was maintained at $2.8 \times 10^7 \alpha/\text{cm}^2 \text{ s}$ [235].

The effects of 5 MeV α -particles have been investigated using a single 3 mm \times 3 mm \times 2 mm CZT device [235]. The exposure was made in vacuum over the fluence region of 2.5×10^9 to $1.5 \times 10^{10} \alpha/\text{cm}^2$ with the flux maintained at $2.8 \times 10^7 \alpha/\text{cm}^2 \text{ s}$. The α -particle spectra obtained by integrating the pulses from a small irradiated area are shown in Fig. 78. Plots of the resultant FWHM and the position of the α -peak are shown in Fig. 79. The data of Fig. 79 show a near linear decrease in the peak position with fluence for fluences exceeding a threshold value. The FWHM, after decreasing initially, increases by more than 60% after an exposure of $1.5 \times 10^{10} \alpha/\text{cm}^2$.

In summary, we note that while a full understanding of radiation damage in CZT is lacking, the material clearly is susceptible to radiation. The thresholds for damage, at least in terms of the type of radiation and the flux levels studied, are reasonably high compared to certain configurations of cryogenically cooled germanium, however. No radiation-annealing procedures have been reported, although the prospects for thermal annealing appear favorable based on room temperature studies.

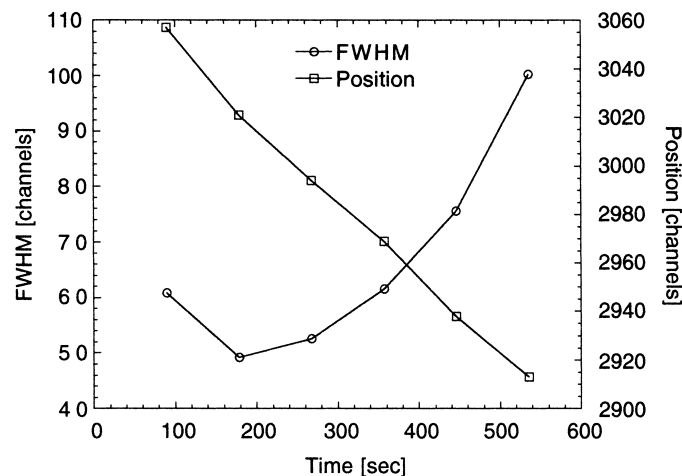


Fig. 79. Peak channel and FWHM as a function of exposure time. Exposure fluxes correspond to the levels of Fig. 78 [235].

7. Conclusions

We have reviewed the material properties of cadmium zinc telluride with Zn content in the range of 10–20%. The yield of material suitable for this application remains relatively low, and this continues to limit to some extent the applications of this technology due to the associated high material costs. The development of additional growth techniques, further improvements in the yield, and hence reduction in detector cost, will aid this technology. Some of this has occurred with the introduction of some low pressure Bridgman grown material, which appears to be suitable for use in certain applications and significant improvements in yield have also been seen in high pressure Bridgman grown material. Many of the defects that were initially common in this material have been either reduced or essentially eliminated. A complete understanding of the microscopic defects and the mechanisms that account for the Fermi-level pinning in CZT is not yet available, and this has contributed to the issues of yield and uniformity. Mapping techniques, which have been developed to reveal the spatial distribution of material properties have proven to be invaluable in elucidating regions of high-quality material and helping to develop correlations between material properties and growth techniques. Contacts, too, continue to be of concern though it has become more apparent that the choice of material (and the contact geometry) are far more important than the deposition method employed.

A great deal has been learned about this material in a relatively short time and this has contributed significantly to the advancement in the state-of-the-art of room temperature CZT nuclear detectors and spectrometers. Commercial systems for various applications have either been demonstrated or are now entering the marketplace, and it appears that this technology is poised to make significant inroads in various areas, most notably medical and national-security systems.

References

- [1] W.E. Burcham, *Nuclear Physics: An Introduction*, Longmans, London, 1963.
- [2] A. Rose, *Concepts in Photoconductivity and Allied Problems*, Wiley, New York, 1963.
- [3] T.E. Schlesinger, R.B. James (Eds.), *Semiconductors for Room Temperature Nuclear Applications*, Vol. 43, Academic Press, New York, 1995, Chapter 9, p. 335.
- [4] C. Szeles, E.E. Eissler, *MRS Symp. Proc.* 487 (1998) 3.
- [5] K. Lynn, M. Weber, H. Glass, J. Flint, C. Szeles, *Mater. Res. Soc. Symp.* 487 (1998) 229.
- [6] K. Chattopadhyay, H. Chen, K.-T. Chen, A. Burger, J.P. Flint, H.L. Glass, R.B. James, *Mater. Res. Soc. Proc.* 487 (1998) 123.
- [7] T.E. Schlesinger, B. Brunett, H. Yao, J. Van Scyoc, R.B. James, S. Egarievwe, K. Chattopadhyay, X. Ma, A. Burger, N. Giles, U. El-Hanany, A. Shahar, A. Tsigelman, *J. Electron. Mater.* 28 (1999) 864.
- [8] R.B. James, A. Burger, H. Hermon, E. Cross, W. Yao, G. Wright, M. Schieber, 2000, unpublished.
- [9] P.N. Luke, *Appl. Phys. Lett.* 65 (1994) 2884.
- [10] P.N. Luke, *IEEE Trans. Nucl. Sci.* 42 (1995) 207.
- [11] J.C. Lund, J.M. VanScyoc, R.B. James, D.S. Mc Gregor, R.W. Olsen, *Nucl. Instrum. Methods A* 380 (1996) 256.
- [12] Z. He, G.F. Knoll, D.K. Wehe, R. Rojeski, C.H. Mastrangelo, M. Hammig, C. Barrett, A. Uriani, *Nucl. Instrum. Methods A* 380 (1996) 228.
- [13] E.Y. Lee, J.C. Lund, N.R. Hilton, B.A. Brunett, R.B. James, *Mater. Res. Soc. Proc.* 487 (1998) 537.
- [14] J.D. Eskin, H.H. Barrett, H.B. Barber, *J. Appl. Phys.* 85 (1999) 647.
- [15] M. Amman, P.N. Luke, *Proc. SPIE* 3115 (1997) 205.
- [16] K. Zanio, Willardson, Beer, Teatise (Eds.), *Cadmium Telluride, Semiconductors and Semimetals*, Vol. 13, Academic Press, San Diego, 1978, p. 53.
- [17] J.E. Toney, B.A. Brunett, T.E. Schlesinger, J.M. Van Scyoc, R.B. James, M. Schieber, M. Goorsky, H. Yoon, E. Eissler, C. Johnson, *Nucl. Instrum. Methods A* 380 (1996) 132.
- [18] N. Motta, A. Balzarotti, P. Letardi, A. Kisiel, M.T. Czyzyk, M. Zimnal-Starnawska, M. Podgorny, *J. Cryst. Growth* 72 (1985) 205.

- [19] M.S. Goorsky, H. Yoon, M. Schieber, R.B. James, D.S. McGregor, M. Natarajan, Nucl. Instrum. Methods A 3806 (1996) 6.
- [20] P. Yu, M. Cardona, Fundamentals of Semiconductors, Vol. 102, Springer, Berlin, 1996.
- [21] P. Plumelle, M. Vandevyver, Phys. Stat. Sol. (b) 73 (1976) 271.
- [22] K. Kunc, Ann. Phys. (France) 5 (1973/1974) 319.
- [23] J.M. Rowe, R.M. Nicklow, D.L. Price, K. Zanio, Phys. Rev. B 10 (1974) 671.
- [24] N. Vagelatos, D. Wehe, J.S. King, J. Chem. Phys. 60 (1974) 3613.
- [25] S. Perkowitz, L.S. Kim, Z.C. Feng, P. Becla, Phys. Rev. B 42 (1990) 1455.
- [26] N. Peyghambarian, S.W. Koch, A. Mysyrowicz, Introduction to Semiconductor Optics, Prentice-Hall, Englewood Cliffs, 1993.
- [27] M.L. Cohen, J.R. Chelikowsky, Electronic Structure and Optical Properties of Semiconductors, Springer, New York, 1988.
- [28] B.K. Ridley, Quantum Processes in Semiconductors, Oxford University Press, New York, 1982.
- [29] V. Swaminathan, A.T. Macrander, Materials Aspects of GaAs and InP Based Structures, Prentice-Hall, Englewood Cliffs, 1991.
- [30] D. Kanzer, J. Phys. C: Solid State Phys. 6 (1973) 2967.
- [31] J. Singh, Physics of Semiconductors and their Heterostructures, McGraw-Hill, New York, 1993.
- [32] J.A. Van Vechten, T.K. Bergstresser, Phys. Rev. B 1 (1970) 3351.
- [33] K. Shim, D.N. Talwar, H.J. Moh, Solid State Commun. 97 (1996) 315.
- [34] T.-C. Yu, R.F. Brebrick, J. Phase Equilibria 13 (1992) 476.
- [35] J. Steininger, A.J. Strauss, R.F. Brebrick, J. Electrochem. Soc. 117 (1970) 1305.
- [36] R. Triboulet, G. Neu, B. Fotouhi, J. Cryst. Growth 65 (1983) 263.
- [37] P. Cheuvart, U. El-Hanani, D. Schneider, R. Triboulet, J. Cryst. Growth 101 (1990) 270.
- [38] M. Bruder, H. Schwarz, R. Schmitt, H. Maier, J. Cryst. Growth 101 (1990) 266.
- [39] R. Lauer, F. Williams, J. Appl. Phys. 42 (1971) 2904.
- [40] E. Raitskin, J. Butler, IEEE Trans. Nucl. Sci. 35 (1988) 81.
- [41] J.F. Butler, F.P. Doty, C. Lingren, Proc. SPIE — Int. Soc. Opt. Eng. 1734 (1992) 131.
- [42] F.P. Doty, J.F. Butler, J.F. Schetzina, K.A. Bowers, J. Vac. Sci. Technol. B 10 (1992) 1418.
- [43] R.B. James, H.W. Yao, E.Y. Lee, G.W. Wright, R.W. Olsen, E.S. Cross, L. Li, F. Lu, V.K. Komar, D. Nalivaiko, P. Luke, M. Amman, J. Lee, T.E. Schlesinger, J. Burtalia, in: Proceedings of the Presentation at the SPIE Conference on Hard X-ray, Gamma-ray and Neutron Detector Physics II, San Diego, CA, 2000.
- [44] W. Palosz, K. Graszka, D. Gilles, G. Jerman, J. Cryst. Growth 169 (1996) 20.
- [45] A. Szczerbakow, J. Domagala, D. Rose, K. Durose, V. Ivanov, A. Omeltchouk, J. Cryst. Growth 191 (1998) 673.
- [46] L. Ben-Dor, J. Cryst. Growth 71 (1985) 519.
- [47] M. Fiederle, T. Feltgen, J. Meinhardt, M. Rogalla, K.W. Benz, J. Cryst. Growth 197 (1999) 635.
- [48] V.T. Komar, Technical Report, National Academy of Sciences of the Ukraine, Department of Optical and Constructional Crystals, Kharkov, Ukraine, 1997.
- [49] M. Muhlberg, P. Rudolph, C. Genzel, B. Wermke, U. Becker, J. Cryst. Growth 101 (1990) 275.
- [50] R.B. James, B. Brunett, J. Heffelfinger, J. Van Scyoc, J.C. Lund, F.P. Doty, C.L. Lingren, R. Olsen, E. Cross, H. Hermon, H. Yoon, N. Hilton, M. Schieber, E.Y. Lee, J. Toney, T.E. Schlesinger, M. Goorsky, W. Yao, H. Chen, A. Burger, J. Electron. Mater. 27 (1998) 788.
- [51] C. Szeles, M. Driver, SPIE Proc. 3446 (1998) 2.
- [52] A. Burger, K.-T. Chen, D. Shi, W.E. Collins, R.B. James, SPIE Proc. 3115 (1997) 70.
- [53] S.U. Egarievwe, K.T. Chen, A. Burger, R.B. James, C.M. Lisse, J. X-ray Sci. Technol. 6 (1996) 309.
- [54] H.L. Glass, A.J. Socha, D.W. Bakken, V.M. Speziale, J.P. Flint, Mater. Res. Soc. Symp. Proc. 487 (1998) 27.
- [55] S. Sen, W. Konkell, S. Tighe, L. Bland, S. Sharma, R. Taylor, J. Cryst. Growth 86 (1988) 111.
- [56] S. Sen, J. Stannard, Mater. Res. Soc. Symp. 302 (1993) 391.
- [57] G.F. Knoll, D.S. McGregor, Mater. Res. Soc. Proc. 302 (1993) 3.
- [58] R.B. James, H.W. Yao, G. Wright, R.W. Olsen, E.Y. Lee, J. Erickson, L. Xia, F. Lu, P. Luke, M. Amman, J. Lee, V.K. Komar, D. Naliviako, Y. Nemirovsky, J. Burtalia, in: Proceedings of the Presentation at the 12th American Conference on Crystal Growth and Epitaxy, Vail, CO, 2000.
- [59] H.W. Yao, R.B. James, J. Erickson, G. Wright, L. Li, F. Lu, J. Buturlia, Y. Nemirovsky, in: Proceedings of the Presentation at the SPIE Conference on Hard X-ray, Gamma-ray and Neutron Detector Physics, San Diego, CA, 2000.
- [60] Y. Nemirovsky, A. Peyser, J. Gurelik, R.B. James, H.W. Yao, L.X. Li, F. Lu, 2000, unpublished.
- [61] Cirignano K.S. Shah, P. Bennett, L. Li, F. Lu, J. Buturlia, H.W. Yao, G. Wright, R.B. James, in: R.B. James, R.C. Schirato (Eds.), Hard X-ray, Gamma-ray and Neutron Detector Physics II, Vol. 4141, SPIE, Bellingham, WA, 2000, pp. 23–28.
- [62] H. Scholz, Acta Electron. 17 (1974) 69.
- [63] M. Schieber, W. Schneppe, L. van den Berg, J. Cryst. Growth 33 (1976) 125.
- [64] L. van den Berg, Mater. Res. Soc. Symp. 302 (1993) 73.

- [65] J. Boone, G. Cantwell, W. Harsch, J. Thomas, B. Foreman, *J. Cryst. Growth* 139 (1994) 27.
- [66] M. Laasch, R. Schwartz, W. Joerger, C. Eiche, M. Fiederle, K. Benz, K. Grasz, *J. Cryst. Growth* 146 (1995) 125.
- [67] Y. Bailing, M. Isshiki, Z. Chuanping, H. Ximin, Y. Xiling, *J. Cryst. Growth* 147 (1995) 399.
- [68] K. Grasz, U. Zuzga-Grasz, A. Jedrzejczak, R. Galazka, J. Maajewski, A. Szadkowski, E. Grodzicka, *J. Cryst. Growth* 123 (1992) 519.
- [69] H. Wiedemeier, G. Wu, *J. Electron. Mater.* 24 (1995) 1007.
- [70] W. Palosz, S. Lehoczky, F. Szofran, *J. Cryst. Growth* 148 (1995) 49.
- [71] W. Palosz, F. Szofran, S. Lehoczky, *J. Cryst. Growth* 148 (1995) 56.
- [72] A. Melnikov, A. Sigov, K. Vorotilov, A. Davydov, L. Topalova, *J. Cryst. Growth* 197 (1999) 666.
- [73] W. Trower, in: *Proceedings of the 5th Scientific Symposium on Room Temperature Semiconductor X-ray, Gamma-ray, and Neutron Detectors*, Sandia National Laboratories, Livermore, CA, March 1997.
- [74] W. Palosz, W. George, E. Collins, K. Chen, Y. Zhang, Z. Hu, A. Burger, *J. Cryst. Growth* 174 (1997) 733.
- [75] W. Palosz, D. Gillies, K. Grasz, H. Chung, B. Raghothamachar, M. Dudley, *J. Cryst. Growth* 182 (1997) 37.
- [76] R.S. List, J.H. Tregilgas, A.M. Turner, J.D. Beck, J.C. Ehmke, *Proc. SPIE — Int. Soc. Opt. Eng.* 2228 (1994) 274.
- [77] M. Meshkinpour, M.S. Goorsky, G. Chu, D.C. Streitt, T.R. Block, M. Wojtowicz, *Appl. Phys. Lett.* 66 (1995) 748.
- [78] C.J. Johnson, E.E. Eissler, S.E. Cameron, Y. Kong, S. Fan, S. Jovanovic, K.G. Lynn, *Mater. Res. Soc. Symp.* 302 (1993) 463.
- [79] H. Hermon, M.M. Schieber, M.S. Goorsky, T.T. Lam, E. Meerson, H.W. Yao, J. Erickson, R.B. James, in: R.B. James, R.C. Schirato (Eds.), *Hard X-ray, Gamma-ray and Neutron Detector Physics II*, Vol. 4141, SPIE, Bellingham, WA, 2000, 186–193.
- [80] K.Y. Lay, D. Nichols, S. McDevitt, B.E. Dean, C.J. Johnson, *J. Cryst. Growth* 86 (1988) 118.
- [81] H. Yoon, J.M. Van Scyoc, T.S. Gilbert, M.S. Goorsky, B.A. Brunett, J.C. Lund, H. Hermon, M. Schieber, R.B. James, *Mater. Res. Soc. Symp. Proc.* 487 (1998) 115.
- [82] C. Szeles, in: *Proceedings of the 5th Scientific Symposium on Room Temperature X-ray, Gamma-ray and Neutron Detectors*, Livermore, CA, 11–12 March 1997.
- [83] R.B. James, G. Wright, V. Komar, private communication, 2000.
- [84] J.R. Heffelfinger, D.L. Medlin, H. Yoon, H. Hermon, R.B. James, *SPIE Proc.* 3115 (1997) 40.
- [85] B.D. Cullity, *Elements of X-ray Diffraction*, 2nd Edition, Addison-Wesley, Menlo Park, CA, 1978.
- [86] H. Yoon, S.E. Lindo, M.S. Goorsky, *J. Cryst. Growth* 174 (1997) 775.
- [87] B. Jenichen, R. Köhler, W. Möhling, *J. Phys. E: Sci. Instrum.* 21 (1988) 1062.
- [88] K. Nakagawa, K. Naeda, S. Takeuchi, *Appl. Phys. Lett.* 34 (1979) 574.
- [89] A. Burger, R.B. James, Sandia National Laboratories, 2000, unpublished data.
- [90] C. Hackett, H. Hermon, E. Cross, P. Doty, E. Tarver, R.B. James, *J. Electron. Mater.* 28 (1999) 774.
- [91] F. Rosenberger, *Fundamentals of Crystal Growth*, Vol. 1, Springer, New York, 1979.
- [92] A. Tanaka, Y. Masa, S. Seto, T. Kawasaki, *J. Cryst. Growth* 94 (1989) 166.
- [93] S.K. Ghandi, *VLSI Fabrication Principles*, Wiley, New York, 1994.
- [94] M. Azoulay, S. Rotter, G. Gafni, R. Tenne, M. Roth, *J. Cryst. Growth* 3117 (1992) 276.
- [95] Y. Tao, S. Kou, *J. Cryst. Growth* 181 (1997) 301.
- [96] J.E. Toney, T.E. Schlesinger, R.B. James, *Nucl. Instrum. Methods Phys. Res. A* 428 (1999) 14.
- [97] H. Yoon, M.S. Goorsky, B.A. Brunett, J.M. VanScyoc, J.C. Lund, R.B. James, *J. Electron. Mater.* 28 (1999) 838.
- [98] K. Hjelt, M. Juvonen, T. Tuomi, S. Nenonen, E.E. Eissler, M. Bavdaz, *Phys. Stat. Sol. (a)* 162 (1997) 747.
- [99] D.J. Olego, J.P. Faurie, S. Sivananthan, P.M. Raccach, *Appl. Phys. Lett.* 47 (1985) 1172.
- [100] J.L. Reno, E.D. Jones, *Phys. Rev. B* 45 (1992) 1440.
- [101] N. Magnea, F. Dal'bo, J.L. Pautrat, A. Million, L. DiCiocco, G. Guillet, *Mater. Res. Soc. Symp. Proc.* 90 (1987) 455.
- [102] K. Oettinger, D.M. Hofmann, A.L. Efros, B.K. Meyer, M. Salk, K.W. Benz, *J. Appl. Phys.* 71 (1992) 4523.
- [103] T. Taguchi, *Phys. Stat. Sol. (a)* 77 (1983) K115.
- [104] R.G. Rhodes, *Imperfections and Active Centres in Semiconductors*, Macmillan, New York, 1964.
- [105] J. Lee, N.C. Giles, D. Rajavel, C.J. Summers, *Phys. Rev. B* 49 (1994) 1668.
- [106] C.J.L. Moore, C.J. Miner, *J. Cryst. Growth* 103 (1990) 21.
- [107] P. Rudolph, A. Engel, I. Schentke, A. Grochocki, *J. Cryst. Growth* 147 (1995) 297.
- [108] J.R. Heffelfinger, D.L. Medlin, R.B. James, *Mater. Res. Soc.* 487 (1998) 33.
- [109] L. Chibani, M. Hage-Ali, P. Siffert, *J. Cryst. Growth* 161 (1996) 153.
- [110] E.Y. Lee, R.B. James, *J. Electron. Mater.* 28 (1999) 6.
- [111] D.E. Holmes, R.T. Chen, K.R. Elliott, C.G. Kirkpatrick, *Appl. Phys. Lett.* 40 (1982) 46.
- [112] F.P. Doty, in: *Proceedings of the Presentation at the 1998 US Workshop on the Physics and Chemistry of II–VI Semiconductors*, Charleston, SC, 21–22 October 1998.
- [113] M. Hage-Ali, P. Siffert, *Semiconductors for room temperature nuclear detector applications*, in: T.E. Schlesinger, R.B. James (Eds.), *Semiconductors and Semimetals*, Vol. 43, Academic Press, New York, 1995, p. 219.
- [114] N.R. Kyle, in: P. Siffert, A. Cornet (Eds.), *Proceedings of the 1st International Symposium on CdTe: A Material for Gamma-Ray Detectors*, Centre de Recherches Nucleaires, Strasbourg, 1971.

- [115] A. Cornet, Thesis, Universite Louis Pasteur, Strasbourg, 1976.
- [116] F.V. Wald, R.O. Bell, A.A. Menna, Int. Tyco Technical Report, 1973.
- [117] P. Siffert, A. Cornet, R. Stuck, R. Triboulet, Y. Marfaing, IEEE Trans. Nucl. Sci. 22 (1975) 221.
- [118] C. Scharager, J.C. Muller, R. Stuck, P. Siffert, Phys. Stat. Sol. (a) 31 (1975) 247.
- [119] B. Biglari, M. Samimi, M. Hage-Ali, J.M. Koebel, P. Siffert, J. Cryst. Growth 89 (1988) 428.
- [120] B. Biglari, M. Samimi, M. Hage-Ali, J.M. Koebel, P. Siffert, Nucl. Instrum. Methods Phys. Res. A 283 (1989) 249.
- [121] P. Moravec, M. Hage-Ali, L. Chibani, P. Siffert, Mater. Sci. Eng. B 16 (1993) 223.
- [122] E.J. Johnson, J.A. Kafalas, R.W. Davies, J. Appl. Phys. 54 (1982) 204.
- [123] M. Fiederle, D. Ebling, C. Eiche, P. Hug, W. Joerger, M. Laasch, R. Schwarz, M. Salk, K.W. Benz, J. Cryst. Growth 146 (1995) 142.
- [124] H.I. Ralph, J. Appl. Phys. 49 (1978) 672.
- [125] M. Hage-Ali, P. Siffert, Nucl. Instrum. Methods A322 (1992) 313.
- [126] J. Shen, D.K. Aidun, L. Regel, W.R. Wilcox, Mater. Sci. Eng. B 16 (1993) 182.
- [127] T.J. Magee, J. Peng, J. Bean, Phys. Stat. Sol. (a) 27 (1975) 557.
- [128] F.A. Selim, V. Swaminathan, F.A. Kroger, Phys. Stat. Sol. (a) 29 (1975) 465.
- [129] R.H.J. Bube, Chem. Phys. 23 (1955) 18.
- [130] D.C. Look, Z.-Q. Fang, J.W. Hemsky, P. Kengkan, Phys. Rev. B 55 (1997) 2214.
- [131] B. Santic, U.V. Desnica, Appl. Phys. Lett. 56 (1990) 2636.
- [132] D.V. Lang, J. Appl. Phys. 45 (1974) 3023.
- [133] P.M. Mooney, J. Appl. Phys. 54 (1983) 208.
- [134] C. Eiche, D. Maier, M. Schneider, D. Sinerius, J. Weese, K.W. Benz, J. Honerkamp, J. Phys. Condens. Matter 4 (1992) 6131.
- [135] M. Fiederle, D. Ebling, C. Eiche, D.M. Hofmann, M. Salk, W. Stadler, K.W. Benz, B.K. Meyer, J. Cryst. Growth 138 (1994) 529.
- [136] J.E. Toney, B.A. Brunett, T.E. Schlesinger, E. Cross, F.P. Doty, R.B. James, Mater. Res. Soc. Symp. Proc. 487 (1998) 59.
- [137] Zerrai, M. Dammark, G. Bremond, in: Proceedings of the Semiconducting and Semi-Insulating Materials Conference, IEEE, 1996.
- [138] X.J. Bao, T.E. Schlesinger, R.B. James, R.H. Stulen, C. Ortale, L. van den Berg, J. Appl. Phys. 67 (1990) 7265.
- [139] X.J. Bao, T.E. Schlesinger, R.B. James, G.L. Gentry, A.Y. Cheng, C. Ortale, J. Appl. Phys. 69 (1997) 4247.
- [140] L. Chibani, M. Hage-Ali, J.P. Stoquert, J.M. Koebel, P. Siffert, Mater. Sci. Eng. B16 (1993) 202.
- [141] P. Fougères, M. Hage-Ali, J.M. Koebel, P. Siffert, S. Hassan, Al. Lussan, R. Triboulet, G. Marrkchi, A. Zerrai, K. Cherkaoui, R. Adhiri, G. Bremond, O. Kaitasov, M.O. Rualult, J. Cretou, J. Cryst. Growth 184/185 (1998) 1313.
- [142] E.Y. Lee, B.A. Brunett, R.W. Olsen, J.M. Van Scyoc III, H. Hermon, R.B. James, SPIE Proc. 3446 (1998) 40.
- [143] E.Y. Lee, Solid State Commun. 112 (1999) 31.
- [144] E.Y. Lee, R.B. James, R.W. Olsen, H. Hermon, J. Electron. Mater. 28 (1999) 766.
- [145] Z.C. Huang, E. Eissler, C.R. Wie, Nucl. Instrum. Methods B100 (1995) 507.
- [146] C. Szeles, Y.Y. Shan, K.G. Lynn, E.E. Eissler, Nucl. Instrum. Methods A 380 (1996) 148.
- [147] C. Szeles, Y.Y. Shan, K.G. Lynn, A.R. Moodenbaugh, E.E. Eissler, Phys. Rev. B 55 (1997) 6945.
- [148] G.F. Neumark, J. Appl. Phys. 51 (1980) 3383.
- [149] E. Molva, J.L. Pautrat, K. Saminadayar, G. Milchberg, N. Magneat, Phys. Rev. B 30 (1984) 3344.
- [150] E.M. Pell, J. Appl. Phys. 31 (1960) 291.
- [151] J.W. Mayer, J. Appl. Phys. 33 (1962) 2894.
- [152] R.M. Bilbe, J.E. Nicholls, J.J. Davies, Phys. Stat. Sol. (b) 121 (1984) 339.
- [153] E. Weigel, G. Muller-Vogt, J. Cryst. Growth 161 (1996) 40.
- [154] D.V. Lang, Phys. Rev. B 19 (1979) 1015.
- [155] D.V. Lang, in: S.T. Pantelides (Ed.), Deep Centers in Semiconductors, Gordon and Breach, New York, 1986 (Chapter 7).
- [156] C.H. Park, D.J. Chadi, Phys. Rev. B 52 (1995) 11884.
- [157] K. Khachatryan, M. Kaminska, E.R. Weber, B. Becla, R.A. Street, Phys. Rev. B 40 (1989) 6304.
- [158] C. Burkey, R.P. Khosla, J.R. Fischer, D.L. Losee, J. Appl. Phys. 47 (1976) 1095.
- [159] S.B. Quadri, E.F. Skelton, A.W. Webb, J. Kennedy, Appl. Phys. Lett. 46 (1985) 257.
- [160] S.B. Quadri, E.F. Skelton, A.W. Webb, J. Kennedy, Physica 139 (1986) 341.
- [161] H. Landolt, R. Börnstein, Numerical Data and Functional Relationships in Science and Technology, Vol. III/17b, Springer, New York, 1987.
- [162] L. Scherbak, P. Feichouk, P. Fochouk, O. Panchouk, J. Cryst. Growth 161 (1996) 219.
- [163] F. Bissani, S. Tatarenko, K. Saminadayar, N. Magnea, R.T. Cox, A. Tardot, C. Grattapain, J. Appl. Phys. 72 (1992) 2927.
- [164] B.K. Meyer, P. Omling, E. Weigel, G. Muller-Vogt, Phys. Rev. B 46 (1992) 15135.
- [165] C. Gely-Sykes, C. Corbel, R. Triboulet, Solid State Commun. 80 (1991) 79.
- [166] C. Corbel, L. Baroux, F.M. Kiessling, C. Gely-Sykes, R. Triboulet, Mater. Sci. Eng. B 16 (1993) 134.

- [167] R. Krause-Rehberg, H.S. Leipner, T. Abgarjan, A. Polity, Appl. Phys. A 66 (1998) 599.
- [168] D.M. Hofmann, P. Omling, H.G. Grimmeiss, B.K. Meyer, K.W. Benz, D. Sinerius, Phys. Rev. B 45 (1992) 6247.
- [169] Kh. Allachen, M. Tapiero, Z. Guellil, J.P. Zielinger, J.C. Launay, J. Cryst. Growth 184/185 (1998) 1142.
- [170] W. Stadler, D.M. Hofmann, B.K. Meyer, R. Krause-Rehberg, A. Polity, Th. Abgarjan, M. Salk, K.W. Benz, M. Azoulay, Acta Phys. Pol. A 88 (1995) 921.
- [171] Y.P. Varshni, Physica 34 (1967) 34.
- [172] J. Weese, Comput. Phys. Commun. 69 (1992) 99.
- [173] P. Emanuelson, P. Omling, B.K. Meyer, M. Wienke, M. Shenk, Phys. Rev. B 47 (1993) 15578.
- [174] G. Tessaro, P. Mascher, J. Cryst. Growth 197 (1999) 581.
- [175] M.A. Berding, Appl. Phys. Lett. 74 (1999) 552.
- [176] M. Schieber, H. Hermon, J.C. Lund, A. Antolak, D. Morse, N.N. Kolesnikov, Yu.N. Ivanov, M.S. Goorsky, J.M. Van Scyoc, H. Yoon, J. Toney, T.E. Schlesinger, F.P. Doty, J.P. Cozzatti, IEEE Trans. Nucl. Sci. 44 (1997) 2566.
- [177] Y. Marfaing, Prog. Crystal Growth Characteristics 4 (1981) 317.
- [178] R.C. Sharma, Y.A. Chang, Bull. Alloy Phase Diagrams 10 (1989) 334.
- [179] Y.C. Chang, R.B. James, in: R.B. James, R.C. Sherato (Eds.), Hard X-ray, Gamma-ray and Neutron Detector Physics and Applications, Vol. 3768, SPIE, Bellingham, WA (Phys. Rev. B), 1999, p. 381.
- [180] C.H. Park, D.J. Chadi, Phys. Rev. Lett. 75 (1995) 1134.
- [181] K. Zanio, J. Electron. Mater. 3 (1974) 327.
- [182] M.G. Astles, in: P. Capper (Ed.), Properties of Narrow Gap Cadmium-Based Compounds, EMIS Data Reviews Series no. 10, INSPEC, London, 1994, p. 494.
- [183] K. Suzuki, S. Seto, S. Dairaku, N. Takojima, T. Sawada, K. Imai, J. Electron. Mater. 25 (1996) 1241.
- [184] D.L. Rode, Phys. Rev. B 2 (1970) 1012.
- [185] D. Chattopadhyay, Solid State Commun. 91 (1994) 149.
- [186] D.N. Talwar, Z.C. Feng, P. Becla, Phys. Rev. B 48 (1993) 17064.
- [187] D.L. Rode, Phys. Rev. B 2 (1970) 4036.
- [188] Z. Burshtein, H.N. Jayathirtha, A. Burger, J.F. Butler, B. Apotovsky, F.P. Doty, Appl. Phys. Lett. 63 (1993) 102.
- [189] T.M. Duc, C. Hsu, J.P. Faurie, Phys. Rev. Lett. 58 (1987) 1127.
- [190] D. Rioux, D.W. Niles, H. Hochst, J. Appl. Phys. 73 (1993) 8381.
- [191] M. Costato, C. Jacoboni, L. Reggiani, Phys. Stat. Sol. (b) 52 (1972) 461.
- [192] J.D. Wiley, Phys. Rev. B 4 (1971) 2485.
- [193] J. Toney, Ph.D. Thesis, Carnegie Mellon University, 1998.
- [194] B.A. Brunett, J.M. Van Scyoc, H. Yoon, T.S. Gilbert, T.E. Schlesinger, J.C. Lund, R.B. James, MRS Symp. Proc. 487 (1998) 39.
- [195] M. Jung, J. Morel, P. Fougeres, M. Hage-Ali, P. Siffert, Nucl. Instrum. Methods A 428 (1999) 45.
- [196] M. Martini, T.A. McMath, Nucl. Instrum. Methods 79 (1970) 259.
- [197] H.W. Yao, R.J. Anderson, R.B. James, R.W. Olsen, Mater. Res. Soc. Symp. Proc. 487 (1998) 51.
- [198] T.H. Prettyman, Nucl. Instrum. Methods Phys. Res. A 428 (1999) 72.
- [199] T.H. Prettyman, Nucl. Instrum. Methods Phys. Res. A 422 (1999) 232.
- [200] E.Y. Lee, R.B. James, Nucl. Instrum. Methods Phys. Res. A 428 (1999) 66.
- [201] C. Manfredotti, F. Fizzotti, C. Ongaro, E. Vittone, U. Nastasi, Mater. Res. Soc. Symp. Proc. 302 (1993) 183.
- [202] C. Manfredotti, F. Fizzotti, F. Polesello, E. Vittone, Nucl. Instrum. Methods Phys. Res. A 380 (1996) 145.
- [203] E. Vittone, F. Fizzotti, A. Giudice, P. Polesello, C. Manfredotti, Nucl. Instrum. Methods Phys. Res. A 428 (1999) 81.
- [204] H. Chen, J. Tong, Z. Hu, D.T. Shi, G.H. Wu, K.-T. Chen, M.A. George, W.E. Collins, A. Burger, R.B. James, C.M. Stahle, M. Bartlett, J. Appl. Phys. 80 (1996) 3599.
- [205] T.W. Chan, X.J. Bao, I.H. Oh, P.J. Sides, E.I. Ko, MRS Symp. Proc. 259 (1992) 275.
- [206] A. Burger, H. Chen, J. Tong, D. Shi, M.A. George, K.-T. Chen, W.E. Collins, R.B. James, C.M. Stahle, L.M. Bartlett, IEEE Trans. Nucl. Sci. 44 (1997) 934.
- [207] H. Chen, D.T. Shi, B. Granderson, M.A. George, W.E. Collins, A. Burger, R.B. James, J. Vac. Sci. Technol. A 15 (1997) 850.
- [208] H. Chen, K. Chattopadhyay, K.-T. Chen, A. Burger, M.A. George, J.C. Gregory, P.K. Nag, J.J. Weimer, R.B. James, J. Vac. Sci. Technol. B A17 (1999) 97.
- [209] A. Rusin, Y. Nemirovsky, Appl. Phys. Lett. 71 (1997) 2274.
- [210] W. Monch, Semiconductor Surfaces and Interfaces, 2nd Edition, Vol. 347, Springer, Berlin, 1995.
- [211] R. Arlt, V. Ivanov, A. Khusainov, SPIE Proc. 3115 (1997) 76.
- [212] T. Takahashi, K. Hirose, C. Matsumoto, K. Takizawa, R. Ohno, T. Ozaki, K. Mori, Y. Tomita, SPIE Proc. 3446 (1998) 29.
- [213] M. Driver, private communication.
- [214] T. Hazlett, H. Cole, M.R. Squillante, G. Entine, G. Sugars, W. Fecych, O. Tench, IEEE Trans. Nucl. Sci. 33 (1986) 332.
- [215] A. Nimela, H. Sipila, IEEE Trans. Nucl. Sci. 43 (1996) 1476.
- [216] R. Sudharsanan, G.D. Vakerlis, N.H. Karam, J. Electron. Mater. 26 (1997) 745.

- [217] W.J. Hamilton, D.R. Rhiger, S. Sen, M.H. Kalisher, G.R. Chapman, R.E. Millis, J. Electron. Mater. 25 (1996) 1286.
- [218] U. Lachish, Nucl. Instrum. Methods A 403 (1998) 417.
- [219] U. Lachish, in: Proceedings of the Presentation at the 1998 Nuclear Sciences Symposium, Toronto, CA, November 1998, unpublished.
- [220] M. Silver, M.P. Shaw, in: J. Mort, D.M. Pai (Eds.), Photoconductivity and Related Phenomena, Elsevier, Amsterdam, 1976, pp. 1–25.
- [221] E. Belcarz, J. Chwaszczewska, M. Slapa, M. Szymczak, J. Tys, Nucl. Instrum. Methods 77 (1970) 21.
- [222] D.M. Hofmann, W. Stadler, P. Christmann, B.K. Meyer, Nucl. Instrum. Methods A 380 (1996) 117.
- [223] A. Castaldini, A. Cavallini, B. Fraboni, P. Fernandez, J. Piqueras, J. Appl. Phys. 83 (1998) 2121.
- [224] B.A. Brunett, Ph.D. Thesis, Carnegie Mellon University, 2000.
- [225] C. Szeles, M. Driver, SPIE Proc. 3466 (1998) 1.
- [226] F.P. Doty, private communication, 1999.
- [227] B.A. Brunett, T.E. Schlesinger, J.E. Toney, R.B. James, SPIE Proc. 3768 (1999) 348.
- [228] P.N. Luke, E.E. Eissler, IEEE Trans. Nucl. Sci. 43 (1996) 1481.
- [229] Y. Nemirovsky, A. Rusin, G. Asa, J. Gorelik, J. Electron. Mater. 25 (1996) 1221.
- [230] J. Toney, T.E. Schlesinger, R.B. James, IEEE Trans. Nucl. Sci. 45 (1998) 105.
- [231] P. De Antonis, E.J. Morton, F.J.W. Podd, IEEE Trans. Nucl. Sci. 43 (1996) 1487.
- [232] L.S. Varnell, W.A. Mohone, E.L. Hull, J.F. Butler, A.S. Wong, SPIE Proc. 2806 (1996).
- [233] L.M. Bartlett, Goddard Space Flight Center, Greenbelt, MD, private communication, 1997.
- [234] L.M. Bartlett, C.M. Stahle, P. Shu, L.M. Barber, S.D. Barthelmy, N. Gehrels, J.F. Krizmanic, P. Kurczynski, A. Parsons, B.J. Teegarden, T. Tuellere, SPIE Proc. 2859 (1996) 10.
- [235] L.A. Franks, B.A. Brunett, B.L. Doyle, R.W. Olsen, G. Vizkelthy, D.S. Walsh, J.I. Trombka, R.B. James, Nucl. Instrum. Methods A428 (1999) 95.
- [236] E. Molva, K. Saminadayar, J.L. Pautrat, E. Ligeon, Solid State Commun. 48 (1983) 955.
- [237] J.M. Francou, K. Saminadayar, J.L. Pautrat, Phys. Rev. B 41 (1990) 12035.
- [238] W. Jantsch, G. Brunthaler, G. Hendorfer, Mater. Sci. Forum 10–12 (1986) 515.
- [239] Ch. Ye, J.H. Chen, J. Appl. Phys. 67 (1990) 2475.
- [240] P.I. Babii, V.V. Slynko, Yu.P. Gnatenko, P.N. Bukivskii, M.I. Llashchuk, O.A. Parfenyuk, Sov. Phys. Semicond. 24 (1990) 904.
- [241] P. Christman, B.K. Meyer, J. Kreissl, R. Schwarz, K.W. Benz, Appl. Phys. Lett.
- [242] M.J. Caldas, Z. Fazzio, Z. Zunger, Appl. Phys. Lett. 45 (1984) 671.
- [243] M. Godlewski, J.M. Baranowski, Phys. Stat. Sol. (b) 97 (1980) 281.
- [244] V.G. Deybuk, et al., Izv. Vuzov. Fizika 4 (1982) 24.
- [245] K. Lischka, G. Brunthaler, W. Jantsch, J. Cryst. Growth 72 (1985) 355.
- [246] A. Sarem, B.A. Orlowski, S. Kuzminski, Acta Phys. Pol. A 79 (1991) 183.
- [247] G. Hendorfer, G. Brunthaler, W. Jantsch, J. Reisinger, H. Sitter, J. Cryst. Growth 86 (1988) 497.
- [248] E. Molva, J.P. Chamonal, J.L. Pautrat, Phys. Stat. Sol. (b) 109 (1982) 635.
- [249] Y. Eisen, A. Shor, Mater. Res. Soc. Symp. 487 (1998) 129.
- [250] O. Tousignant, L. Hamel, J. Courville, J. Macri, M. Mayer, M. McConnell, J. Ryan, IEEE Trans. Nucl. Sci. 45 (1998) 413.
- [251] Z. He, G. Knoll, D. Wehe, Y. Du, Mater. Res. Soc. 487 (1998) 89.
- [252] H.L. Glass, A.J. Socha, C.L. Parfeniuk, D.W. Bakken, J. Cryst. Growth 184/185 (1998).
- [253] E. Molva, J.P. Chamonal, G. Milchberg, K. Saminadayar, B. Pajot, G. Neu, Solid State Commun. 44 (1982) 351.
- [254] E. Molva, J.M. Francou, J.P. Pautrat, K. Samindayar, L.S. Dang, J. Appl. Phys. (1984).
- [255] C.H. Park, D.J. Chadi, Appl. Phys. Lett. 66 (1995) 3167.
- [256] K. Suzuki, N. Akita, S. Dairaku, S. Seto, T. Sawada, K. Imai, J. Cryst. Growth 159 (1996) 406.
- [257] A. Zerrai, G. Bremond, J. Appl. Phys. 84 (1998) 5554.
- [258] A. Zerrai, G. Marrakchi, G. Bremond, J. Appl. Phys. 87 (2000) 4293.
- [259] M. Yamada, K. Yamamoto, K. Abe, J. Phys. D. 10 (1977) 1309.
- [260] K. Yasuda, K. Kojima, K. Mori, Y. Kubota, T. Nimura, F. Inukai, Y. Asai, J. Electron. Mater. 27 (1998) 527.
- [261] J.S. Goela, R.L. Taylor, Appl. Phys. Lett. 51 (1987) 928.
- [262] E.E. Haller, in: P.Y. Yu, M. Carlona (Eds.), Fundamentals of Semiconductors, Springer Verlag, New York, 1996, pp. 539–541.
- [263] R.J. Zucca, J. Appl. Phys. 48 (1977) 1987.
- [264] J.A. von Windheim, M. Cocivera, J. Phys. Chem. Solids 53 (1992) 31.
- [265] R.E. Kremer, W.B. Leigh, J. Cryst. Growth 86 (1988) 490.
- [266] A. Waag, T. Litz, F. Fischer et al., J. Cryst. Growth. 138 (1994) 437.
- [267] L. Verger, N. Baffert, M. Rosaz, J. Rustique, Nucl. Instrum. Methods. Phys. Res. A 380 (1996) 121.
- [268] J.E. Toney, B.A. Brunett, T.E. Schlesinger, R.B. James, E.E. Eissler, IEEE Trans. Nucl. Sci. 44 (1997) 499.